Simultaneous measurement of the top quark pair production cross-section and R_b in the ATLAS experiment

Jordi Nadal

Institut de Física d'Altes Energies

Universitat Autònoma de Barcelona

supervised by

Dr. Lluïsa-Maria Mir

2012 July

Abstract

This thesis describes the simultaneous measurement of the top pair production cross-section together with the R_b parameter in the lepton plus jets channel with 1 fb^{-1} of the 2011 data at 7 TeV obtained with the ATLAS experiment at the LHC. Events are categorized in 18 orthogonal channels, depending on the lepton flavor (e or μ), the jet multiplicity (3, 4, or 5 jets) and the b-tagging multiplicity (0, 1, or 2 tags).

With 1 fb^{-1} of luminosity, the $t\bar{t}$ cross-section measurement is limited by systematic uncertainties and much effort has been put into trying to quantify and, when possible, limit their impact on the overall measurement precision. The analysis also includes a measurement of R_b , which has not been performed in ATLAS yet. The R_b parameter is related to the $|V_{tX}|$ mixing matrix elements and, in combination with the single top cross section measurement, can be used to set quasi model independent constraints on their magnitudes. In addition, it is sensitive to new physics with heavy-flavour content larger than the one predicted by the SM processes.

Als meus pares

Contents

List of Figures

LIST OF FIGURES

List of Tables

1

Introduction

Ancient Greeks already postulated that matter is made out of small building blocks or atoms, as Democritus called them. Major updates on particle physics came from J. J. Thomson and the electron discovery in 1897 [2]. In the next decades more and more understanding of the atomic structure and discoveries came along. Nuclei lost their elementary character revealing the existence of protons and neutrons in Rutherford's experiment in 1911. In 1968 at SLAC, protons and neutrons were shown to contain much smaller, point-like, particles named quarks [3] [4]. A particle "zoo" started to emerge from colliders around the world and a theory was developed to give them a common framework: the Standard Model (SM) [5] [6]. The SM as we know it nowadays includes twelve elementary constituent particles: three charged leptons, three neutrinos and six quarks. All of them have been discovered, the tau neutrino being the latest one in 2000.

The SM explains three out of the four known fundamental forces: the electromagnetic, the weak and the strong forces. These forces are mediated via interaction bosons [7]. They are the photon, the $W^{\pm}$ and Z and eight gluons. Finally, the Higgs boson is responsible to give mass to all particles. All of them, except the Higgs boson, have been discovered and their properties measured precisely. However, on July, 4^{th} 2012 CERN announced the discovery of a new particle with properties similar to those of the Higgs boson [8].

According to the SM, the top quark decays almost 100% of the times into a W boson and a b-quark, and the probability of this to occur is proportional to $|V_{tb}|^2$ [9]. In this thesis we measure the fraction of tops decaying into a W boson and a b-

quark. This quantity is known as the R_b parameter and is defined as $R_b = \frac{B(t\to Wb)}{B(t\to Wq)} = \frac{|V_{tb}|^2}{|V_{tb}|^2+|V_{ts}|^2+|V_{td}|^2}$, where V_{tb}, V_{ts} and V_{td} are the Cabibbo-Kobayashi-Maskawa (CKM) matrix elements. Any deviation of R_b from the SM value can be used in combination with the single top cross section measurements to set quasi model independent constraints on the magnitudes of the CKM matrix elements. In addition, it is sensitive to new physics with heavy-flavor content larger than the one predicted by the SM processes.

In this thesis we focus on the lepton plus jets top quark pair decay channel to measure simultaneously the $t\bar{t}$ production cross-section and R_b. The reconstruction of decay final states is extremely complicated since all detector elements are required to detect them. They involve leptons (electrons or muons), light jets, b-jets and missing transverse energy. There are other physics processes that have identical or similar final state, mainly vector boson decays, but also single top and multi-jet processes, which can, therefore, fake the top quark pair decay.

With 1 fb^{-1} of 2011 data the measurement is dominated by systematic uncertainties, which have been studied carefully. $\sigma_{t\bar{t}}$ and R_b are obtained from a likelihood fit to the reconstructed mass of the hadronic top. Using the profiling technique, the systematic uncertainties are treated as free parameters, and therefore, with large enough samples, can eventually be constrained by the data themselves.

This document is organized as follows. The SM is introduced in Chapter 2. Chapter 3 is devoted entirely to top physics including the top observation, mass measurements and production rates, among other topics. Chapter 4 contains basic information about Monte Carlo techniques, and concepts like parton shower, hadronization, and underlying event are introduced. In Chapter 5, the LHC accelerator and ATLAS detector are described. Chapter 6 deals with object reconstruction, and includes the description of how particles are detected and reconstructed inside the ATLAS detector. The main analysis and measurements are presented in Chapter 7. Conclusions are drawn in Chapter 8.

2

Theory

2.1 The Standard Model of Particle Physics

The entire universe is built from a plethora of particles. Matter seems to be made of twelve building blocks or elementary particles, named leptons and quarks, and interacts through four fundamental forces. The force carriers are also particles, called bosons. These particles are governed by the rules of the Standard Model (SM). The SM aims to describe the fundamental forces of our universe. These are the electromagnetic force, which provides the attraction between electrons and nuclei to form atoms and molecules; the weak interaction, which is behind the nuclear beta decays [10]; and the strong force, which holds quarks together to form mesons and baryons, and also binds nucleons together to form nuclei. Gravity, the weakest force in nature and negligible at nuclear regimes, is not described in the SM.

2.1.1 Gauge Theories

Due to the phase (or gauge) invariance in quantum mechanics, quantum-mechanical observables are unchanged under phase rotations of the wave functions. Since quantum-mechanical equations of motion always involve derivatives of the wave functions, in order to achieve local phase invariance one has to modify the equations of motion (and the observables involving derivatives) by the introduction of additional fields.

Let us consider the Schrödinger equation as example. The quantum mechanical state described by the complex wave function $\psi(x)$ is invariant under a global phase rotation $\psi(x) \rightarrow e^{i\theta}\psi(x)$. To have $\psi(x)$ also invariant under a local phase rotation

$\psi(x) \rightarrow e^{i\theta(x)}\psi(x)$, it is necessary to introduce the electromagnetic field $A_\mu(x)$ and to replace the gradient ∂_μ by the gauge-covariant derivative $\mathcal{D}_\mu \equiv \partial_\mu + ieA_\mu$, where e is the charge of the particle described by $\psi(x)$, and the field A_μ transforms under phase rotations as $A_\mu(x) \rightarrow A_\mu(x) - \frac{1}{e}\partial_\mu\theta(x)$. The required transformation of the field has the form of a gauge transformation in electrodynamics, and the covariant derivative corresponds to the canonical replacement $(p^\mu - eA^\mu) \rightarrow i(\partial^\mu + ieA^\mu)$, which leads to the covariant form of Maxwell's equations. Furthermore, the gauge invariance of electromagnetism leads, via Noether's theorem, to the conservation of the electric charge.

Thus, the imposition of local symmetry requires the existence of interactions, and can serve as a dynamical principle to the construction of interacting field theories.

2.1.2 The Standard Electroweak Gauge Theory

The electroweak gauge theory (EW) unified two of the four fundamental forces: the electromagnetic and weak interactions. The relativistic quantum theory for the electromagnetic force (QED) was first written by Paul Dirac who, with many others, described the quantization of the electromagnetic field and made possible, in principle, the computation of any electromagnetic process [11]. QED is based on the $U(1)$ gauge group. By imposing gauge invariance, the existence of a gauge boson, the photon, is required and the interaction with fermions is specified. However, computations are reliable only at first order of perturbation theory making the theory unpredictable at higher orders. Such pathologies are dealt with by means of the *renormalization* [12]. Renormalization is the process where the divergencies found at high orders of perturbative calculation are included into the theoretical constants at tree level. Once renormalized, QED is a predictable theory for any fermion and its interaction with photons.

Electroweak interactions are the responsible for both nuclear β decays $n \rightarrow p + e^- + \bar{\nu_e}$ and muon decays $\mu^- \rightarrow e^- + \bar{\nu_e} + \nu_\mu$. Becquerel (1896) studied the decay ${}^A Z \rightarrow {}^A (Z+1) + \beta^-$. The apparent no conservation of energy in the interaction led Pauli (1930) [13] to postulate the existence of a new (undetected at that time) particle, the neutrino [14]. The muon decay can be explained from a quantum field theory similar to QED, but in the muon decay the gauge field can not be a neutral boson, like the QED photon, it has to be electrically charged. So there must be at least two more

gauge bosons responsible for the weak interaction, and actually we will see that there are three new bosons.

Given the fact that QED and the weak interaction have some similarities, it is reasonable to think that the two interactions can be combined in the same framework. Abdus Salam, Sheldon Glashow and Steven Weinberg worked on the unification in 1967 [5] [6].

Experiments with neutrinos in 1962 showed that the electronic neutrino and the muon neutrino are different particles. The tau and tau neutrino were not discovered until 1977 (Mark I Experiment, SLAC) [15] and 2000 (DONuT, Fermilab) [16], respectively. In the SM, leptons are arranged in families:

$$\begin{pmatrix}\nu_e\\ e^-\end{pmatrix}, \qquad \begin{pmatrix}\nu_\mu\\ \mu^-\end{pmatrix}, \qquad \begin{pmatrix}\nu_\tau\\ \tau^-\end{pmatrix}.$$

Tab. 2.1 shows the mass and lifetimes of the leptons. All leptons have spin 1/2.

Table 2.1: Lepton masses and lifetimes [1].

Lepton	Mass (c=1)	Lifetime
e^-	0.510998902(21) MeV	$> 4.6 \times 10^{26}$ y (90% C.L.)
ν_e	< 3 eV	
μ^-	105.658357(5)MeV	$2.19703(4) \times 10^{-6}$ s
ν_μ	< 0.19 MeV	
τ^-	$1776.99^{+0.29}_{-0.26}$ MeV	$290.6 \pm 1.1 \times 10^{-15}$ s
ν_τ	< 18.2 MeV	

The EW interaction is based on the $SU(2)_L \times U(1)_Y$ symmetry group. Local invariance in the $SU(2)_L$ group introduces * three new gauge bosons for the weak interaction ($W^\pm$ and Z) and one for $U(1)_Y$ (photon). The Lagrangian for the electroweak interaction is

$$\mathcal{L}_{EW} = -\frac{1}{4}W_{\mu\nu}W^{\mu\nu} - \frac{1}{4}B_{\mu\nu}B^{\mu\nu} + \bar{\psi}i\gamma^\mu D_\mu\psi \tag{2.1}$$

*A Lie group SU(n) has (n^2-1) generators.

the covariant derivative being

$$D_\mu = \partial_\mu + igW_\mu T + ig'(1/2)B_\mu Y \tag{2.2}$$

where T and Y are the isospin and hypercharge operators, which can be represented by Pauli matrices. $W_\mu^\pm$ and B_μ can be expressed as

$$W_\mu^\pm = \frac{1}{\sqrt{2}}(W_{1\mu} \pm iW_{2\mu}) \tag{2.3}$$

and

$$igW_3T_3 + ig'\frac{1}{2}BY = iA[g\sin\theta_W T_3 + g'\cos\theta_W \frac{1}{2}Y] + iZ[g\cos\theta_W T_3 - g'\sin\theta_W \frac{1}{2}Y] \tag{2.4}$$

The subindex L in $SU(2)_L$ means that only left-handed particles interact weakly. Processes like beta decays only affect fermions with the spin in the opposite direction of their motion. Right-handed particles can be seen as singlets in this group, and therefore do not interact with the weak bosons.

At this stage, the main deficiency of the SM is the prediction of massless particles, in contrast with the experimental measurements [17]. The solution to this problem will be discussed in the next section.

2.1.3 Spontaneous Symmetry Breaking

Only massless vector fields are gauge invariant under local transformations of the EW Lagrangian. Additional mass terms like $m^2W^\mu W_\mu$ are not gauge invariant, and therefore can not be included directly in the Lagrangian to get masses for the (experimentally measured to be massive) $W^\pm$ and Z bosons. The concept of spontaneous symmetry breaking (SSB) [18] [19] was introduced in the EW theory to allow particles to acquire mass while keeping the theory still renormalizable.

Let's consider the Higgs potential for scalar particles $V = \mu^2\phi^2 + \frac{1}{2}\lambda\phi^4$ with $\lambda > 0$. If $\mu^2 > 0$ the above potential simply describes a scalar field with mass μ. The interesting case occurs when $\mu^2 < 0$, because the minimum of the potential is not at $\phi = 0$ but at $\phi = \sqrt{-\mu^2/\lambda}$, which is referred to as the vacuum expectation state of ϕ. Choosing the correct expansion for the perturbative calculation around the minima of the Higgs potential breaks the symmetry of the Lagrangian. Furthermore, some terms that give

masses to the $W^{\pm}$ and Z boson while ensuring that the photon remains massless appear in the Lagrangian. This is what is called the Higgs mechanism.

2.1.4 Quantum Chromodynamics

In 1960's a large amount of different hadrons were emerging from colliders. M. Gell-Mann and Y. Ne'eman, independently, developed the *Eightfold Way* classification [20]. This conducted M. Gell-Mann and G. Zweig [21] [22] to the idea of quarks, elementary particles "living" and interacting inside hadrons. Their theory only included three quarks, the up, the down and the strange. Electron-proton collisions at the SLAC-MIT experiment in 1968, showed that the proton contained much smaller particles and was therefore not an elementary particle [23] [24]. These smaller particles were later identified as quarks. An extension of the model (by Glashow and Bjorken) predicted the existence of a new quark, the charm quark. In 1970, S. Glashow, J. Iliopoulos and L. Maiani presented further motivations for the existence of the yet undiscovered charm quark. Finally, in 1974, charm quarks were produced simultaneously by two teams, one at SLAC, led by B. Richter, and the other at Brookhaven, under S. Ting. The charm quarks were observed as bound charm-anticharm states. In summer of 1977, a team of physicists led by Leon M. Lederman working on an experiment at Fermilab discovered the upsilon particle, which is composed of a bottom-antibottom quark pair [25]. The top quark was the latest to be discovered (1995) at the Tevatron, Fermilab [26] [27]. Thus, three families of quarks similarly to those of leptons can be structured as:

$$\begin{pmatrix} u \\ d \end{pmatrix}, \qquad \begin{pmatrix} c \\ s \end{pmatrix}, \qquad \begin{pmatrix} t \\ b \end{pmatrix}.$$

Table 2.2 shows the masses and charges of the quarks. All quarks have spin 1/2.

Quantum Chromodynamics (QCD) is the theory which describes the strong interactions, built to explain the interactions among quarks to form mesons (combinations quark-antiquark) and baryons (combinations of three quarks). Quarks and gluons carry "color charge", analogous to the electric charge in QED. The color charge was introduced to explain how identical quarks could coexist inside hadrons without violating the principle of exclusion of Pauli. QCD is a non-Abelian theory based in the $SU(3)$ Lie group, and predicts the existence of eight massless gauge bosons, named gluons. Each quark has a color either red, blue or green (anti-quarks have anti-red, anti-blue

Table 2.2: Quarks masses and charges [1].

Lepton	Mass (c=1)	Charge
u	$2.3^{+0.7}_{-0.5}$ MeV	2/3
d	$4.8^{+0.7}_{-0.3}$ MeV	-1/3
c	1.275 ± 0.025 GeV	2/3
s	95 ± 5 MeV	-1/3
t	173.5 ± 1.0 GeV	2/3
b	4.18 ± 0.03 GeV	-1/3

or anti-green colors) and gluons are color-anticolor combinations. Thus, baryons are built with three quarks of three different colors and mesons are color-anticolor combinations. Quarks can not be observed isolated (they are not color-eigenstates) so from the experimental point of view only hadrons can be studied.

The Lagrangian for QCD is

$$\mathcal{L}_{QCD} = \sum_{flavour} \bar{q}_a (i\gamma^\mu (D_\mu)_{ab} - m_q \delta_{ab}) q_b - \frac{1}{4} F^A_{\mu\nu} F^{\mu\nu}_A \tag{2.5}$$

where $D_\mu = \partial_\mu + i g_s A^\alpha_\mu T^\alpha$ is the covariant derivative, T^α are the Gell-Mann matrices, γ^μ are the Dirac matrices, q_a is the quark field of flavour a and mass m_{q_a}, and a and b run over the six quark flavours. The coupling constant $g_s = \sqrt{4\pi\alpha_S}$ is the parameter of the theory giving the strength of the interaction. The field tensor $F^A_{\mu\nu}$ is given by $F^A_{\mu\nu} = \partial^A_\mu G^A_\nu - \partial^A_\nu G^A_\mu - g_s f_{ABC} G^B_\mu G^C_\nu$, where f_{ABC} are the structure constants of the $SU(3)$ group, and A, B and C indices run over the eight degrees of freedom of the gluon field. The third term of the field tensor is responsible for the non-Abelian nature of QCD and describes the gluon self-interactions. The gluons self-coupling determines the variation of the strong interaction strength with energy, and leads to the two main characteristics of QCD: asymptotic freedom and confinement [28] [29]. At very high momentum transfers, or equivalently at very short distances, the strong coupling is weak. Inside the hadrons, quarks and gluons behave as nearly-free particles (asymptotic freedom). On the other hand, and large distances or small momentum transfers, the strong coupling grows, leading to the confinenement of quarks and gluons, which cannot be observed as free particles: When two quarks become separated it is energetically

more efficient to create a new pair quark-antiquark. The newly created quarks and antiquarks combine to form hadrons.

2.1.5 Quark Mixing and Cabibbo-Kobayashi-Maskawa Matrix

The fact that the number of families is bigger than one allows quark mixing. The theoretical motivation for quark mixing is that gauge invariance allows non-diagonal mass matrices, such that mass eigenstates of down-type quarks can be expressed as rotations of weak eigenstates (weak eigenstates are the ones defined previously by the gauge transformations [30]) *

$$d' = d\cos\theta_c + s\sin\theta_c \tag{2.6}$$

$$s' = -d\sin\theta_c + s\cos\theta_c \tag{2.7}$$

which means that the neutral-current for the up quark is

$$J_\mu = \bar{u}\gamma_\mu(1+\gamma_5)[d\cos\theta_c + s\sin\theta_c] \tag{2.8}$$

With the existence of only the up, down and strange quarks, the weak eigenstate $s' = -d\sin\theta_c + s\cos\theta_c$ would be uncoupled to the up quark, and the theory could not account for strangeness-changing weak interactions such as the decay $\Lambda \to p^+\pi^-$. This motivated Glashow, Iliopoulos and Maiani (1970) to introduce the charm quark [32], experimentally discovered in 1974 [33] [34].

In the three-family six-quark case, we have the Cabibbo-Kobayashi-Maskawa (CKM) unitary matrix

$$\begin{bmatrix} |d'\rangle \\ |s'\rangle \\ |b'\rangle \end{bmatrix} = \begin{bmatrix} V_{ud} & V_{us} & V_{ub} \\ V_{cd} & V_{cs} & V_{cb} \\ V_{td} & V_{ts} & V_{tb} \end{bmatrix} \begin{bmatrix} |d\rangle \\ |s\rangle \\ |b\rangle \end{bmatrix}. \tag{2.9}$$

After unitarity constraints, the CKM matrix can be described by four physical independent parameters: three angles and one phase. The present knowledge of the CKM matrix elements is [1]:

*Note: if neutrinos are massless, the lepton mixing is unobservable [31].

- $|V_{ud}|$= 0.97425 ± 0.00022.
- $|V_{us}|$= 0.2252 ± 0.0009.
- $|V_{cd}|$= 0.230 ± 0.011.
- $|V_{cs}|$= 1.006 ± 0.023.
- $|V_{cb}|$= (40.9 ± 1.1) x 10^{-3}.
- $|V_{ub}|$= (4.15 ± 0.49) x 10^{-3}.
- $|V_{td}|/|V_{ts}|$= 0.211 ± 0.006.
- $|V_{tb}|$= 0.89 ± 0.07.

Figure 2.1 sketches several processes that can be used to determine the values of the different CKM matrix elements. We will discuss further $|V_{tb}|$, $|V_{ts}|$ and $|V_{td}|$ in the following chapter.

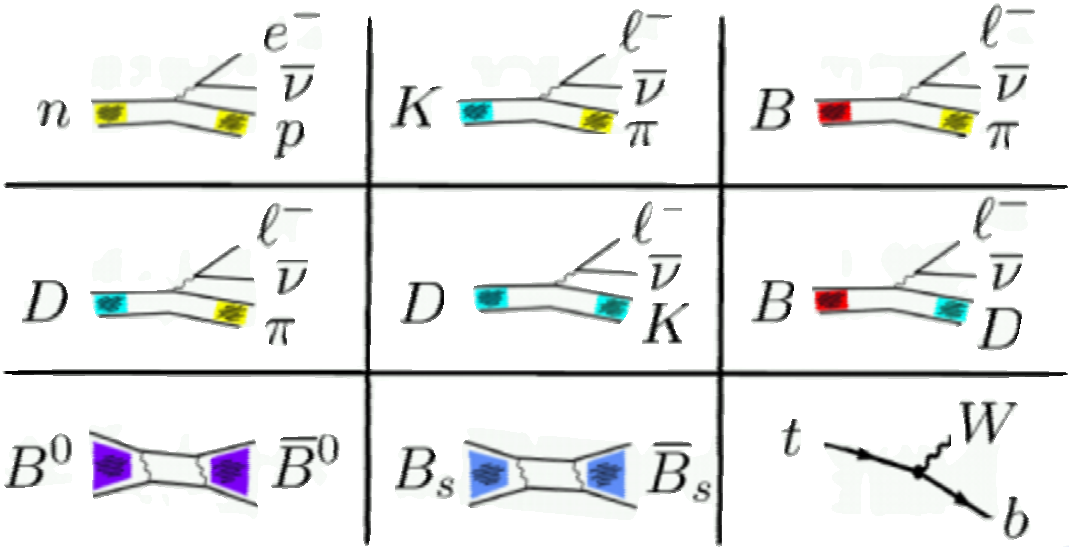

Figure 2.1: Experimental determination of each of the CKM matrix elements.

2.1.6 Incompleteness of the Standard Model

Even though the SM has been tested to a very high degree of accuracy (see Fig. 2.2) it is not a complete theory because it leaves many questions unanswered. Why do we have three families and why do their mass scales differ so much? Which is the origin of the matter/antimmater asymmetry in the universe? Why are the electroweak and Plank scales so different? What are dark matter and dark energy composed of?

One can hope that detailed studies of the top quark, the most massive elementary particle discovered so far, will eventually help to solve some of the open questions of the SM.

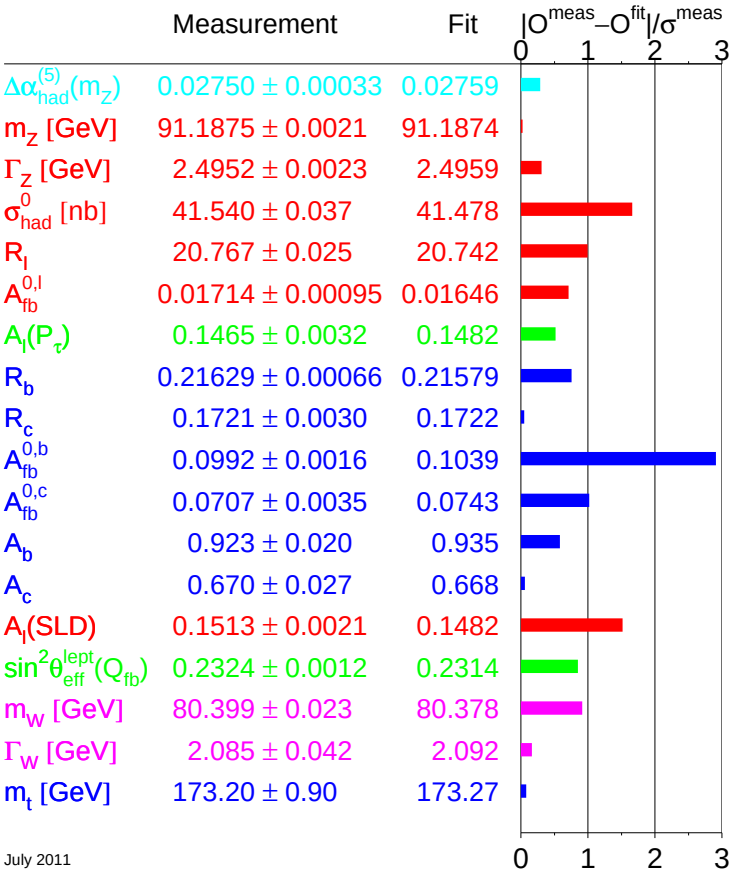

Figure 2.2: Comparison of the global fit of the electroweak SM results with direct measurements. The rightmost graph shows the pulls or differences between the measurements and the fit predictions divided by the measurements uncertainties. For almost all parameters, the deviation of the measurements from the predictions is within the uncertainties, showing the good predictive power of the SM.

3

Top Quark Physics

The D0 collaboration reports on a search for the Standard Model top quark in $p\bar{p}$ collisions at $\sqrt{s} = 1.8$ TeV at the Fermilab Tevatron. [...] The kinematic properties of the excess events are consistent with top quark decay. We conclude that we have observed the top quark and measure its mass to be $199^{+19}_{-21}(stat.) \pm 22(syst.)$ GeV/c^2 and its production cross-section to be 6.4 ± 2.2 pb.

3.1 Top Quark

The above quotation shows a fragment of one of the articles that D0 and CDF [26] [27] released on March 1995 on the observation of the top quark. This was another great success of the SM predictions and also the completion of the third quark generation family together with the bottom quark. The top quark is the heaviest particle discovered so far, with basic properties of electric charge $Q = +2/3$ and isospin $T_3 = +1/2$. This chapter will review the most important characteristics of the top quark, from its production in hadron colliders to its decays and various properties. The main backgrounds to $t\bar{t}$ signal are described at the end of the chapter.

3.1.1 Top Production and Decays

The top quark pair production cross section in pp colliders (see Sec. 4.1) depends on the parton density function (PDF), which describes the probability to find a parton i inside the proton carrying a momentum fraction x_i. To produce a top pair, x_i should

be of order $\frac{2m_t}{\sqrt{s}}$, which amounts to approximately 0.05 at the LHC and 0.18 at the Tevatron.

Figure 3.1 [35] shows the PDF of a proton measured at different Q^2. Valence quarks (u, d) dominate at large x and gluons (g) at low x. Sea quarks ($\bar{u}$, $\bar{d}$, s, c, b) contribute mostly at low x. At higher Q^2, the gluon and sea quarks density increases with respect to the valence quarks.

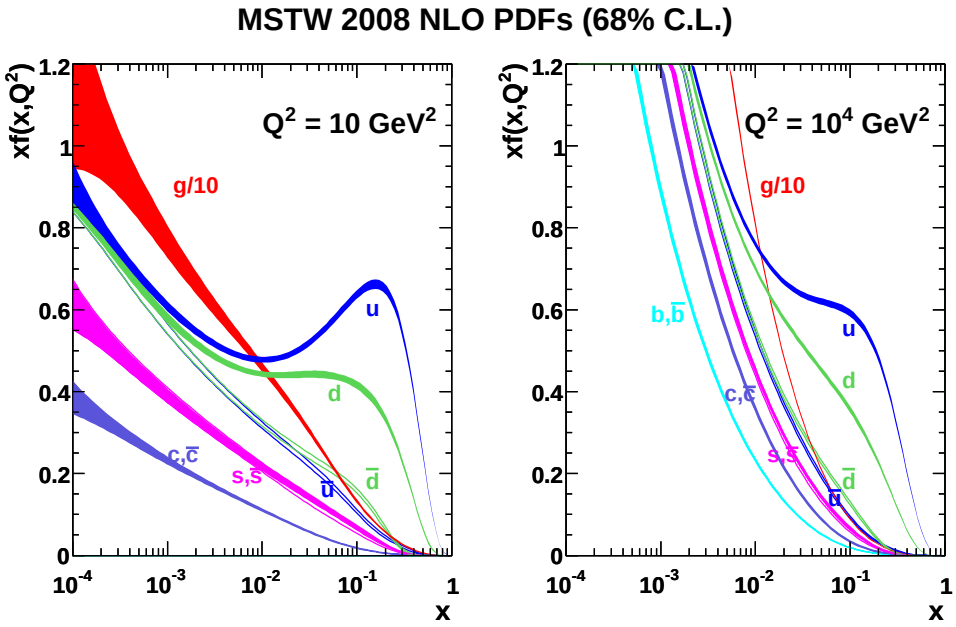

Figure 3.1: Distributions of x times the PDF $f(x)$ and their associated errors at two differerent values of Q^2 as a function of x.

At LHC the top pair production is dominated by gluon fusion processes (shown in Fig. 3.2) which account for $\sim 85\%$ of the total. The rest proceeds via quark-antiquark annihilation (see Fig. 3.3). The total cross-section of top quark pair production in pp colliders has been computed theoretically in perturbation theory to next to next to leading order (NNLO) accuracy with a precision better than 10 % [36]:

$$\sigma_{t\bar{t}} = 165^{+11}_{-16} \text{ pb at } \sqrt{s} = 7 \text{ TeV}.$$

Due to the generation mixing, the top quark can decay to Wd and Ws states, but in the SM these final states are expected to be suppressed relative to Wb by the ratio

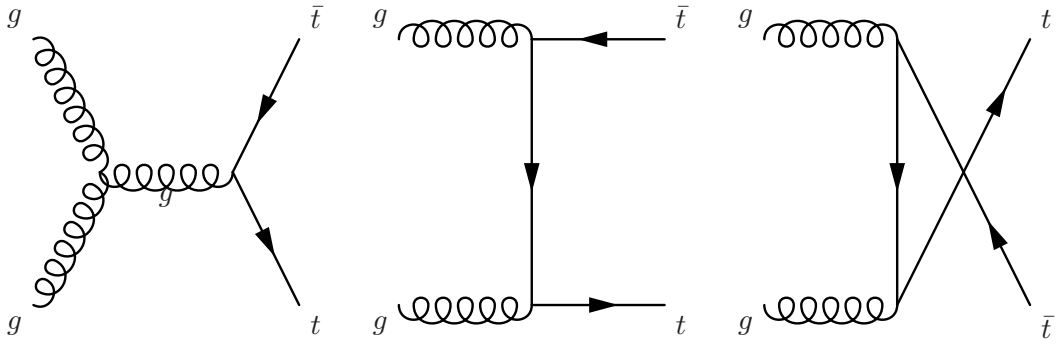

Figure 3.2: Born level Feynman diagrams contributing to top quark pair production. The gluon annihilation is the dominating top pair production at the LHC, accounting for 85% of the total.

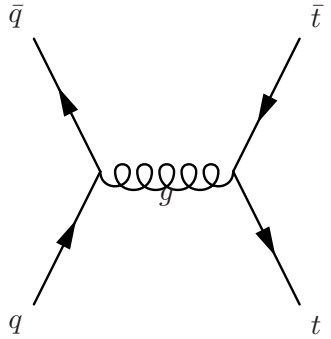

Figure 3.3: Born level Feynman diagrams contributing to top quark pair production. The quark annihilation is the dominating top pair production at the Tevatron. At LHC it contributes only about 15%.

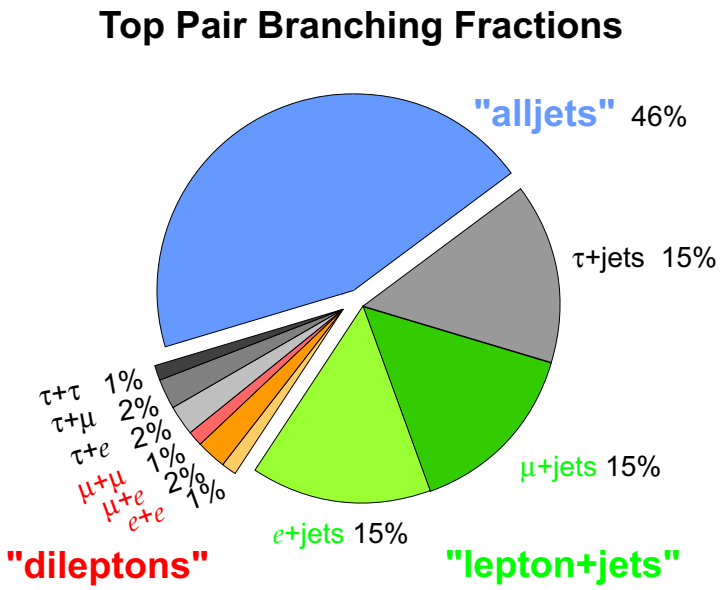

Figure 3.4: Top pair branching fractions, dominated by the "alljets" signature, where the two Ws decay to light jets.

of the square of the CKM matrix elements $|V_{ts}|$ and $|V_{td}|$ with respect to $|V_{tb}|^2$ (see Sec. 3.1.2.2).

Once the top pair has been produced, a classification of the final state can be made depending on how the W decays (see Fig. 3.4):

- The *fully hadronic final state*, where the two Ws decay hadronically, has almost half of the phase space. This final state suffers from a large multi-jet background. In addition it is difficult to trigger on it since there is no lepton nor missing transverse energy present in the event. The signature for the "all jets" final state are two high-p_{T} jets corresponding to the b-jets since they are coming directly from the top decays and are expected to have the highest p_{T}, and four more light-jets from the W decays.

- The *lepton plus jets final state* is the one we will use in this analysis. This decay accounts practically for the remaining part of the phase space, as "e + jets" accounts for $\sim$ 15 %, "μ + jets" for $\sim$ 15 % and "τ + jets" for $\sim$ 15 %. In the electron and muon cases, it is characterized by the presence of two b-jets, one high-p_{T} lepton, missing transverse energy from the leptonic W decay, and two

light jets from the hadronic W decay products. It is the best channel in terms of signal over background ratio and statistics.

- The *dilepton* channel is the channel with the smallest branching ratio, ~ 9 %. It suffers from little background contamination when only electrons and/or muons are present in the final state.

3.1.2 Top Properties

The SM fixes almost all the top quark properties. Therefore any experimental measurement of those properties can be used to gain accuracy in our knowledge of the SM, to set limits on new physics or to discover possible deviations from the theory yielding to a new model. This section attempts to briefly discuss some theoretical implications of different top quark properties that can be measured at the LHC detectors. For a review on top quark see [37] [38].

3.1.2.1 Top Mass and Top Width

The top quark is the heaviest fundamental particle discovered so far. Before its observation at Tevatron its mass was already predicted via a fit to electroweak measurements with an uncertainty of $\Delta m_t/m_t \sim 6$ %. On its discovery, CDF reported a top mass of 174 ± 10 (stat.)$\pm$ 13 (syst.) GeV and D0 199 ± 20 (stat.) $\pm$ 22 (syst.) GeV. Since then, the precision has improved: The top mass has been measured in September 2011 to be $m_t = 172.9 \pm 0.6$ (stat.)$\pm$ 0.8 (syst.) GeV [39].

A precise measurement of the top mass is important. For example, the knowledge of the top quark mass can help constrain the Higgs Boson mass * via the processes shown in Fig. 3.5.

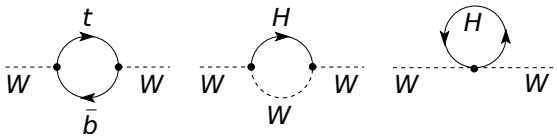

Figure 3.5: Lowest order diagrams that correlate M_W, M_t and M_H

*All masses are free parameters in the SM.

The Yukawa coupling of the top quark, $\lambda_t = 2^{2/3} G_F^{1/2} m_t$ is of order one. This raises the question of why is the top quark mass so different from the other quarks and suggests that it may play a special role in the electroweak symmetry breaking.

The total width, or the corresponding lifetime, is a fundamental property of the top quark that has not yet been measured very precisely. Among other parameters, the top quark width depends on m_t, m_W and the strength of the left handed Wtb coupling, $|V_{tb}|$. The total width predicted by the SM is $\Gamma_t = 1.99^{+0.69}_{-0.55}$ GeV, and increases with the top mass. This corresponds to a lifetime $\tau = 3.3^{+1.3}_{-0.9} \times 10^{-25}$ s [40]. A precise measurement of the top lifetime is also interesting because it can be used to constrain couplings with a 4^{th} generation b' quark [41].

Unlike the b or c hadrons, that can be observed since they have long lifetimes, the top quark is the only quark that decays before hadronization, so there is no phenomenology of top hadrons. On the other hand, since it decays before it can hadronize, its spin is propagated to its decay products.

3.1.2.2 The CKM Matrix Element V_{tb}

As it has been already mentioned, the dominant decay for the top quark is $t \to Wb$, which depends on $|V_{tb}|$. Other SM decays $t \to Ws$ and $t \to Wd$ suffer from small branching ratios, proportional to $|V_{ts}|$ and $|V_{td}|$, respectively. Using the unitary conditions of the CKM matrix, one can obtain $|V_{tb}|$ in an indirect way to be [$0.9990 < |V_{tb}| < 0.9992$] at 90% C.L. The unitary assumption is mainly supported by three experimental facts [42]:

- Measurements of $|V_{ub}|$ and $|V_{cb}|$ in B mesons are in excellent agreement with predictions obtained using lattice QCD calculations.
- The ratio $\frac{\Delta M_{B_d}}{\Delta M_{B_s}}$ (since $\Delta M_{B_q} \propto |V_{tb}^* V_{tq}|^2$) is in good agreement with the unitary hypothesis allowing the ratio $[0.20 < \frac{|V_{td}|}{|V_{ts}|} < 0.22]$ to be accommodated within the unitary condition. It is worth mentioning that these decays come from loop diagrams and can be modified by new physics contributions.
- Latest measurements from CDF and D0 collaborations give $|V_{tb}| > 0.78$ at 95 % C.L., but this value is obtained from the square root of $R_b = \frac{|V_{tb}|^2}{|V_{td}|^2+|V_{ts}|^2+|V_{tb}|^2}$ assuming the unitarity of the CKM matrix.

The possibility that $|V_{tb}| \neq 1$ still exists. One example is the existence of new heavy quarks, since the SM does not fix the number of quark families. Diverse extensions of the SM predict the existence of such quarks, providing a new mixing matrix of dimensions 3×4, 4×4 or even larger.

Any deviation from unity on the direct $|V_{tb}|$ measurement would open a window to new physics processes [43]. For example, the strongest constraint on new models that include a fourth generation quark comes from R_b, which restricts the allowed amount of t - t' mixing.

Latest $|V_{tb}|$ measurements at Tevatron can be seen at [44] [45]. CDF measure R_b alone, using lepton plus jets and dilepton data sets, whereas D0 perform a simultaneous measurement of R_b and $\sigma_{t\bar{t}}$ in a lepton plus jets sample. Both measurements are derived from the relative number of $t\bar{t}$ events with different multiplicity of identified b-jets. CMS also reports an R_b measurement with a result not yet published [46].

3.1.2.3 Top Rare Decays

Flavour changing neutral currents (FCNC) are interactions that change the flavor of the leptons without changing its electrical charge. They are present in the EW Lagrangian only beyond tree level, and therefore suppressed by the GIM mechanism [32]. FCNC involve decays like $t \to \gamma + u/c$, $t \to Z + u/c$ or $t \to$ gluon $+ u/c$. These decays are good candidates for searches beyond the SM physics as several extensions of the SM predict higher branching fractions for the top quark FCNC decays (see Tab. 3.1 [47]). A summary of the LHC latest results can be found in [48] and [49].

3.1.2.4 Charge Asymmetry

As we have seen, in pp collisions at the LHC, the dominant mechanism for $t\bar{t}$ production is gluon-gluon fusion, while the production via quark-antiquark annihilation is small. Since the initial state is symmetric, the forward backward asymmetry is not a useful observable. However, due to the $q\bar{q} \to t\bar{t}(g)$ and $qg \to t\bar{t}q$ processes, there is an asymmetry in the differential distributions of the top and the antitop. QCD predicts at LHC a small excess of centrally produced antitop quarks while top quarks are produced, on average, at larger absolute rapidities. Fig. 3.6 shows the charge asymmetry, defined as $A_c = \frac{N(\Delta|y|>0) - N(\Delta|y|<0)}{N(\Delta|y|>0) + N(\Delta|y|<0)}$, where $\Delta|y|$ is the difference between the absolute values

Process	SM	QS	2HDM	FC 2HDM	MSSM	$\not{R}$ SUSY	TC2
$t \to u\gamma$	3.7×10^{-16}	7.5×10^{-9}	—	—	2×10^{-6}	1×10^{-6}	
$t \to uZ$	8×10^{-17}	1.1×10^{-4}	—	—	2×10^{-6}	3×10^{-5}	—
$t \to ug$	3.7×10^{-14}	1.5×10^{-7}	—	—	8×10^{-5}	2×10^{-4}	—
$t \to c\gamma$	4.6×10^{-14}	7.5×10^{-9}	$\sim 10^{-6}$	$\sim 10^{-9}$	2×10^{-6}	1×10^{-6}	$\sim 10^{-6}$
$t \to cZ$	1×10^{-14}	1.1×10^{-4}	$\sim 10^{-7}$	$\sim 10^{-10}$	2×10^{-6}	3×10^{-5}	$\sim 10^{-4}$
$t \to cg$	4.6×10^{-12}	1.5×10^{-7}	$\sim 10^{-4}$	$\sim 10^{-8}$	8×10^{-5}	2×10^{-4}	$\sim 10^{-4}$

Table 3.1: Theoretical values for the branching fractions of FCNC top quark decays predicted by the SM, the quark-singlet model (QS), the two-Higgs doublet model (2HDM), the flavour-conserving two-Higgs doublet model (FC 2HDM), the minimal supersymmetric model (MSSM), SUSY with R-parity violation and the Topcolour-assisted Technicolour model (TC2).

of the top and antitop rapidities and N is the number of events with $\Delta|y|$ positive or negative, as measured by ATLAS using 1 fb^{-1} of data [50][51].

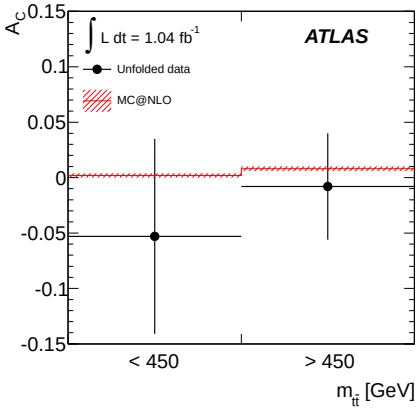

Figure 3.6: Unfolded asymmetries in two regions of m($t\bar{t}$) compared to the prediction from MC@NLO simulation. The error bands on the prediction include uncertainties from parton distribution functions and renormalisation and factorisation scales.

This measurement disfavours models with a new flavour-changing Z' or W' vector bosons that have been proposed to explain the measured Tevatron asymmetry.

3.2 Backgrounds

Due to the fact that only final state products such as leptons and jets are detected, any process whose final state is similar or equal to that of $t\bar{t}$ can mimic a signal event. These processes constitute the physics background. In addition, due to misidentification of physical objects or due to the incomplete coverage of the detector around the beam line such that particles of the final state escape without being detected, processes with different final states can also mimic $t\bar{t}$ decays. They are known as instrumental background.

3.2.1 Vector Boson Production Plus Jets

The main background process is W + jets production (Fig. 3.7). The inclusive cross-sections for W and $t\bar{t}$ production differ by three orders of magnitude, but the requirement of additional jets will decrease the W cross-section. It becomes comparable to the top pair cross-section when three jets are produced together with the W.

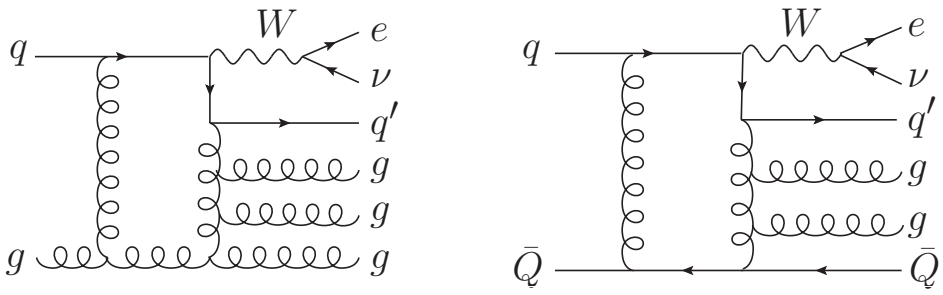

Figure 3.7: Sample diagrams for the seven-point loop amplitudes for $qg \to W\,q'ggg$ and $q\bar{Q} \to W\,q'gg\bar{Q}$, followed by $W \to e\nu$.

The total rate for W + 4 jets is poorly predicted by LO event generators. To reduce the uncertainties at high jet multiplicities, one can use the relation of the cross-sections for W+ n jets and W + (n+1) jets, known as Berends scaling [52]:

$$\alpha = \frac{\sigma_{(W+(n+1)-jets)}}{\sigma_{(W+(n)-jets)}} \tag{3.1}$$

where α is α_s at LO prediction.

NLO computations provide better absolute normalization and shape estimations of differential observables. Therefore they give more confidence in the background

estimations in the signal region. Although NLO processes are not straightforward to compute, a huge improvement has been made in event generation, actually the first hadron collider process with five final-state objects to be computed at NLO was $W + 4$ jets.

Several generators of multiparton hard processes in hadron collisions supplement the events generated using matrix elements with shower development, which accounts for higher order corrections. The matrix elements at each parton multiplicity are calculated at a given order in perturbative calculation, typically tree level, and the different multiplicity samples are combined into an inclusive sample by weighting them by their corresponding matrix element cross section.

The addition of the parton shower to the inclusive sample might lead to a double counting of events: if the parton shower produces an extra jet to an n-parton event, this event will overlap with the contribution coming from the $n + 1$-parton sample. ALPGEN, the inclusive boson generator used in this analysis (see Section 7.1) uses the MLM matching to remove overlapping contributions. It is based in the separation of the phase space covered by the matrix element and that of the parton shower. The matching proceeds in three steps: First, the inclusive sample is divided into the unweighted exclusive samples. Then, the parton shower is applied to each exclusive sample. A jet algorithm is run on the final parton configuration and the original n partons are matched to a partonic jet if some condition (typically $\Delta R(jet, parton) < R_{jet}$ in cone algorithms of radius R) is fulfilled. If all partons are matched and there are no extra jets, the event is accepted. If the parton shower has produced a hard emission that gives origin to an additional jet, the event is rejected. Finally, the events with different jet multiplicities are combined into an inclusive sample. The strategy is modified in the highest multiplicity sample, allowing more jets after parton shower than the original number of partons, to make the combined sample really inclusive.

The inclusive Z contribution is of order ten times smaller than that of W and, since its final state is rather different than that of $\mathrm{t\bar{t}}$ (two high-p_{T} leptons or large $E_{\mathrm{T}}^{\mathrm{miss}}$ contributions) it is easier to suppress.

3.2.2 QCD Multi-jet Production

QCD multi-jet events are another important source of background due to their huge cross-section. Although in principle their final state is different than that of $\mathrm{t\bar{t}}$ signal,

they can contribute to the signal selection if the reconstructed missing energy in the event is sufficiently large and a (fake) lepton is reconstructed. Thus, QCD multi-jet background can arise from various sources:

- Jets mis-reconstructed as electrons if a relatively high fraction of their energy is in the electromagnetic calorimeter.
- Photons inside jets undergoing conversions to electrons.
- Real electrons or muons produced in the decays of heavy flavour inside jets.

The muon case is simpler than the electron one since only semi-leptonic b-jet decays or hadron decays in flight will lead to misidentification. These processes are difficult to model, and data-driven techniques have been developed to extract this contribution directly from data (see Sec. 7.5).

3.2.3 Single Top

Even though the single top production cross-section is smaller than that of $t\bar{t}$, their final states can be similar. There are three single top production processes in pp collisions: t-channel with $\sigma_{t-chan} = 64.2 \pm 2.6$ pb, Wt-production with $\sigma_{Wt-chan}$ 15.6 ± 1.3 pb and s-channel with $\sigma_{s-chan} = 4.6 \pm 0.2$ pb [53] [54] [55] (see Fig.3.8).

3.2.4 Dibosons

Diboson production ($W\ W$, $W\ Z$, $Z\ Z$) is the smallest background to top quark pair production. The main contribution comes from $W\ W$, with one W decaying hadronically and the other leptonically, and with additional jets produced via initial or final state radiation [56].

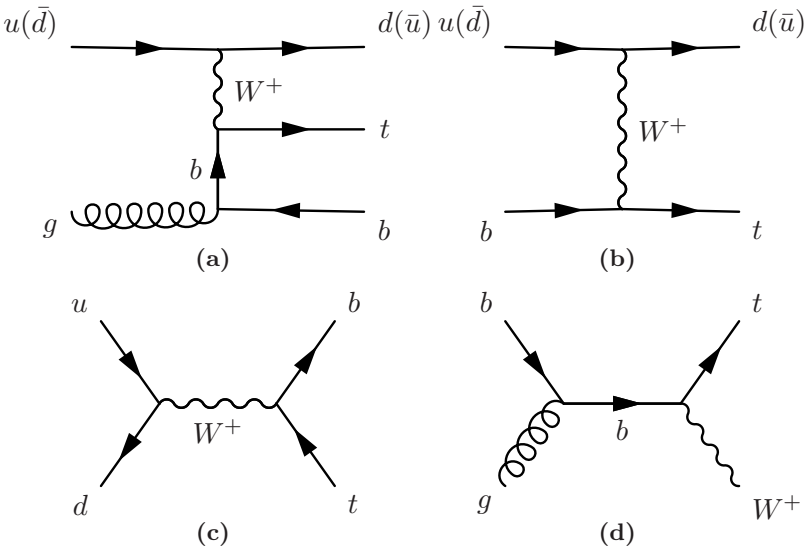

Figure 3.8: The Feynman diagrams for single top quark production: (a) and (b) t-channel, (c) s-channel, and (d) associated production (Wt-channel).

4

Event generation

Fig. 4.1 sketches the different processes occurring in a proton-proton collision. The main process is the hard scattering, which takes place when two incoming partons collide producing a given number of outgoing high transverse momentum partons. Before and after the hard scatering, both initial and final states can radiate, processes known as initial and final state radiation (ISR/FSR). Hard scattering and ISR/FSR involve high momentum transfers and can be calculated perturbatively. The breakup of the colliding protons which do not take part in the hard interaction can also interact. These interactions are referred to as underlying event [57] [58]. The outgoing partons branch into other partons in a cascade of quark-antiquark pairs and gluons in a process known as parton shower. Due to the color connection, all these semi-hard interactions interfere with the main event and have to be taken into account because they may influence the observables of the final state. At the last stage of the parton shower, the final state partons interact non-perturbatively to form color-neutral hadrons. This process occurs at low energy scales and is known as hadronization or fragmentation. Finally, since at LHC each colliding bunch contains around 10^{11} protons, there is a non-negligible probability that one single bunch crossing may produce several separate events, called pile-up events. The amount of pile-up events increases with the luminosity.

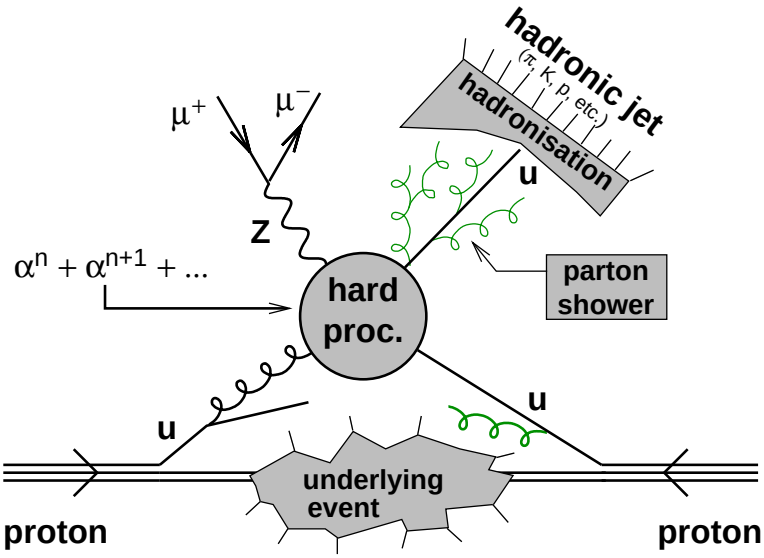

Figure 4.1: Schematic representation of a hard interaction in a proton-proton collision, where initial partons create the hard scattering which subsequently develops a parton shower. The rest of the partons create the underlying event polluting the hard process and making more difficult its reconstruction.

4.1 Hard Process

A typical hard process for top pair production can be seen in Fig. 4.2. Hard processes involve large momentum transfers to produce heavy particles out of the initial partons. These reactions can be described by perturbation theory. Using the factorization theorem, the top quark pair production cross-section in pp collisions can be expressed as

$$\begin{aligned}\sigma_{t\bar{t}}(P_1, P_2) = \sum_{i,j} \int dx_1 dx_2 f_i(x_1, \mu_F^2) f_j(x_2, \mu_F^2) \times \\ \times \sigma_{ij\to t\bar{t}}(x_1, x_2, \alpha_S(\mu_R^2), Q^2/\mu_F^2, Q^2/\mu_R^2)\end{aligned} \tag{4.1}$$

where $f(x_i, \mu_F)$ are the PDFs already introduced in Sec. 3.1, and $\sigma_{ij\to t\bar{t}}$ denotes the parton level cross section of the initial two-parton interaction to the two-parton final state, in leading order (LO) approach. Both, the PDF and $\sigma_{ij\to t\bar{t}}$ depend on the momentum fraction of the initial partons, x_i, and the factorization scale μ_F. Q^2 is the four-momentum transfer. The dependence of any observable on μ_F is given by the

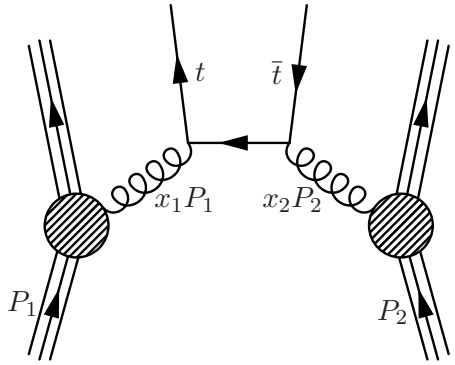

Figure 4.2: The predominant production mechanism of top pairs at LHC: gluons inside two colliding protons annihilate to produce a top-antitop pair.

terms included in the perturbative expansion: the more terms are included, the weaker the dependence on μ_F is.

The cross section for the hard scattering $\sigma_{ij\to t\bar{t}}$ is calculated in powers of the strong coupling constant α_S, and describes the short distance interaction of the incoming partons. This cross section depends directly on the matrix element squared of the $2 \to 2$ process, calculable from the sum over the Feynman diagrams at LO, shown in Figs. 3.2 and 3.3. For higher order diagrams, ultraviolet divergences can be isolated by the renormalization procedure, which introduces the renormalization scale, μ_R. The choice of μ_R is arbitrary, but in most MC generators it is common to choose $\mu_R = \mu_F = Q^2$, and to vary μ_R and μ_F, usually by using twice and half values of the scales, to estimate the uncertainty associated by the choice.

4.2 Parton Showers

As we have seen, the hard process involves large momentum transfers and therefore the partons involved in it emit QCD radiation in form of gluons. Since gluons themselves also carry colour charges, they can emit further radiation, leading to the formation of parton showers. Parton showers describe the evolution in momentum transfer from the high scales associated with the hard process down to the low scales, of order 1 GeV, associated with the confinement of the partons.

The parton interactions at first order in α_S are described by three possible processes: gluon radiation ($q \to qg$), gluon splitting ($g \to gg$) and quark pair production ($g \to q\bar{q}$).

The Dokshitzer-Gribov-Lipatov-Altarelli-Parisi [59] [60] [61] splitting functions $P_{ab}(r)$ describe the probability that a parton of type b radiates a quark or a gluon and becomes a parton of type a, carrying a fraction r of the parton b momentum. The evolution of the quark and gluon densities can be written as a function of the splitting functions. In principle, the showers represent the higher-order corrections to the hard subprocess. In practice, it is not feasible to calculate these corrections exactly and an approximation scheme is used in which the dominant contributions are included at each order.

The splitting process $i \to j + k$ cannot take place with all partons on their mass-shells. The dominant contributions will come from configurations in which the virtualities are strongly ordered, with the parton nearest to the hard process farthest from its mass shell and the virtualities falling sharply as the shower evolves away from it. The upper limit on the initial virtuality is set by some momentrum transfer scale $q^2 < Q^2$, and the shower is terminated when the virtualities reach the hadronization scale, $q^2 \sim 1$ GeV.

Parton showers are built on soft and collinear approximations, while many of the observables we are interested in are explicitly sensitive to hard wide-angle emissions and multi-jet final states, which can only be described accurately with the help of high-order matrix elements. Also, they can not be extended arbitrarily far to the infrared region where QCD becomes strong interacting.

4.3 Hadronization

QCD perturbation theory is valid for the description of the partons outgoing from the hard scattering process. But with increasing distance, the strong interaction becomes very strong and the perturbative approach breaks down. In this regime, quarks and gluons combine to form the colorless hadronic final state. Final hadrons are collimated in a small angular region in the direction of the original parton. In such region a jet can be defined, aiming to collect the parton's daughters and therefore conserving the original parton kinematic properties. Since the hadronization process cannot be calculated from perturbative QCD, it has to be modeled and subsequently tuned to data.

Two main hadronization models are currently in use: the string model and the cluster model. The main difference among the two is that the former transforms partonic

systems directly into hadrons, while the latter employs an intermediate stage of cluster objects, with a typical mass scale of a few GeV.

The string method is based on the assumption of linear confinement. Let's consider the production of a back-to-back quark pair. As the quarks move apart, a colour flux tube stretches between them, as seen in Fig. 4.3 (a). When the quarks move further apart from the creation vertex, the potential energy stored in the string increases, and the string may break by the production of a new quark pair, so that the system splits into two colour-singlet systems. If the invariant mass of either of these systems is large enough, further breaks may occur (Fig. 4.3 (b)). At the end of the process, the string has broken into a set of quark-antiquark pairs that fragment into hadrons.

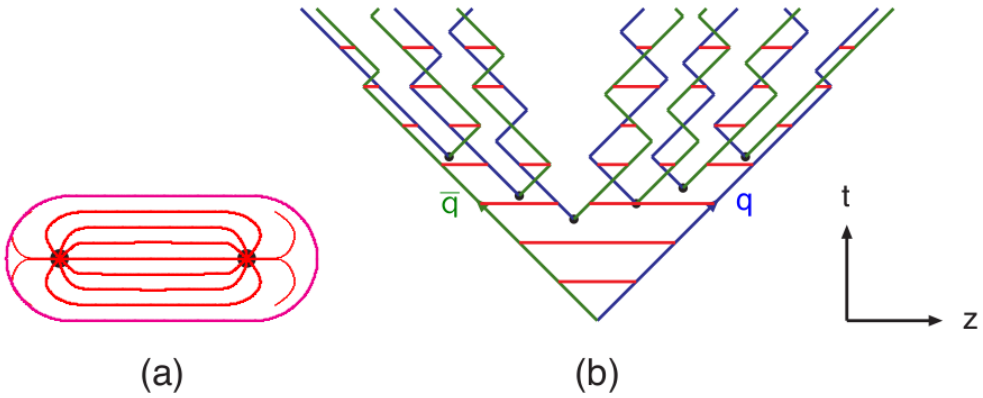

Figure 4.3: (a) A flux tube is created when two quarks are pulled apart. (b) Schematic representation of the string algorithm: Motion and breakup of a string system where diagonal lines are (anti) quarks and horizontal ones snapshots of the string field.

The cluster model is based on the preconfinement propertiy of parton showers, which leads to colour-singlet parton clusters with a mass distribution independent of the scale Q and the nature of the hard process. To leading order in N_c (number of colors) gluons can be represented by pairs of colour-anticolour lines as seen in Fig. 4.4. Clusters are formed of nearby quarks while remaining gluons are split into quark-antiquark pairs. Each cluster decays into hadrons depending on the phase space available to the decay products.

The MC samples employed in this thesis use PYTHIA, based on the string model, or HERWIG, based on the cluster model, as fragmentation models.

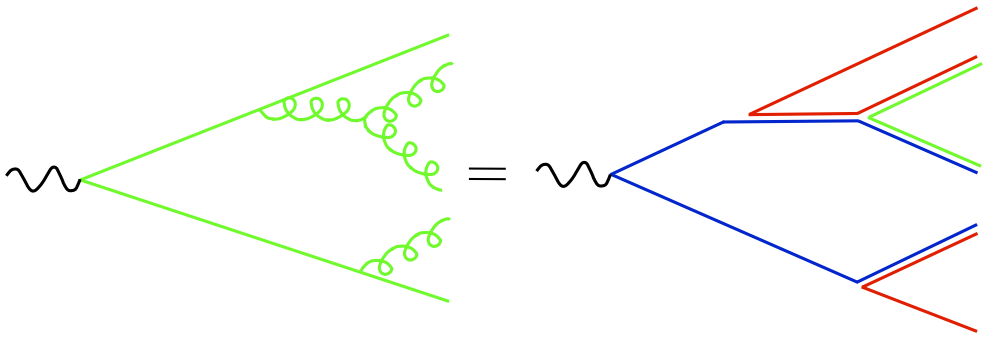

Figure 4.4: Color structure of a parton shower to leading order in N_c.

4.4 Underlying Event

The beam-beam remnants are what is left over after a parton is knocked out of each of the two initial beam hadrons. Thus, the underlying event arises from collisions between those partons that do not directly participate in the hard process, but contribute to the final state. Their interaction happens at low transfer momentum and involves flavour and color connections to the hard scattering, therefore it cannot be descibed perturbatively.

5

LHC and ATLAS Detector

This chapter briefly introduces CERN's accelerators and the ATLAS detector layout and sub-systems. CERN, the European Organization for Nuclear Research founded in 1954, is one of the largest centers for scientific research of the world. At CERN, the biggest and most complex scientific instruments are used to study the basic constituents of matter, the fundamental particles. Accelerators boost beams of particles to high energies before they are made to collide with each other or with stationary targets. Detectors observe and record the results of these collisions.

5.1 LHC Machine

The Large Hadron Collider (LHC) [62] is located in a tunnel of a circumference of 27 km, as deep as 175 m beneath the Franco-Swiss border near Geneva, Switzerland. It is designed to collide opposing particle beams of either protons or heavy ions at up to 14 TeV.

On September 10^{th} 2008, the proton beams were successfully circulated in the main ring of the LHC for the first time, but nine days later operations were halted due to a magnet quench incident resulting from an electrical fault. The following helium gas explosion damaged over 50 superconducting magnets and their mountings, and contaminated the vacuum pipe. On November 20^{th} 2009 beams were successfully circulated again, with the first recorded proton - proton collisions occurring three days later at the injection energy of 450 GeV per beam. On March 30^{th} 2010, the first collisions took place between two 3.5 TeV beams, setting the world record for the highest-energy

particle collisions in accelerators, and the LHC began its planned research program. In 2012 the energy has been increased to 4 TeV per beam.

5.1.1 The Accelerator

Protons are obtained by removing electrons from hydrogen atoms. Prior to being injected into the main accelerator, the particles are prepared by a series of systems that successively increase their energy. The first system is the linear particle accelerator LINAC 2 [63] generating 50 MeV protons, which feeds the Proton Synchrotron Booster (PSB)[64]. There the protons are accelerated to 1.4 GeV and injected into the Proton Synchrotron (PS)[65], where they are accelerated to 26 GeV. Finally the Super Proton Synchrotron (SPS)[66] is used to further increase their energy to 450 GeV before they are at last injected into the main ring. Here the proton bunches are accumulated, accelerated to their peak 3.5 TeV energy, and finally circulated for 10 to 24 hours while collisions occur at the four interaction points. The CERN's accelerator complex can be seen in Fig. 5.1.

The PS has a circumference of 628 m, 277 conventional electromagnets, including 100 dipoles to bend the beams round the ring, and it operates at up to 25 GeV. The SPS is the second largest machine in the CERNs accelerator complex. Measuring nearly 7 km in circumference, it takes particles from the PS and accelerates them to provide beams for the LHC, the COMPASS experiment and the CNGS project. The SPS has 1317 conventional electromagnets, including 744 dipoles to bend the beams round the ring, and it operates at up to 450 GeV.

The LHC 3.8 m wide concrete-lined tunnel, constructed between 1983 and 1988, was formerly used to house the Large Electron Positron Collider. It contains two adjacent parallel beamlines (or beam pipes) that intersect at four points, each containing a proton beam, which travel in opposite directions around the ring. 1,232 dipole magnets keep the beams on their circular path, while 392 additional quadrupole magnets are used to keep the beams focused, in order to maximize the chances of interaction between the particles in the four intersection points, where the two beams will cross. In total, over 1,600 superconducting magnets are installed, most of them weighing over 27 tones. Approximately 96 tones of liquid helium are needed to keep the magnets, made of copper-clad niobium-titanium, at their operating temperature of 1.9 K, making the LHC the largest cryogenic facility in the world at liquid helium temperature.

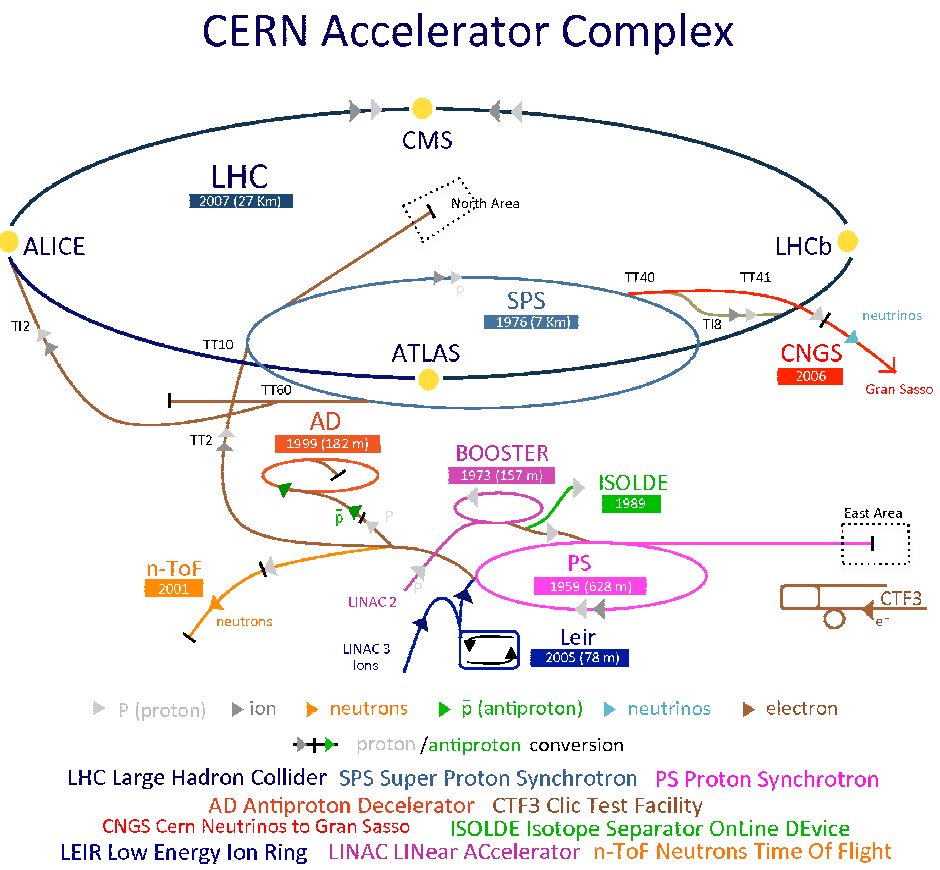

Figure 5.1: CERN accelerator complex

The LHC physics program is mainly based on proton-proton collisions. However, shorter running periods, typically one month per year, with heavy-ion collisions are included in the program. While lighter ions are considered as well, the baseline scheme deals with lead ions. The aim of the heavy-ion program is to investigate the quark-gluon plasma, which existed in the early universe.

5.2 ATLAS Detector

The overall detector layout is shown in Fig.5.2. The magnet configuration is based on an inner thin superconducting solenoid surrounding the inner detector cavity, and large superconducting air-core toroids consisting of independent coils arranged with a an eight-fold symmetry outside the calorimeters. A precise description of the lay-out

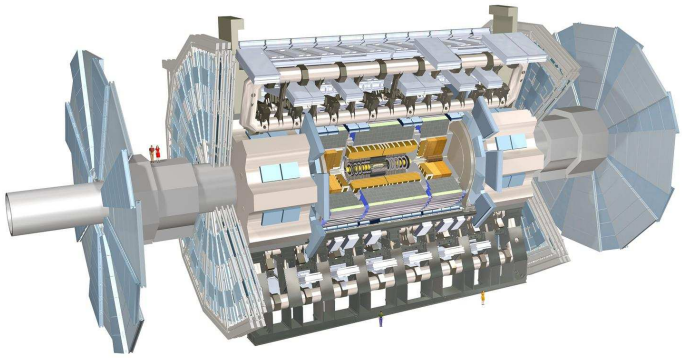

Figure 5.2: Overview of the ATLAS detector.

is given in the following sections. The radial extension of the different subdetectors is summarized in Tab. 5.1. A summary of their coverage and expected resolution is shown in Tab. 5.2.

Table 5.1: Summary of the ATLAS subdetectors, magnets and beam pipe radial extension in the barrel.

Detector component	Radial extension (m)
Beampipe	$0.029 < R < 0.036$
Inner detector (envelope)	$0 < R < 1.15$
Solenoid	$1.23 < R < 1.28$
EM calorimeter	$1.4 < R < 2$
Hadronic calorimeter	$2.28 < R < 4.25$
Toroids	$4.7 < R < 10.05$
Muon spectrometer	$5 < R < 10$

5.2.1 Magnet System

The ATLAS superconducting magnet system is an arrangement of a central solenoid (CS) providing the inner detector with magnetic field, surrounded by a system of three large air-core toroids generating the magnetic field for the muon spectrometer. The

Table 5.2: Summary of the ATLAS subdetectors coverage and expected resolution.

Detector component	$\|\eta\|$ Coverage		Resolution
	Measurement	Trigger	
Inner detector	< 2.5		$\sigma_{p_T}/p_T = 0.05\% p_T \oplus 1\%$
Calorimeters			
Electromagnetic	< 3.2	< 2.5	$\sigma_E/E = 10\%/\sqrt{E} \oplus 0.7\%$
Hadronic barrel/end-cap	< 3.2		$\sigma_E/E = 50\%/\sqrt{E} \oplus 3\%$
Hadronic forward	$3.1 < \|\eta\| < 3.9$		$\sigma_E/E = 100\%/\sqrt{E} \oplus 10\%$
Muon spectrometer	< 2.7	< 2.4	$\sigma_{p_T}/p_T = 10\%$ at $p_T = 1$ TeV

overall dimensions of the magnet system are 26 m in length and 20 m in diameter. The two end-cap toroids (ECT) are inserted in the barrel toroid (BT) at each end and line up with the CS. They have a length of 5 m, an outer diameter of 10.7 m and an inner bore of 1.65 m. The CS extends over a length of 5.3 m and has a bore of 2.4 m. The unusual configuration and large size make the magnet system a considerable challenge requiring careful engineering. The CS provides a central field of 2 T with a peak magnetic field of 2.6 T at the superconductor itself. The peak magnetic fields on the superconductors in the BT and ECT are 3.9 and 4.1 T, respectively. The performance in terms of bending power is characterized by the field integral $\int Bdl$, where B is the azimuthal field component and the integral is taken on a straight line trajectory between the inner and outer radius of the toroids. The BT provides 2 to 6 Tm and the ECT contributes with 4 to 8 Tm in the 0.0-1.3 and 1.6-2.7 pseudorapidity ranges respectively. The bending power is lower in the transition regions where the two magnets overlap. The position of the CS in front of the EM calorimeter demands a careful minimization of the material in order to achieve the desired calorimeter performance. As a consequence, the CS and the LAr calorimeter share one common vacuum vessel, thereby eliminating two vacuum walls.

5.2.2 Inner Detector

The layout of the inner detector (ID) is shown in Fig. 5.3. It combines high-resolution detectors at the inner radii with continuous tracking elements at the outer radii, all contained in the CS, which provides a nominal magnetic field of 2 T.

The momentum and vertex resolution requirements from physics call for high-precision measurements to be made with fine-granularity detectors, given the very large track density expected at the LHC. Semiconductor tracking detectors, using silicon microstrip (SCT) and pixel technologies offer these features. The highest granularity is achieved around the vertex region using semi-conductor pixel detectors. The total number of precision layers must be limited because of the material they introduce, and because of their high cost. Typically, three pixel layers and eight strip layers are crossed by each track. A large number of tracking points is provided by the straw tube tracker (TRT), which provides continuous track-following with much less material per point and a lower cost. The combination of the two techniques gives very robust pattern recognition and high precision in both ϕ and z coordinates. The straw hits at the outer radius contribute significantly to the momentum measurement, since the lower precision per point compared to the silicon is compensated by the large number of measurements and the higher average radius. The relative precision of the different measurements is well matched, so that no single measurement dominates the momentum resolution. This implies that the overall performance is robust. The high density of measurements in the outer part of the tracker is also valuable for the detection of photon conversions and of B^0 decays. The latter are an important element in the signature of CP violation in the B system. In addition, the electron identification capabilities of the whole experiment are enhanced by the detection of transition-radiation photons in the xenon-based gas mixture of the straw tubes. The outer radius of the ID cavity is 115 cm, fixed by the inner dimension of the cryostat containing the LAr EM calorimeter, and the total length is 7 m, limited by the position of the end-cap calorimeters. Mechanically, the ID consists of three units: a barrel part extending over $\pm$ 80 cm, and two identical end-caps covering the rest of the cylindrical cavity. The precision tracking elements are contained within a radius of 56 cm, followed by the continuous tracking, and finally the general support and service region at the outermost radius. In order to give uniform η-coverage over the full acceptance, the final TRT wheels at high z extend inwards to a lower radius than the other TRT end-cap wheels. In the barrel region, the high-precision detector layers are arranged on concentric cylinders around the beam axis, while the end-cap detectors are mounted on disks perpendicular to the beam axis. The pixel layers are segmented in R, ϕ and z, while the SCT detector uses small angle (40 mrad) stereo strips to measure both coordinates, with one set of strips

in each layer measuring ϕ. The barrel TRT straws are parallel to the beam direction. All the end-cap tracking elements are located in planes perpendicular to the beam axis. The strip detectors have one set of strips running radially and a set of stereo strips at an angle of 40 mrad. The continuous tracking consists of radial straws arranged into wheels.

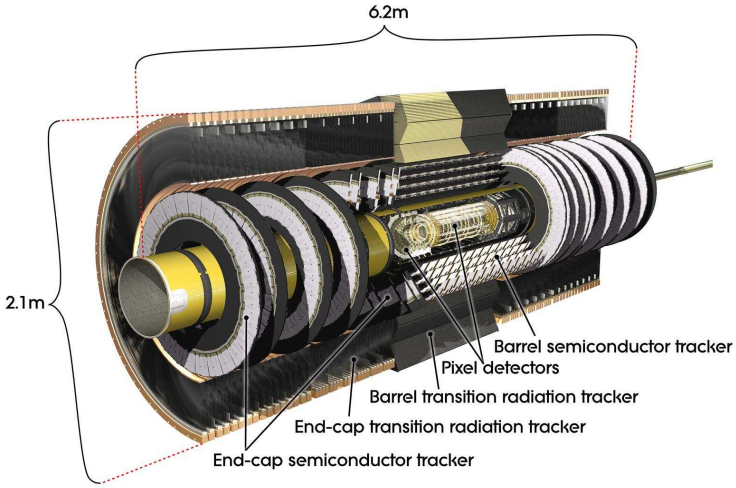

Figure 5.3: Overview of the ATLAS inner detector.

The layout provides full tracking coverage over $|\eta| < 2.5$, including impact parameter measurements and vertexing for heavy-flavour and τ tagging. The secondary vertex measurement performance is enhanced by the innermost layer of pixels, at a radius of about 4 cm, as close as is practical to the beam pipe. The lifetime of such a detector will be limited by radiation damage, and may need replacement after a few years, the exact time depending on the luminosity profile. Physics studies have demonstrated the value of good b-tagging performance during all phases of the LHC operation, for example in the case of Higgs and supersymmetry searches.

5.2.2.1 Pile-up in the ID

The number of inelastic proton-proton interactions per bunch crossing follows a Poisson distribution with mean value μ, which depends on the beam intensity, the increasing emittance * and also varies between bunches. The value of μ increased from five at

* The emittance is a measure for the average spread of particle coordinates in position and momentum phase space.

the start of the fill in early 2011, to more than 15 by the end of the year, as shown in Fig. 5.4. The design specifications of the ID are 25 interactions per bunch crossing. In 2012 the peak number of iterations will be greater than 30. Although pile-up has a significant impact in many areas, the detector design and reconstruction algorithms are sufficiently robust to maintain good performance in such a high pile-up environment.

In data μ is calculated using the following formula:

$$\mu = \frac{L \times \sigma_{incl}}{n_{bunch} \times f_r} \tag{5.1}$$

where L is the instantaneous luminosity, σ_{incl} the total inelastic cross-section, n_{bunch} the number of colliding bunches and f_r the LHC revolution frequency. The uncertainty on μ depends on the uncertainties on the luminosity and the total inelastic cross-section. The first ATLAS measurement of the total inelastic cross section at $\sqrt{s} = 7$ TeV was 60.3 ± 2.1 mb, measured for $\xi > 5 \times 10^{-6}$, where $\xi = M_x^2/s$ is calculated from the invariant mass, M_x, of hadrons selected in the kinematic range $M_x > 15.7$ GeV.

During 2011, the proton bunches were separated by 50 ns, corresponding to twice the LHC design bunch spacing. The impact of the interactions from the same bunch crossing, referred to as in-time pile-up, can be measured from the number of reconstructed vertices on an event-by-event basis. The impact of interactions from neighbouring bunch crossings or out-of-time pile-up, has a much smaller effect due to the timing resolution of the ID.

5.2.2.2 Pixel Detectors

The pixel detector is designed to provide a very high-granularity, high-precision set of measurements as close to the interaction point as possible. The system provides three precision measurements over the full acceptance, and mostly determines the impact parameter resolution and the ability of the ID to find short-lived particles such as B hadrons and τ leptons.

The system consists of three barrels at average radii of ~ 4, 10, and 13 cm, and five disks on each side, between radii of 11 and 20 cm, which complete the angular coverage. The system is designed to be highly modular, containing approximately 1,500 barrel modules and 700 disk modules, and uses only one type of support structure in the barrel and two types in the disks.

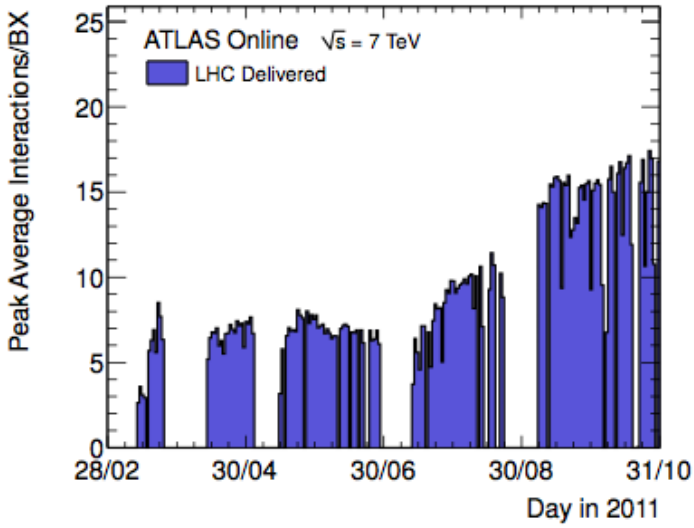

Figure 5.4: The mean number of interactions per bunch crossing in 2011 data.

5.2.2.3 Semiconductor Tracker

The SCT system is designed to provide eight precision measurements per track in the intermediate radial range, contributing to the measurement of momentum, impact parameter and vertex position, as well as providing good pattern recognition by the use of high granularity.

The system is an order of magnitude larger in surface area than previous generations of silicon micro-strip detectors, and in addition must face radiation levels which will alter the fundamental characteristics of the silicon wafers themselves. The barrel SCT uses eight layers of silicon micro-strip detectors to provide precision points in the Rϕ and z coordinates, using small angle stereostrips to obtain the z measurement. Each silicon detector is 6.36×6.40 cm^2 with 768 readout strips of 80 μm pitch. Each module consists of four single-sided p-on-n silicon detectors. On each side of the module, two detectors are wire-bonded together to form 12.8 cm long strips. Two such detector pairs are then glued together back-to-back at a 40 mrad angle, separated by a heat transport plate, and the electronics is mounted above the detectors on a hybrid. The readout chain consists of a front-end amplifier and discriminator, followed by a binary pipeline which stores the hits above threshold until the level-1 trigger decision. The end-cap modules are very similar in construction but use tapered strips, with one

set aligned radially. To obtain optimal η-coverage across all end-cap wheels, end-cap modules consist of strips of either 12 cm length (at the outer radii) or 6-7 cm length (at the innermost radius). The detector contains 61 m^2 of silicon detectors, with 6.2 million readout channels. The spatial resolution is 16 μm in R ϕ and 580 μm in z, per module containing one R ϕ and one stereo measurement. Tracks can be distinguished if separated by more than 200 μm.

5.2.2.4 Transition Radiation Tracker

The TRT is based on the use of straw detectors, which can operate at the very high rates expected at the LHC by virtue of their small diameter and the isolation of the sense wires within individual gas volumes. Electron identification capability is added by employing xenon gas to detect transition-radiation photons created in a radiator between the straws. This technique is intrinsically radiation hard, and allows a large number of measurements, typically 36, to be made on every track at modest cost. However, the detector must cope with a large occupancy and high counting rates at the LHC design luminosity.

Each straw is 4 mm in diameter and is equipped with a 30 μm diameter gold-plated W-Re wire, giving a fast response and good mechanical and electrical properties for a maximum straw length of 144 cm in the barrel. The barrel contains about 50,000 straws, each divided in two at the centre. In order to reduce the occupancy they are read out at each end. The end-caps contain 320,000 radial straws, with the readout at the outer radius. Thus, the total number of electronic channels is 420,000. Each channel provides a drift-time measurement, giving a spatial resolution of 170 μm per straw. The distinction between transition-radiation and tracking signals is obtained on a straw-by-straw basis using separate low and high thresholds in the front-end electronics.

The TRT provides additional discrimination between electrons and hadrons, with e.g. a pion rejection factor at $p_T = 20$ GeV varying with η between 20 and 100 at 90 % electron efficiency.

5.2.3 Calorimeters

A view of the ATLAS calorimeters is presented in Fig. 5.5. The calorimetry consists of an electromagnetic (EM) calorimeter covering the pseudorapidity region $|\eta| < 3.2$, a

hadronic barrel calorimeter covering $|\eta| < 1.7$, hadronic end-cap calorimeters covering $1.5 < |\eta| < 3.2$, and forward calorimeters covering $3.1 < |\eta| < 4.9$.

The EM calorimeter is a lead/liquid-argon (LAr) detector with accordion geometry. Over the pseudorapidity range $|\eta| < 1.8$, it is preceded by a presampler detector, installed immediately behind the cryostat cold wall, and used to correct for the energy lost in the material (ID, cryostats, coil) upstream of the calorimeter. The hadronic barrel calorimeter is a cylinder divided into three sections: one central barrel and two identical extended barrels. It is based on a sampling technique with plastic scintillator plates (tiles) embedded in an iron absorber. At larger pseudorapidities, where higher radiation resistance is needed, the intrinsically radiation-hard LAr technology is used for all the calorimeters: the hadronic end-cap calorimeter, a copper LAr detector with parallel-plate geometry, and the forward calorimeter, a dense LAr calorimeter with rod-shaped electrodes in a tungsten matrix. The barrel EM calorimeter is contained in a barrel cryostat, which surrounds the ID cavity. The solenoid which supplies the 2 T magnetic field to the ID is integrated into the vacuum of the barrel cryostat and is placed in front of the EM calorimeter. Two end-cap cryostats house the end-cap EM and hadronic calorimeters, as well as the integrated forward calorimeter. The barrel and extended barrel tile calorimeters support the LAr cryostats and also act as the main solenoid flux return. The approximately 200,000 signals from the LAr calorimeters leave the cryostats through cold-to-warm feedthroughs located between the barrel and the extended barrel tile calorimeters, and at the back of each end-cap. The electronics up to the digitization stage will be contained in radial boxes attached to each feedthrough and located in the vertical gaps between the barrel and extended barrel tile calorimeters.

5.2.3.1 Electromagnetic Calorimeter

The EM calorimeter is divided into a barrel part ($|\eta| < 1.475$) and two end-caps ($1.375 < |\eta| < 3.2$). The barrel calorimeter consists of two identical half-barrels, separated by a small gap (6 mm) at z = 0. Each end-cap calorimeter is mechanically divided into two coaxial wheels: an outer wheel covering the region $1.375 < |\eta| < 2.5$, and an inner wheel covering the region $2.5 < |\eta| < 3.2$. The EM calorimeter is a lead LAr detector with accordion-shaped kapton electrodes and lead absorber plates over its full coverage. The accordion geometry provides complete ϕ symmetry without azimuthal cracks. The

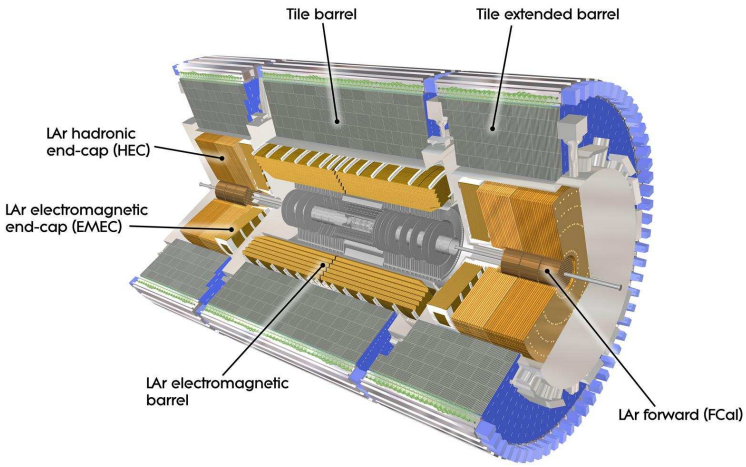

Figure 5.5: Overview of the ATLAS calorimeters.

lead thickness in the absorber plates has been optimized as a function of η in terms of EM calorimeter performance in energy resolution. The LAr gap has a constant thickness of 2.1 mm in the barrel. In the end-cap, the shape of the kapton electrodes and lead converter plates is more complicated, because the amplitude of the accordion waves increases with radius. The absorbers have constant thickness, and therefore the LAr gap also increases with radius. The total thickness of the EM calorimeter is > 24 radiation lengths (X_0) in the barrel and > 26 X_0 in the end-caps.

5.2.3.2 Hadronic Calorimeters

The ATLAS hadronic calorimeters cover the range $|\eta| < 4.9$ using different techniques best suited for the widely varying requirements and radiation environment over the large η-range. Over the range $|\eta| < 1.7$, the iron scintillating-tile technique is used for the barrel and extended barrel tile calorimeters and for partially instrumenting the gap between them with the intermediate tile calorimeter (ITC). This gap provides space for cables and services from the innermost detectors. Over the range $1.5 < |\eta| < 4.9$, LAr calorimeters were chosen: the hadronic end-cap calorimeter (HEC) extends to $|\eta| < 3.2$, while the range $3.1 < |\eta| < 4.9$ is covered by the high-density forward calorimeter (FCAL). Both the HEC and the FCAL are integrated in the same cryostat as that housing the EM end-caps. An important parameter in the design of the hadronic

calorimeter is its thickness: it has to provide good containment for hadronic showers and reduce punch-through into the muon system to a minimum. The total thickness is 11 interaction lengths (λ) at $\eta = 0$, including about 1.5 λ from the outer support, which has been shown both by measurements and simulation to be sufficient to reduce the punch-through well below the irreducible level of prompt or decay muons. Close to 10 λ of active calorimeter are adequate to provide good resolution for high energy jets. Together with the large η-coverage, this will also guarantee a good missing transverse energy measurement, which is important for many physics signatures and in particular for SUSY particle searches.

5.2.3.3 Tile Calorimeter

The large hadronic barrel calorimeter is a sampling calorimeter using iron as the absorber and scintillating tiles as the active material. The tiles are placed radially and staggered in depth. The structure is periodic along z. The tiles are 3 mm thick and the total thickness of the iron plates in one period is 14 mm. Two sides of the scintillating tiles are read out by wavelength shifting (WLS) fibres into two separate photomultipliers (PMTs).

The tile calorimeter is composed of one barrel and two extended barrels. Radially the tile calorimeter extends from an inner radius of 2.28 m to an outer radius of 4.25 m. It is longitudinally segmented in three layers, approximately 1.4, 4.0 and 1.8 interaction lengths thick at $\eta = 0$. Azimuthally, the barrel and extended barrels are divided into 64 modules. In η, the readout cells, built by grouping fibres into PMTs, are pseudo-projective towards the interaction region. The resulting granularity is $\Delta\eta \times \Delta\phi = 0.1{\times}0.1$ ($0.2{\times}0.1$ in the last layer). The total number of channels is about 10,000. The calorimeter is placed behind the EM calorimeter and the solenoid coil. The total thickness at the outer edge of the tile-instrumented region is 9.2 λ at $\eta = 0$.

The barrel cylinder covers the region $\eta < 1.0$. A vertical gap of 68 cm width provides space for cables from the ID, feedthroughs, and service pipes for the EM calorimeter and the CS; it also houses front-end electronics for the EM calorimeter. The extended barrel covers the region $0.8 < \eta < 1.7$. The azimuthal segmentation is as for the barrel, but the radial segmentation differs for the second and third layers. The thickness of the calorimeter in the gap is improved by the ITC, which has the same segmentation as the rest of the tile calorimeter. It is composed of two radial sections attached on the face

of the extended barrel. The outer section, 31 cm thick, starts at the outer radius and covers 45 cm in radius. It is followed by the inner section which is 9 cm thick and extends over 45 cm to lower radii. The ITC is extended further inwards by a scintillator sheet, covering the inner part of the extended barrel and extending to the region between the LAr barrel and end-cap cryostats over $1.0 < \eta < 1.6$. This scintillator samples the energy lost in the cryostat walls and dead material. It is segmented in three sections of $\Delta\eta = 0.2$. The signals produced by the scintillating tiles and collected by the WLS fibers are fast. The PMTs have low dark current and are also fast (rise time and transit time of a few ns). The shaper transforms the current pulse from the PMT into a unipolar pulse of FWHM of 50 ns.

5.2.3.4 Liquid-Argon Hadronic End-cap Calorimeters

Each HEC consists of two independent wheels, of outer radius 2.03 m. The upstream wheel, built out of 25 mm copper plates farther from the interaction point, uses 50 mm plates. In both wheels, the 8.5 mm gap between consecutive copper plates is equipped with three parallel electrodes, splitting the gap into four drift spaces of about 1.8 mm. The readout electrode is the central one, which is a three layer printed circuit, as in the EM calorimeter. The two layer printed circuits on either side serve only as high-voltage carriers. Such a scheme has the same behaviour as a double gap of 4 mm, but without the drawbacks associated with very high voltage (typically 4 kV instead of 2 kV), and ion build up in larger gaps.

Each wheel is built out of 32 identical modules, assembled with fixtures at the periphery, and a central ring. The central (buried) layer of the readout boards features a pad structure which defines the transverse readout granularity. The other layers are made out of a high resistivity coating, with a typical surface resistance of 1 MΩ per square.

Primarily in order to limit the capacitance seen by a single preamplifier, and thus to allow for a fast response, only two gaps are grouped together at the pad level. Miniature coaxial cables running between the sectors carry signals to the preamplifier boards located at the wheel periphery. Output signals from (typically) four preamplifiers are summed together on the same board. A buffer stage drives the output signal up to the cold-to-warm feedthroughs.

Cells defined in this way are fully projective in azimuth, but only pseudo-projective in η. However, the detector envelope is cylindrical, for the sake of mechanical simplicity. To minimize the dip in the material density at the transition between the end-cap and the forward calorimeter (around $|\eta| = 3.1$), the end-cap EM calorimeter reaches $|\eta| = 3.2$, thereby overlapping the forward calorimeter.

5.2.3.5 Liquid-Argon Forward Calorimeter

The FCAL is a particularly challenging detector owing to the high level of radiation it has to cope with. In ATLAS, the forward calorimeter is integrated into the end-cap cryostat, with a front face at about 4.7 m from the interaction point. Compared to layouts with a forward calorimeter situated at much larger distances from the interaction point, the survival of such a calorimeter in terms of radiation resistance is clearly more difficult. On the other hand, the integrated FCAL provides clear benefits in terms of uniformity of the calorimetric coverage as well as reduced radiation background levels in the muon spectrometer.

The FCAL consists of three sections: the first one is made of copper, while the other two are made out of tungsten. In each section the calorimeter consists of a metal matrix with regularly spaced longitudinal channels filled with concentric rods and tubes. The rods are at positive high voltage while the tubes and matrix are grounded. The LAr in the gap between is the sensitive medium. This geometry allows for an excellent control of the gaps which are as small as 250 μm in the first section. While the construction of the copper section does not present special difficulties, the construction of a tungsten calorimeter was a rather new and challenging task. After successful assembly of several prototypes, a technique was chosen based on the assembly of small sintered tungsten alloy pieces. The overall density (including the LAr) of a section built in this way, with 375 μm gaps, is 14.5 g/cm3.

Particular care is needed to support the FCAL in the end-cap cryostat such that the sensitive area is extended down to an angle as small as possible. An external structural tube carries the weight of the forward calorimeter, and withstands the pressure on the cryostat end-walls, while the central cryostat tube near the beam pipe has no structural role. In terms of electronics and readout, four rods are ganged on the detector, and the signal is carried out by polyimide insulated coaxial cables. The total number of channels is 3,584.

5.2.4 Muon Spectrometer

The conceptual layout of the muon spectrometer is visible in Fig. 5.6. It is based on the magnetic deflection of muon tracks in the large superconducting air-core toroid magnets, instrumented with separate trigger and high-precision tracking chambers. Over the range $\eta \leqslant 1.0$, magnetic bending is provided by the large barrel toroid. In the $1.4 \leqslant \eta \leqslant 2.7$ region, muon tracks are bent by two smaller end-cap magnets inserted into both ends of the barrel toroid. Over $1.0 \leqslant \eta \leqslant 1.4$, usually referred to as the transition region, magnetic deflection is provided by a combination of barrel and end-cap fields. This magnet configuration provides a field that is mostly orthogonal to the muon trajectories, while minimizing the degradation of resolution due to multiple scattering. The anticipated high level of particle fluxes has had a major impact on the choice and design of the spectrometer instrumentation, affecting required performance parameters such as rate capability, granularity, ageing properties and radiation hardness. Trigger and reconstruction algorithms have been optimized to cope with the difficult background conditions resulting from penetrating primary collision products and from radiation backgrounds, mostly neutrons and photons in the 1 MeV range, produced from secondary interactions in the calorimeters, shielding material, beam pipe and LHC machine elements.

In the barrel region, tracks are measured in chambers arranged in three cylindrical layers (stations) around the beam axis; in the transition and end-cap regions, the chambers are installed vertically, also in three stations. Over most of the $|\eta|$-range, a precision measurement of the track coordinates in the principal bending direction of the magnetic field is provided by monitored drift tubes (MDTs). At large pseudorapidities and close to the interaction point, cathode strip chambers (CSCs) with higher granularity are used in the innermost plane over $2 < \eta < 2.7$, to withstand the demanding rate and background conditions. Optical alignment systems have been designed to meet the stringent requirements on the mechanical accuracy and the survey of the precision chambers. The precision measurement of the muon tracks is made in the R-z projection, in a direction parallel to the bending direction of the magnetic field; the axial coordinate (z) is measured in the barrel and the radial coordinate (R) in the transition and end-cap regions. The MDTs provide a single-wire resolution of 80 μm when operated at high gas pressure (3 bar) together with robust and reliable operation

thanks to the mechanical isolation of each sense wire from its neighbours. The trigger system covers the pseudorapidity range $\eta \leqslant 2.4$. Resistive plate chambers (RPCs) are used in the barrel and thin gap chambers (TGCs) in the end-cap regions. The trigger chambers for the ATLAS muon spectrometer serve a threefold purpose:

- Bunch crossing identification, requiring a time resolution better than the LHC bunch spacing of 50 ns.
- A trigger with well-defined p_{T} cut-offs in moderate magnetic fields, requiring a granularity of the order of 1 cm.
- Measurement of the second coordinate in a direction orthogonal to that measured by the precision chambers, with a typical resolution of 510 mm.

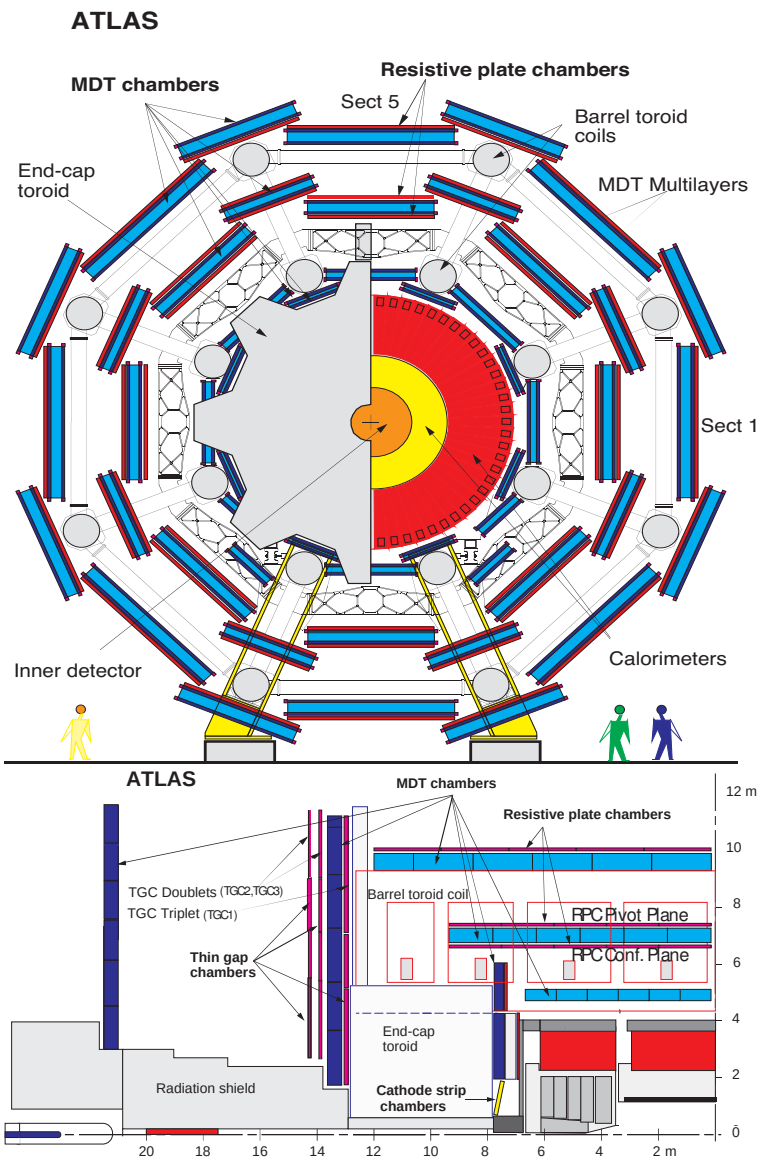

Figure 5.6: Schematic view of the muon spectrometer in the x-y (top) and z-y (bottom) projections.

5.3 Trigger and Data-acquisition System

The ATLAS trigger and data-acquisition (DAQ) system is based on three levels of online event selection. Each trigger level refines the decisions made at the previous level and, where necessary, applies additional selection criteria. Starting from an initial bunch-crossing rate of 40 MHz (interaction rate of $\sim 10^9$ Hz at a luminosity of 10^{34} cm^{-2}s^{-1}), the rate of selected events must be reduced to $\sim$200 Hz for permanent storage.

The level-1 (LVL1) trigger makes an initial selection based on reduced-granularity information from a subset of detectors. High transverse-momentum (high-p_{T}) muons are identified using the trigger chambers, RPCs in the barrel, and TGCs in the end-caps. The calorimeter selections are based on reduced-granularity information from all the calorimeters (EM and hadronic; barrel, end-cap and forward). Objects searched for by the calorimeter trigger are high-p_{T} electrons and photons, jets, and τ-leptons decaying into hadrons, as well as large missing and total transverse energies. In the case of the electron/photon and hadron/ τ triggers, energy isolation cuts can be applied. It is designed for an average output rate of 75 kHz, with an upper limit of 100 kHz.

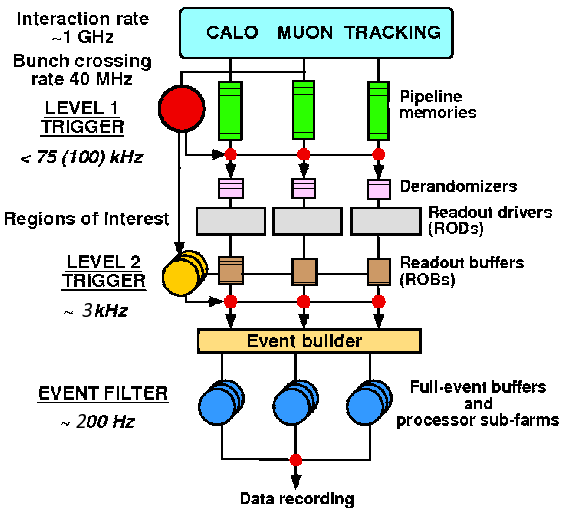

Figure 5.7: Block diagram of the Trigger/DAQ system.

The LVL2 trigger makes use of region-of-interest (RoI) information provided by the LVL1 trigger. This includes information on the position (η and ϕ) and p_{T} of candidate objects (high-p_{T} muons, electrons/γ, hadrons/τ, jets), and energy sums ($E_{\mathrm{T}}^{\mathrm{miss}}$ vector

and scalar E_T value). The RoI data are sent by LVL1 to LVL2, for all events selected by the LVL1 trigger, using a dedicated data path. Using the RoI information, the LVL2 trigger selectively accesses data from the ROBs, moving only the data that are required in order to make the LVL2 decision. The LVL2 trigger has access to all of the event data, if necessary with the full precision and granularity. It is expected that LVL2 will reduce the rate to ∼1 kHz. The latency of the LVL2 trigger is variable from event to event and is in the range 40 ms.

The Event Filter (EF) aims to reduce the event rate to roughly 200 Hz. Since in the EF the available event processing time is of the order of four seconds, the offline analysis procedures (such as algorithms, calibrations and alignments) can be used.

The readout system receives and stores temporally the data in local buffers. The data associated to a RoI is requested by the L2 trigger. Events selected by the L2 are transferred to the event-building system, and later to the EF for the final selection, after which the selected events are moved to permanent storage at the CERN computer center. The events are written to inclusive data *streams* based on the trigger type according to the HLT. There are four primary streams: Egamma, Muon, JetTauETmiss and MinBias. The ATLAS trigger menu defines trigger chains, which start from a L1 item and specify L2 and EF signatures and prescaling values. A trigger signature is each of the features that yield to trigger decision, usually identifying a particle candidate or event properties. There are between 200 and 500 triggers defined in the trigger chain, such that only 1 in N events passing the trigger causes an event to be accepted at that trigger level. L1 items are named in capital letters starting with "L1_", containing info on the kind of object selected ("MU", "EM", "MET", etc.) the energy threshold passed and some information on the isolation. For example, the item L1_EM14 means that an electromagnetic object was found that passed a 14 GeV threshold. EF signatures use non-capital names specifying better the kind of object and identification passe: EF_e15_medium is the signature of an electron object that passes a transverse energy threshold of 15 GeV and the *medium* identification at EF.

5.4 Luminosity Measurement

The luminosity of a pp collider can be expressed as

$$\mathcal{L} = \frac{R_{inel}}{\sigma_{inel}} \tag{5.2}$$

where R_{inel} is the rate of inelastic collisions and σ_{inel} is the pp inelastic cross section. Knowing the revolution frequency (f_r) and the number of bunches that cross at the interaction point (n_b), the above expression can be rewritten as

$$\mathcal{L} = \frac{\mu n_b f_r}{\sigma_{inel}} \tag{5.3}$$

where μ is the average number of inelastic interactions per beam crossing. Thus, the instantaneous luminosity can be determined by any method that measures the ratio μ/σ_{inel}.

To assess and control the systematic uncertainties affecting the absolute luminosity measurement, ATLAS compares the measurements of several luminosity detectors (LUCID and BCM among them), most of which use more than one counting technique. Knowing the efficiency for one inelastic pp collision to satisfy a given event selection criteria (ϵ), the average number of pp collisions which satisfy that event selection is $\mu^{vis} = \epsilon\mu$, and we can rewrite

$$\mathcal{L} = \frac{\mu^{vis} n_b f_r}{\sigma_{vis}} \tag{5.4}$$

where $\sigma_{vis} \equiv \epsilon\sigma_{inel}$ is the visible cross section, and acts as calibration constant which relates the measurable quantity μ^{vis} to the luminosity $\mathcal{L}$. In the limit μ^{vis} much smaller than one, $\mu^{vis} \approx \frac{N}{N_{BC}}$, where N is the number of events passign the selection criteria that are observed during a given time interval, and N_{BC} is the number of bunch crossings in that same interval.

To calibrate the counting techniques, one can use the absolute luminosity as obtained from measured accelerator parameters:

$$\mathcal{L} = \frac{n_b f_r n_1 n_2}{2\pi\Sigma_x\Sigma_y} \tag{5.5}$$

where n_1 and n_2 are the number of protons on each colliding bunch, and Σ_x and Σ_y are the widths of the horizontal and vertical beam profiles. Σ_x and Σ_y are measured

in the so-called *van der Meer* scans. In these scans, the beams are separated by steps of a known distance first in the horizontal and then in the vertical direction. These measurements yield two bell-shaped curves, with maximum at zero separation, from which one extracts Σ_x and Σ_y. The luminosity at zero separation is obtained from Eq. 5.5, and σ_{vis} is extracted from Eq. 5.4 using the measured values of $\mathcal{L}$ and μ^{vis}. In ATLAS van der Meer scans are used to obtain the absolute calibration both for online monitoring and offline analysis.

6

Object Reconstruction

6.1 Track Reconstruction

Tracks are reconstructed in the ID using a sequence of algorithms [67]. The inside-out algorithm is the baseline algorithm designed for the efficient reconstruction of primary charged particles. Primary particles are defined as particles with a mean lifetime greater than 3×10^{-11} s. The inside-out algorithm starts from 3-point seeds in the silicon detectors and adds hits moving away from the interaction point using a combinatorial Kalman filter. Ambiguities in the track candidates found in the silicon detectors are resolved, and tracks are extended into the TRT. The tracks reconstructed by the inside-out algorithm are required to have transverse momentum $p_{\mathrm{T}} > 400$ MeV .

In a second stage, a track search starts from segments reconstructed in the TRT and extends them inwards by adding silicons hits, which is referred to as back-tracking. Back-tracking is designed to reconstruct secondaries, which are particles produced in the interactions of primaries. Finally, tracks with a TRT segment but no extension into the silicon detectors are referred to as TRT-standalone tracks. There is a significant impact from pile-up on both back-tracking and TRT-standalone tracks. The increasing detector occupancy due to pile-up can confuse the pattern recognition algorithm such that the track is not correctly reconstructed. Increased occupancy can lead to an increase of combinatorial fake tracks, i.e. reconstructed tracks which could not be matched to either a primary or secondary particle. However, fake tracks can be minimized by tightening the quality requirements on reconstructed tracks. A set of robust requirements is therefore defined by selecting tracks with at least nine hits in

the silicon detectors (pixel+SCT) and exactly zero holes in the pixel detector. A hit is a measurement point assigned to a track and a hole is a non-existing but expected measurement point for a given track trajectory. For 2011 data only seven silicon hits and at most two holes in the pixel detector were required.

The track reconstruction efficiency is defined as the fraction of primary particles with $p_{\mathrm{T}} > 400$ MeV and $|\eta| < 2.5$ matched to reconstructed tracks. The matching criterion is based on the fraction of hits on the track in each sub-detector that were produced by the primary particle. The contributions from each sub-detector are weighted by a scale factor to account for the differences in the expected number of hits per track and the contribution of each hit to the reconstructed track parameters.

6.2 Vertex Reconstruction

The reconstruction of the interaction vertex is based on the reconstruction of charged-particle tracks in the ATLAS ID. The reconstruction of primary vertices is organized in two steps:

- The primary vertex finding algorithm, dedicated to associate reconstructed tracks to the vertex candidates.
- The vertex fitting algorithm, dedicated to reconstruct the vertex position and its corresponding error matrix. It also refits the associated tracks constraining them to originate from the reconstructed interaction point.

The reconstructed tracks fulfilling the following quality requirements are used for the primary vertex reconstruction:

- $p_{\mathrm{T}} > 150$ MeV ,
- $|d_0| < 4$ mm,
- $\sigma(d_0) < 5$ mm,
- $\sigma(z_0) < 10$ mm,
- at least 4 hits in the SCT detector,
- at least 6 hits in the pixel and SCT detectors.

where d_0 and z_0 denote the transverse and longitudinal impact parameters of tracks with respect to the center of the luminous region, and $\sigma(d_0)$ and $\sigma(z_0)$ denote the corresponding uncertainties as estimated in the track fit. The luminous region in ATLAS is determined during a physics run, typically every 10 minutes, by applying an unbinned maximum likelihood fit to the distribution of primary vertices recorded in this period of time, where the same primary vertex reconstruction algorithm is used, but without applying the beam-spot constraint. The selection criteria are based on impact parameters to remove a good fraction of tracks originating from secondary interactions. According to PYTHIA MC, the above requirements are fulfilled by more than 80 % of the reconstructed tracks corresponding to primary particles.

The *Iterative Vertex Finding* approach works as follows:

- Reconstructed tracks compatible with originating from the interaction region are pre-selected according to the criteria listed above.

- A vertex seed is found by looking for the global maximum in the distribution of z coordinates of the tracks, computed at the point of closest approach to the beam spot center.

- The vertex position is determined using the adaptive vertex fitting algorithm, which takes as input the seed position and the tracks around it. The adaptive vertex fitter is a robust χ^2-based fitting algorithm which deals with outlying track measurements by down-weighting their contribution to the overall vertex χ^2. The down-weighting is performed progressively, while the fit iterations proceed according to a fixed number of steps.

- Tracks incompatible with the vertex by more than approximately seven standard deviations are used to seed a new vertex. The compatibility of the track to the vertex is expressed in terms of a χ^2 with 2 degrees of freedom. The present cut is $\chi^2 > 49$. This procedure is repeated until no unassociated tracks are left in the event or no additional vertex can be found. The very loose cut of $\chi^2 > 49$ is intended to reduce the number of single vertices split into two due to the presence of outlying track measurements.

In standard reconstruction, the parameters of the beam-spot are used both during the finding step to preselect compatible tracks, and during the fitting step to constrain the vertex fit. The transverse beam-spot in the 7 TeV runs varied between approximately 60 μm for the first run to about 30 μm for the later runs with squeezed beams. A small increase in the width during the fills due to the growth in emittance of the beams was also observed. The longitudinal bunch length results in a luminous region size of approximately 20 to 40 mm, depending on the machine parameters. In the vertex fit, the beam-spot constraint has a significant impact on vertices reconstructed out of very few tracks. There the transverse resolution is dominated by the beam-spot information. The typical resolution of a low multiplicity vertex ($>$ 100 μm) is in fact significantly worse than the transverse beamspot width (30-60 μm). However, in the z direction, the length of the luminous region has no visible effect on the longitudinal resolution of the primary vertices, which is determined from the intrinsic longitudinal track resolution of the primary tracks; the only effect of the beam-spot constraint is to remove far outliers. The level of expected (in-time) pile-up is sufficiently low, with an average number of interactions per bunch crossing of less than 0.2, so that it is expected to have no significant impact on the vertex resolution.

6.3 Electrons

The standard electron reconstruction procedure is based on clusters reconstructed in the EC, which then are associated to tracks of charged particles reconstructed in the ID [68]. This algorithm has been developed to allow for an optimal reconstruction of the four-momentum of electrons in the full momentum and pseudorapidity range and for any luminosity. Information from both detectors is used to allow electrons to be identified with the lowest possible amount of backgrounds, keeping in mind that the optimal point between identification efficiency and background rejection depends on the analysis. Electron reconstruction begins with the creation of a preliminary set of seed clusters. Seed clusters with energies above 2.5 GeV are formed by a sliding window algorithm, with a window size of 3$\times$ 5 in η/ϕ middle layer cell units (0.025$\times$0.025). After an energy comparison, duplicated clusters are removed from nearby seed clusters. In the region of the tracker detectors ($|\eta|$ <2.5), an electron is defined by the existence of one or more reconstructed tracks matched to a seed cluster. The track-to-cluster

matching thus forms the central part of the electron reconstruction. Reconstructed tracks are matched to seed clusters by extrapolating them from their last measurement point to the second layer of the calorimeter. The impact point η and ϕ coordinates are then compared to the corresponding seed cluster η and ϕ in that layer. If their difference is below a certain threshold then the track is considered matched to the cluster.

There is an inherent ambiguity between a prompt electron and a converted photon, since both objects are characterized by the existence of tracks pointing to an electromagnetic cluster. In the current reconstruction strategy, objects that have tracks matched to seed clusters will subsequently be treated as electrons. As a result almost all converted photons will be handled as electrons during this stage of the reconstruction and end up in the electron container. This results in a significant contamination of the electron sample by converted photons but on the other hand ensures a high electron reconstruction efficiency. The particle identification criteria will be able to select the prompt electrons from the original electron candidates sample.

Electromagnetic showers characterized by tracks matched to the seed cluster are considered as electron candidates. The electromagnetic cluster is then recomputed using a 3×7 (5×5) sliding window in η/ϕ middle layer cell units in the barrel (end caps). A 3×5 seed cluster size is explicitly chosen to be a subset of the final electromagnetic cluster sizes and, with a 2.5 GeV threshold, improves the reconstruction efficiency of low energy clusters and lowers the duplicate cluster rate. Several corrections to the reconstructed cluster energy are then applied. Finally the electron four-momentum is computed using in addition the track information from the best track matched to the original seed cluster. The energy is computed as a weighted average between the cluster energy and the track momentum. The ϕ and η directions are taken from the corresponding track parameters unless the track contains no silicon hits, in which case η is provided by the cluster η-pointing. In cases where the track has only TRT hits, the ϕ position is taken from the track and the η is provided by the cluster η-pointing.

6.4 Muons

The ATLAS detector is optimized for muon identification, with an efficiency greater than 95% and a fractional momentum resolution better than 3% over a wide transverse

momentum range and raising to 10% at $p_{\mathrm{T}} = 1$ TeV. Muon momenta are independently measured in the ID and the MS (see Sec. 5.2.4).

6.4.1 Muon Identification Strategies

In ATLAS four kinds of muon candidates are distinguished depending on the way they are reconstructed:

- *Stand-alone muon:* The muon trajectory is only reconstructed in the MS. The muon momentum measured in the MS is corrected for the parametrized energy loss of the muon in the calorimeter, to obtain the muon momentum at the interaction point. The direction of flight and the impact parameter of the muon at the interaction point are determined by extrapolating the spectrometer track back to the beam line.

- *Combined muon:* The momentum of the stand-alone muon is combined with the momentum measured in the ID. The muon trajectory in the ID also provides information about the impact parameter of the muon trajectory with respect to the primary vertex.

- *Segment tagged muon:* A trajectory in the inner detector is identified as a muon if the trajectory extrapolated to the MS can be associated with straight track segments in the precision muon chambers.

- *Calorimeter tagged muon:* A trajectory in the ID is identified as a muon if the associated energy depositions in the calorimeters are compatible with the hypothesis of a minimum ionizing particle.

6.5 Jets

Data and MC simulation jets are reconstructed using the anti-kt [69] algorithm with distance parameters R = 0.4 (or R = 0.6) using the FASTJET software [70]. The input to calorimeter jets can be topological calorimeter clusters (topoclusters) or calorimeter towers. Only topoclusters or towers with a positive energy are considered as input to jet finding.

6.5.1 Topological Calorimeter Clusters

Topological clusters are groups of calorimeter cells that are designed to follow the shower development taking advantage of the fine segmentation of the ATLAS calorimeters. The topoclusters formation algorithm starts from a seed cell, whose signal-to-noise ratio is above a threshold of $S/N > 4$. The noise is estimated as the absolute value of the energy deposited in the calorimeter cell divided by the RMS of the energy distribution measured in events triggered at random bunch crossings. Cells neighbouring the seed (or the cluster being formed) that have a S/N of at least two are included iteratively. Finally, all calorimeter cells neighbouring the formed topocluster are added. The topocluster algorithm efficiently suppresses the calorimeter noise.

The topocluster algorithm also includes a splitting step in order to optimize the separation of showers from different close-by particles: All cells in a topocluster are searched for local maxima in terms of energy content with a threshold of 500 MeV. This means that the selected calorimeter cell has to be more energetic than any of its neighbours. The local maxima are then used as seeds for a new iteration of topological clustering, which splits the original cluster into more topoclusters. A topocluster is defined to have an energy equal to the energy sum of all the included calorimeter cells, zero mass and a reconstructed direction calculated from the weighted average of the pseudorapidities and azimuthal angles of the constituent cells. The weight used is the absolute cell energy and the positions of the cells are relative to the nominal ATLAS coordinate system.

6.5.2 Calorimeter Towers

Calorimeter towers are static, $\Delta\eta \times \Delta\phi = 0.1 \times 0.1$, grid elements built directly from calorimeter cells. ATLAS uses two types of calorimeter towers: with and without noise suppression. Calorimeter towers based on all calorimeter cells are called non-noise-suppressed calorimeter towers in the following. Noise-suppressed towers make use of the topoclusters algorithm, i.e. only calorimeter cells that are included in topoclusters are used. Therefore, for a fixed geometrical area, noise-suppressed towers have the same energy content as the topoclusters. Both types of calorimeter towers have an energy equal to the energy sum of all included calorimeter cells. The formed Lorentz four-momentum has zero mass.

6.5.3 Jet Energy Scale Calibration

Jets are reconstructed at the electromagnetic scale, which is the basic signal scale for the ATLAS calorimeters. It accounts correctly for the energy deposited in the calorimeter by electromagnetic showers. This energy scale is established using test-beam measurements for electrons in the barrel and endcap calorimeters. The absolute calorimeter response to energy deposited via electromagnetic processes has also been validated in the hadronic calorimeters using muons, both from test-beams and produced in-situ by cosmic-rays. The energy scale of the electromagnetic calorimeters has been finally corrected using the invariant mass of $Z \rightarrow ee$ events from collision events.

The goal of the jet energy scale (JES) calibration is to correct the energy and momentum of the jets measured in the calorimeter to those of the jets at the hadronic scale. The hadronic jet energy scale is on average restored using data-derived corrections as well as calibration constants derived from the comparison of the reconstructed jet kinematics to that of the corresponding truth level jets in MC studies. The jet energy scale calibration is then validated with in-situ techniques.

The jet energy calibration corrects for detector effects that affect the jet energy measurement:

- Partial measurement of the energy deposited by hadrons (calorimeter non-compensation).
- Energy losses in inactive regions of the detector (dead material).
- Energy deposits from particles not contained in the calorimeter (leakage).
- Energy deposits of particles inside the true jet that are not included in the reconstructed jet.
- Signal losses in calorimeter clustering and jet reconstruction.

Presently, ATLAS uses a simple calibration scheme that applies jet-by-jet corrections as a function of the jet energy and pseudorapidity to jets reconstructed at the electromagnetic scale. This calibration scheme (called EM+JES) allows a direct evaluation of the systematic uncertainty and is therefore suitable for physics analysis. The additional energy due to multiple proton-proton collisions within the same bunch crossing (pile-up) is corrected before the hadronic energy scale is restored, such that the derivation of the jet energy scale calibration is factorised and does not depend on the

number of additional interactions measured. The EM+JES calibration scheme consists of three subsequent steps as outlined below and detailed in the following subsections:

- *Pile-up correction:* The average additional energy due to additional proton-proton interactions is subtracted from the energy measured in the calorimeters using correction constants obtained from in-situ measurements.
- *Vertex correction:* The direction of the jet is corrected such that the jet originates from the primary vertex of the interaction instead of the geometrical centre of the detector.
- *Jet energy and direction correction:* The jet energy and direction as reconstructed in the calorimeters are corrected using constants derived from the comparison of the kinematic observables of reconstructed jets and those from truth jets in MC simulation.

6.5.3.1 Pile-up Correction

As the level of in-time pile-up increases, the average total energy deposition in the calorimeter also increases. This increase is assumed to be completely independent of the hard-scattering activity and thus independent of the jet p_{T}.

The traditional approach is that pile-up contributes as uncorrelated, soft and diffuse background. An offset correction is derived from minimum bias data as a function of the number of reconstructed primary vertices, N_{PV}, the jet pseudorapididy, η, and the bunch spacing τ, because previous bunch crossings can also affect the energy measurement.

The correction applied to the jet transverse energy (E_{T}) can be written as $E_T^{corrected} = E_T - \mathcal{O}(\eta, N_{PV}, \tau_{bunch})$. The aim of the offset correction is to render the jet calibration independent of the instantaneous luminosity.

6.5.3.2 Vertex Correction

Initially, calorimeter jets are reconstructed using the geometrical centre of the ATLAS detector as reference to calculate the direction of jets and their constituents. For each event, the jet four-momentum is corrected such that the direction of each topo-cluster points back to the primary hard-scattering vertex. The kinematic observables of each

topo-cluster are recalculated using the vector from the primary vertex to the topo-cluster centroid as its direction. The raw jet four-momentum is then redefined as the vector sum of the topo-cluster four momenta.

6.5.3.3 Jet Energy Correction

The final step in the EM+JES jet calibration restores the reconstructed energy to the energy of the MC truth jet. The calibration is derived using all isolated calorimeter jets that have a matching isolated truth jet within $\Delta R = 0.3$. The final JES calibration is first parametrized as a function of uncalibrated jet energy and η. The detector pseudorapidy is used rather than the origin-corrected η used in the analyses, since it more directly correspond to a region of the calorimeter. The EM-scale jet energy response ($\mathcal{R}^{\text{jet}}_{\text{EM}} = E^{\text{jet}}_{\text{EM}}/E^{\text{jet}}_{\text{truth}}$) can be seen in Fig. 6.1 for various energy- and η_{det}-bins.

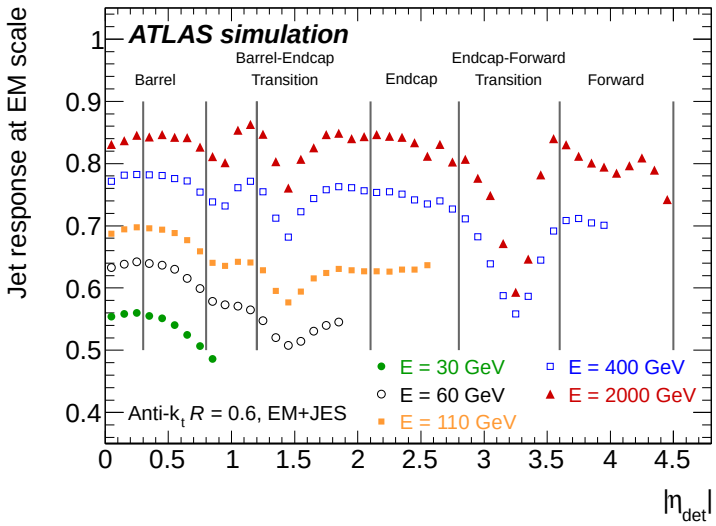

Figure 6.1: Average simulated jet response at the electromagnetic scale as a function of the detector pseudorapidity η_{det} in bins of EM+JES calibrated jet energy. The inverse of the response shown in each bin is equal to the average jet energy scale correction

6.5.3.4 Jet Direction Correction

After the previous corrections, the jet η is further corrected for a bias due to poorly instrumented regions of the calorimeter. In these regions topo-clusters are reconstructed

with a lower energy with respect to better instrumented regions. This causes the jet direction to be biased towards the better instrumented calorimeter regions. The correction is very small ($\Delta\eta < 0.01$) for most regions of the calorimeter, but larger in the transition regions.

6.5.4 Jet Energy Scale Uncertainty

The JES uncertainty is one of the largest uncertainties in almost all analysis in ATLAS. It is derived combining information from the single hadron response in-situ and single pion test-beam measurements, uncertainties on the material budget of the ATLAS detector, the description of the electronic noise, and the MC modelling used in the event generation. The JES systematic uncertainty is determined in the central barrel region $|0.3 < \eta < 0.8|$. The uncertainty for jets beyond this region uses the previous uncertainty as baseline and adds a contribution from the relative calibration with respect to the central region. This choice is motivated by the good knowledge of the detector geometry in the central region, and by the use of test-beam measurements available only for the extension of the Tile calorimeter barrel. The considered contributions to the JES systematic uncertainty are the following:

1. *Uncertainty in the JES calibration.* After the inclusive jet MC sample is calibrated, the jet energy and p_{T} response still shows slight deviations from unity at low p_{T} (non-closure). The systematic uncertainty due to the non-closure of the nominal JES calibration is taken as the larger deviation of the response in either energy or p_{T} from unity.

2. *Uncertainty on the calorimeter response.* The uncertainty of the calorimeter response to jets can be obtained from the response uncertainty of the individual particles constituting the jet. The in-situ measurement of the single particle response significantly reduces the uncertainty due to the limited knowledge of the exact detector geometry, in particular that due to the presence of additional dead material, and the modelling of the exact way particles interact in the detector [71].

3. *Uncertainties due to the detector simulation.* Discrepancies between the simulated noise and the real noise in data can lead to differences in the cluster shapes and to the presence of fake clusters, which affect the jet reconstruction. Also the JES

is affected by possible deviations in the material description as its calibration has been derived to restore the energy lost under the assumption of the geometry simulated in the MC simulation. Simulated detector geometries that include systematic variations of the amount of material have been designed using test-beam measurements in addition to 900 GeV and 7 TeV data.

4. *Uncertainties due to the event modelling in the MC generators.* The contributions to the JES uncertainty from the modelling of the fragmentation, the underlying event and other parameters of the MC event generator are obtained by comparing samples based on ALPGEN+HERWIG+JIMMY and the PYTHIA PERUGIA 2010 tune [72] [73].

5. *Uncertainties due to the relative calibration of the endcap and forward regions.* The relative jet calorimeter response and its uncertainty is studied by comparing the transverse momentum of a well-calibrated central jet and a jet in the forward region in events with only two jets at high transverse momenta (dijets). This uncertainty is uncorrelated with the previous listed and it is treated accordingly [74] [75].

6. *Pileup.* In-time pile-up can produce additional energy deposits that are reconstructed within the jet. The uncertainty in the pile-up corrections can be obtained by varying certain analysis choices and by studying the jet response with respect to the transverse momentum of track jets as a function of the number of primary vertices. This uncertainty is uncorrelated with the previous listed and it is treated accordingly [76].

7. *Flavor.* The fragmentation differences between jets initiated by a quark and jets initiated by a gluon lead to a flavor dependence in the JES. Because the flavor content of the different samples varies, this difference results in an additional flavor-dependent term in the JES uncertainty. This uncertainty is uncorrelated with the previous listed and it is treated accordingly [77].

8. *Close-by jet effects.* The presence of any jets nearby could cause a difference in the jet response, resulting in an additional JES systematic uncertainty [78].

Fig. 6.2 shows the fractional JES systematic uncertainty.

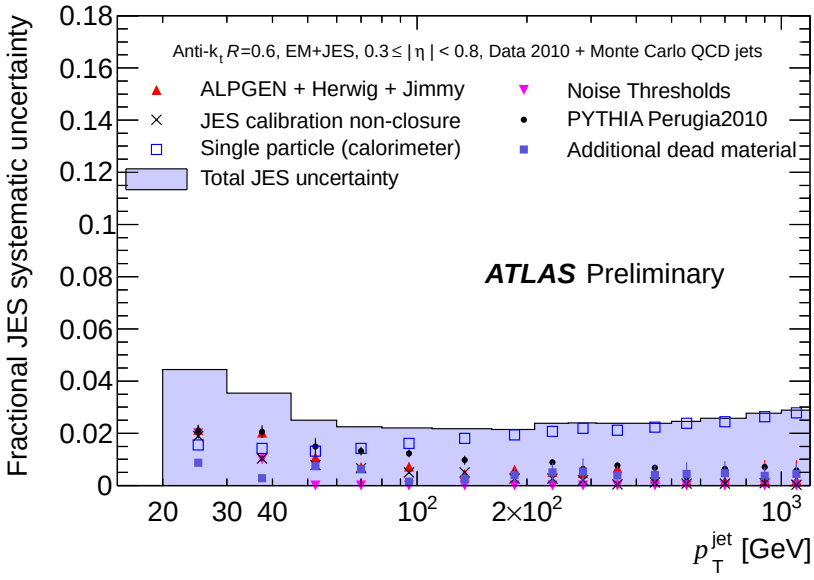

Figure 6.2: Fractional JES systematic uncertainty as a function of p_{T} for jets in the pseudorapidity region 0.3< $|\eta|$ <0.8 in the calorimeter barrel. The total uncertainty is shown as the solid light blue area. The individual sources are also shown, with uncertainties from the fitting procedure if applicable.

6.5.5 B-tagging

The ability to identify jets containing b-hadrons is crucial for this analysis, not only because it leads to a clearer separation between signal and background, but to be able to measure the R_b parameter. A b-jet originates from a b-quark, which produces a b-hadron after fragmentation. B-jets have several characteristic properties that can be utilized to separate them from jets coming from the hadronisation of light quarks. The most important property is the relatively long lifetime of b-hadrons, of about 1.5 ps. This leads to a measurable flight length of a few millimeters before their subsequent decay.

The decay of the b-hadrons also can be identified inclusively by measuring the impact parameters (IP) of tracks coming from their decay, that is, the distance from the point of closest approach of the track to the interaction vertex. The IP is a signed quantity, which is positive if the point of closest approach lies upstream with respect to the jet direction and negative in the other case. The ATLAS tracking system allows the tracks to be measured efficiently and with good accuracy within a pseudorapidity

range of $|\eta| < 2.5$ and down to $p_{\mathrm{T}} = 400$ MeV. For a central track with $p_{\mathrm{T}} = 5$ GeV, which is typical for b-tagging, the transverse momentum resolution is around 75 MeV and the transverse impact parameter resolution is about 35 μm.

The position of the primary interaction point of the proton-proton collision defines the reference point with respect to which impact parameters and vertex displacements are measured. The reconstruction of primary vertices relies on the reconstructed tracks and consists of two stages: first, the vertex finding, which associates reconstructed tracks to the vertex candidates, and second, the vertex fitting, which reconstructs the vertex position and its error matrix. To ensure a good resolution on the vertex position, the primary vertex must be reconstructed from at least five tracks.

Flavor tagging algorithms are defined based on decay lengths, impact parameters, secondary vertices properties and properties of the leptons reconstructed inside the jet. They provide as output a tagging weight, which specifies the probability for a jet to be of a certain flavor. The tagging algorithm used in this analysis, *JetFitter-Comb* results from the combination of two simpler algorithms, *IP3D* and *JetFitter*. The *IP3D* algorithm uses a likelihood ratio technique in which input variables are compared to predefined smoothed and normalized distributions for both the b- and light-jet hypotheses, obtained from MC simulation. The distributions are two-dimensional histograms of the signed transverse and longitudinal impact parameter significances, taking advantage of the correlations between the two variables. The *JetFitter* algorithm exploits the topology of weak b- and c-hadron decays inside the jet. A Kalman filter is used to find a common line on which the primary vertex and the b- and c-vertices lie, as well as their position on this line, giving an approximated flight path for the b-hadron. With this approach, the b- and c-hadron vertices are not necessarily merged, even when only a single track is attached to each of them. The combination of *JetFitter* and *IP3D* is based on artificial neural network techniques with MC simulated training samples and additional variables describing the topology of the decay chain. Fig. 6.3 shows the distribution of the *JetFitterComb* output weight for experimental and simulated data. The shape in experimental data is closely reproduced by the simulation, except in the negative weight region which is dominated by light jets where the impact parameter resolution is poor. In all cases, the tagging rate predicted by the simulation agrees with experimental data to within 20%.

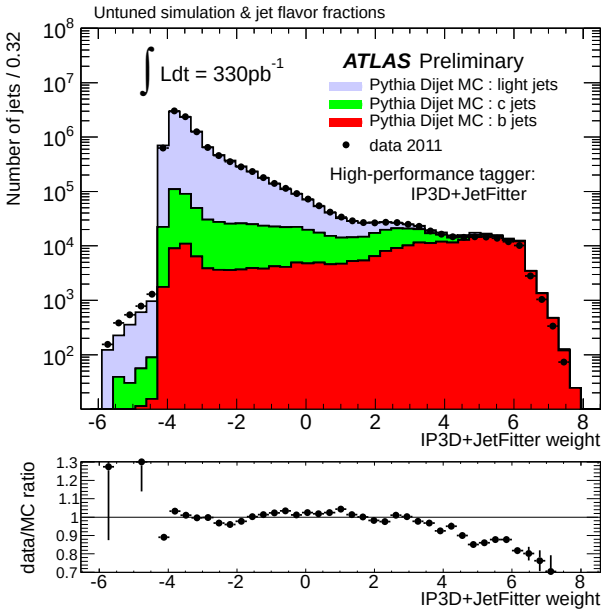

Figure 6.3: Distribution of the output of the IP3D+JetFitter tagging algorithm for experimental data (solid black points) and for simulated data (filled histograms for the various flavors). Jets are from the inclusive leading jet sample. The ratio data/simulation is shown at the bottom of the plot.

6.5.5.1 Calibrating the b-tag Efficiencies and Mistag Rates

In order for b-tagging to be used in physics analysis, the efficiency with which a jet originating from a b-quark is tagged by a b-tagging algorithm needs to be measured. The probability of incorrectly tagging a jet originating from a light-flavour quark or gluon as a b-jet is referred to as the mistag rate [79]. The b-tag efficiencies and mistag rates depend not only on the kinematic variables (η and p_{T}) of the jets, but also on other quantities such as the fraction of jets in the sample originating from gluons. Currently, there is no explicit measurement of the c-tag efficiency available in ATLAS. As both the b- and c-tag efficiencies are dominated by decays of long-lived heavy flavour hadrons, they are expected to show a similar behaviour. However, the systematic uncertainty for the c-tag efficiency scale factor is increased by a factor of two, which is considered to be a conservative value based on simulations.

There are different methods to extract the b-tag efficiency [79]:

1. *The p_T^{rel} method* uses templates of the muon momentum transverse to the jet

axis to fit the fraction of b-jets before and after b-tagging to extract the b-tag efficiency.

2. *The $D^*\mu$ method* explicitly reconstructs the $b \to X\mu D* \to X\mu D^0(\to K\pi)\pi$ decay to obtain a pure sample of b-jets to which the b-tagging algorithm is applied to extract the b-tag efficiency.

3. *The $t\bar{t}$ counting methods* count the number of events after $t\bar{t}$ event selection that have zero, one or two b-tagged jets to extract the b-tag efficiency and the $t\bar{t}$ production cross-section.

4. *The $t\bar{t}$ kinematic selection method* selects a high-purity $t\bar{t}$ sample and extracts the b-tag efficiency from the number of tagged jets together with the expected sample composition.

There are also different approaches to measure the mistag rate:

1. *The SV0 mass method* uses the mass distribution of reconstructed secondary vertices, together with knowledge about the b- and c-tag efficiencies, to determine the fraction of light-flavour jets before and after tagging and hence the mistag rate.

2. *The negative tag method* counts the rate at which secondary vertices with negative decay length significance or tracks with negative impact parameter significances are present in the data and then applies corrections, based on simulation, to translate this negative tag rate into a measurement of the mistag rate.

In the p_T^{rel} method, which is used to calibrate the tagger used in this analysis, the number of b-jets before and after tagging can be obtained for the subset of all b-jets containing a reconstructed muon using the variable p_T^{rel}, which is defined as the momentum of the muon transverse to the combined muon plus jet axis. Muons originating from b-hadron decays have a harder p_T^{rel} spectrum than muons in c- and light-flavour jets. Templates of p_T^{rel} are constructed for b-, c- and light-flavour jets separately, and these are fitted to the p_T^{rel} spectrum of muons in jets in data to obtain the fraction of b-jets before and after requiring a b-tag. The fit is done by adjusting the relative contributions of the b-, c- and light-flavour templates such that their sum

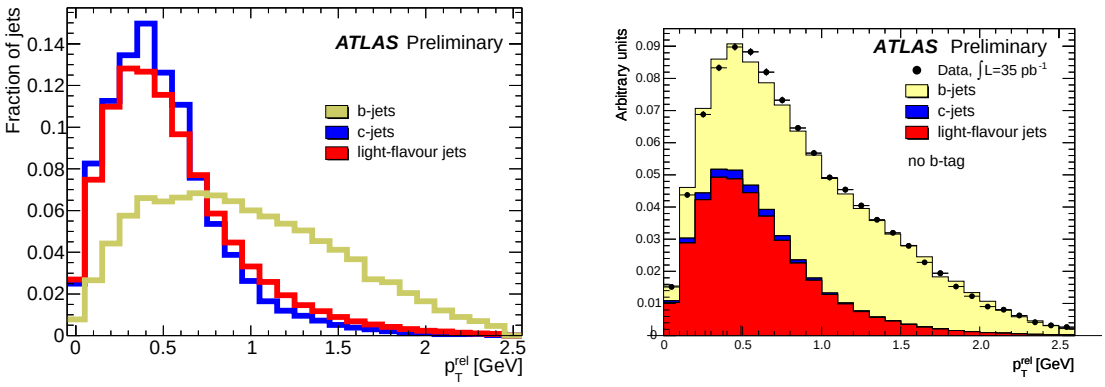

Figure 6.4: (Left-) Examples of p_T^{rel} templates for b-, c- and light-flavour jets. The b- and c-templates have been taken from simulation whereas the light-flavour template has been obtained from data. (Right-) Examples of template fits to the p_T^{rel} distribution in data before b-tagging.

best describes the p_T^{rel} shape in data, as shown in Fig. 6.4. Having obtained the flavour composition of jets containing muons from the p_T^{rel} fits, the b-tag efficiency is defined as

$$\epsilon_b^{data} = \frac{f_b^{tag} \cdot N^{tag}}{f_b \cdot N} \cdot C, \tag{6.1}$$

where f_b and f_b^{tag} are the fractions of b-jets in the pretagged and tagged samples of jets containing muons, and N and N_{tag} are the total number of jets in those two samples. The factor C corrects the efficiency for the biases introduced through differences between data and simulation in the modelling of the b-hadron direction and through heavy flavour contamination of the p_T^{rel} template for light-flavour jets.

The systematic uncertainties affecting the p_T^{rel} method are mainly those that change the shapes of the p_T^{rel} templates used to fit the sample composition. They can either have a direct impact on the p_T^{rel} distribution, or they can indirectly affect the p_T^{rel} distribution by changing the sample composition or the kinematics of the sample.

1. *The p_T^{rel} Template Statistics.* To assess the systematic uncertainty due to the limited statistics available to build the p_T^{rel} templates, 1000 pseudo-experiments were carried out. For each pseudo-experiment, a complete set of pseudo-templates was

created by varying each bin in each template according to a Gaussian distribution with a width reflecting the limited template statistics, and these pseudo-templates were fited to the p_T^{rel} distribution in data. The RMS of the b-tag efficiency distribution of those 1000 pseudo-experiments is taken as the systematic uncertainty.

2. *Modelling of the b-Hadron Direction.* In principle the muon direction resolution also affects p_T^{rel}, but as the muon angular resolution is much higher than that of the jet, the uncertainty associated with this is negligible.

3. *Non-b-Jet Templates* The light-flavour template is obtained from a light-flavour enriched data sample. This template has been compared to a template of muons in light-flavour jets in simulation, and a good agreement was found. However, an influence on the measured efficiency can arise from b-jet contamination in the light-flavour template. The bias introduced by it is corrected for in the final result, and the result of a variation by 25% of the b-jet contamination is taken as systematic uncertainty.

4. *Modelling of b- and c-Production.* In data, b-jets can be produced via several mechanisms: flavour creation, flavour excitation and gluon splitting. In the latter case the angle between the two b-quarks can be so small that both of them end up within the same reconstructed jet. Such b-jets, containing two b-quarks, have a larger probability of being b-tagged than those containing just one b-quark. If the ratio of double-b-jets to single-b-jets is different in data and simulation that would therefore bias the efficiency scale factor measurement. The systematic uncertainty associated with the b-production is estimated by varying the ratio of double-b-jets to single-b-jets in simulation and seeing how much that changes the b-tag efficiency. The systematic uncertainty associated with the c-production is estimated in the same way, namely by varying the ratio of double-c-jets to single-c-jets in simulation and seeing how much that changes the b-tag efficiency.

5. *Modelling of b-Decays.* The muon momentum spectrum in the b-hadron rest-frame, denoted as p*, directly affects the shape of the p_T^{rel} distribution for b-jets. Uncertainties in the modelling of the p* spectrum have to be taken into account and propagated through the analysis.

6. *b-Fragmentation.* An incorrect modelling of the fragmentation in simulation can affect the momentum spectrum of the muons from b-decays and thus alter which muons pass the selection criteria. To investigate the impact of fragmentation, the p_T^{rel} templates were rederived on a simulated sample where the fraction of the b-quark energy carried onto the b-hadron, xb, was changed by 5%. The p_T^{rel} fits were then redone on data using these altered prel templates, and the difference in the b-tag efficiency between this and the default scenario was taken as a systematic uncertainty.

7. *Muon p_{T} Spectrum.* The muon p_{T} spectrum is softer in data than in simulation. To estimate the effect of this mismodelling on the p_T^{rel} measurement, the measurement is repeated after reweighting the muon p_{T} spectrum in simulation to agree with that in data.

8. *Fake Muons in b-Jets.* The p_T^{rel} templates for b-jets are obtained from the simulated QCD μ-jet sample where a muon with $p_{\mathrm{T}}> 3$ GeV is required at generator level. This filter will suppress b-jets containing a fake muon rather than a muon from the b-decay. The fraction of fake muons in the p_T^{rel} templates built from these samples is therefore likely to be lower than in data. To investigate the impact of fake muons on the b-tag efficiency measurement, the p_T^{rel} fits were performed using b-templates with an increased fake muon fraction.

9. *Jet Energy Scale.* A jet energy scale in simulation that is different from that in data would bias the p_{T} spectrum of the simulated events used to build the p_T^{rel} templates. The corresponding systematic uncertainty is obtained by scaling the p_{T} of each jet in the simulation up and down by one standard deviation, according to the uncertainty of the JES, and refitting the data with the modified b- and c-templates as well as rederiving the b-tag efficiency in simulation.

10. *Scale Factor for Inclusive b-Jets.* The p_T^{rel} method can only measure the b-tag efficiency in data for b-jets with a semileptonic b-hadron decay. As these jets always contain the high-momentum and typically well-measured muon track, whereas the hadronic b-jets do not, the b-tag efficiency will be different for these two types of b-jets. The efficiency scale factor derived as the ratio between the semileptonic b-tag efficiency in data and simulation is assumed to be identical for hadronic

b-jets. To investigate the validity of this assumption, the ratio of the weighted averages of the b-tag efficiency for semileptonic and inclusive jets was derived in both data and simulation. The deviation of the double-ratio $SF_{data}^{\mu\to inc}/SF_{sim}^{\mu\to incl}$ from one was taken as systematic uncertainty.

11. *Pileup and Other Time Dependent Effects.* The sensitivity to changing conditions such as the increase in the average number of additional interactions in later run periods has been studied. The b-tag efficiency was found to not depend significantly on the number of primary vertices in the event.

6.6 Missing Transverse Energy

In a collider event the missing transverse momentum is defined as the momentum imbalance in the plane transverse to the beam axis, where momentum conservation is expected. Such an imbalance may signal the presence of unseen particles, such as neutrinos. The vector momentum imbalance in the transverse plane is obtained from the negative vector sum of the momenta of all particles detected in the collision and is denoted as missing transverse momentum, $E_{\mathrm{T}}^{\mathrm{miss}}$.

A precise measurement of $E_{\mathrm{T}}^{\mathrm{miss}}$ is essential for physics at the LHC. A large $E_{\mathrm{T}}^{\mathrm{miss}}$ is a key signature for searches for new physics processes such as supersymmetry (SUSY) or extra dimensions. The measurement of $E_{\mathrm{T}}^{\mathrm{miss}}$ also has a direct impact on the quality of a number of measurements of SM physics, such as the reconstruction of the top-quark mass in $\mathrm{t\bar{t}}$ events.

The $E_{\mathrm{T}}^{\mathrm{miss}}$ reconstruction includes contributions from energy deposits in the calorimeters and muons reconstructed in the muon spectrometer. The two $E_{\mathrm{T}}^{\mathrm{miss}}$ components are calculated as:

$$E_{x(y)}^{\mathrm{miss}} = E_{x(y)}^{\mathrm{miss,calo}} + E_{x(y)}^{\mathrm{miss},\mu}. \tag{6.2}$$

Low p_{T} tracks are used to recover low p_{T} particles which are missed in the calorimeters, and muons reconstructed from the inner detector are used to recover muons in regions not covered by the muon spectrometer. The two terms in the above equation are referred to as the calorimeter and muon terms.

6.6.1 Calculation of the $E_{\mathrm{T}}^{\mathrm{miss}}$ Calorimeter Term

The $E_{\mathrm{T}}^{\mathrm{miss}}$ reconstruction uses calorimeter cells calibrated according to the reconstructed physics object to which they are associated. Calorimeter cells are associated with a reconstructed and identified high-p_{T} parent object in a chosen order: electrons, photons, hadronically decaying τ-leptons, jets and muons. Cells not associated with any such objects are also taken into account in the $E_{\mathrm{T}}^{\mathrm{miss}}$ calculation. Their contribution, named $E_{\mathrm{T}}^{\mathrm{miss,CellOut}}$ hereafter, is important for the $E_{\mathrm{T}}^{\mathrm{miss}}$ resolution.

Once the cells are associated with objects as described above, the $E_{\mathrm{T}}^{\mathrm{miss}}$ calorimeter term is calculated as follows:

$$\begin{aligned} E_{x(y)}^{\mathrm{miss,calo}} = E_{x(y)}^{\mathrm{miss,e}} + E_{x(y)}^{\mathrm{miss},\gamma} + E_{x(y)}^{\mathrm{miss},\tau} + E_{x(y)}^{\mathrm{miss,jets}} \\ + E_{x(y)}^{\mathrm{miss,softjets}} + E_{x(y)}^{\mathrm{miss,calo},\mu} + E_{x(y)}^{\mathrm{miss,CellOut}} \end{aligned} \tag{6.3}$$

where each term is calculated from the negative sum of calibrated cell energies inside the corresponding object, as:

$$\begin{aligned} E_{x}^{\mathrm{miss,term}} &= -\sum_{i=1}^{N_{cell}^{term}} E_i \sin\theta_i \cos\phi_i \\ E_{y}^{\mathrm{miss,term}} &= -\sum_{i=1}^{N_{cell}^{term}} E_i \sin\theta_i \sin\phi_i \end{aligned} \tag{6.4}$$

where E_i, θ_i and ϕ_i are the energy, the polar angle and the azimuthal angle, respectively. The summations performed are over all cells associated with specified objects in the pseudorapidity range $|\eta| < 4.5$.

Because of the high granularity of the calorimeter, it is crucial to suppress noise contributions and to limit the cells used in the $E_{\mathrm{T}}^{\mathrm{miss}}$ sum to those containing a significant signal. This is achieved by using only cells belonging to three dimensional topological clusters, with the exception of electrons and photons for which a different clustering algorithm is used. The various terms in Eq. 6.3 are described in the following:

- $E_{x(y)}^{\mathrm{miss,e}}$, $E_{x(y)}^{\mathrm{miss},\gamma}$, $E_{x(y)}^{\mathrm{miss},\tau}$ are reconstructed from cells in clusters associated to electrons, photons and τ-jets from hadronically decaying τ-leptons, respectively;

- $E_{x(y)}^{\text{miss,jets}}$ is reconstructed from cells in clusters associated to jets with calibrated $p_{\text{T}} > 20$ GeV .
- $E_{x(y)}^{\text{miss,softjets}}$ is reconstructed from cells in clusters associated to jets with 7 GeV$<$ $p_{\text{T}} < 20$ GeV;
- $E_{x(y)}^{\text{miss,calo},\mu}$ is the contribution to $E_{\text{T}}^{\text{miss}}$ originating from the energy lost by the muons in the calorimeter. This term is calculated differently from isolated and non-isolated muons, with non-isolated muons defined as those within a distance $\Delta R = \sqrt{(\Delta\eta)^2 + (\Delta\phi)^2} < 0.3$ of a reconstructed jet in the event.
- $E_{x(y)}^{\text{miss,CellOut}}$ term is calculated from the cells in topoclusters which are not included in the reconstructed objects.

6.6.2 Calculation of the $E_{\text{T}}^{\text{miss}}$ Muon Term

The $E_{\text{T}}^{\text{miss}}$ muon term is calculated from the momenta of muon tracks reconstructed within $|\eta| < 2.7$:

$$E_{x(y)}^{\text{miss},\mu} = -\sum_{muons} p_{x(y)}^{\mu} \tag{6.5}$$

where the summation is over selected muons. In the region $|\eta| < 2.5$, only well-reconstructed muons in the muon spectrometer with a matched track in the ID are considered. The matching requirement considerably reduces contributions from fake muons. These fake muons can sometimes be created in events where some particles from very energetic jets punch through the calorimeter into the muon system.

The p_{T} of an isolated muon is determined from the combined measurement of the ID and MS, taking into account the energy deposited in the calorimeters. In this case the energy lost by the muon in the calorimeters ($E_{x(y)}^{\text{miss,calo},\mu}$) is not added to the calorimeter term to avoid double counting of energy.

For a non-isolated muon, the energy deposited in the calorimeter cannot be resolved from the calorimetric energy depositions of the particles in the jet. The muon spectrometer measurement of the muon momentum after energy loss in the calorimeter is therefore used, so the $E_{x(y)}^{\text{miss,calo},\mu}$ term is added to the calorimeter term. Only in cases in which there is a significant mismatch between the spectrometer and the combined

measurement, the combined measurement is used and a parameterized estimation of the muon energy loss in the calorimeter is subtracted.

For higher values of pseudorapidity ($2.5 < |\eta| < 2.7$), outside the fiducial volume of the ID, there is no matched track requirement and the muon spectrometer p_{T} alone is used for both isolated and non-isolated muons.

Aside from the loss of muons outside the acceptance of the muon spectrometer ($|\eta| < 2.7$), muons can be lost in other small inactive regions (around $|\eta| = 0$ and $|\eta| \sim 1.2$) of the muon spectrometer. The muons which are reconstructed by segments matched to ID tracks extrapolated to the muon spectrometer are used to recover their contributions to $E_{\mathrm{T}}^{\mathrm{miss}}$ in the $|\eta| \sim 1.2$ regions.

7

Simultaneous measurement of the top quark pair production cross-section and R_b

Within the SM, top quarks are predicted to decay to a W boson and a b-quark nearly 100% of the time, and the decay topologies are determined by the decays of the W bosons. A precise measurement of the ratio $R_b = \mathcal{B}(t \to Wb)/\mathcal{B}(t \to Wq)$ with q either a $d-$, $s-$ or $b-$ quark, is sensitive to the hierarchy among the V_{tq} Cabibbo-Kobayashi-Maskawa (CKM) matrix elements since:

$$R_b = \frac{\mathcal{B}(t \to Wb)}{\mathcal{B}(t \to Wq)} = \frac{|V_{tb}|^2}{|V_{tb}|^2 + |V_{td}|^2 + |V_{ts}|^2}. \tag{7.1}$$

This measurement, in combination with the measurements of the single top quark production cross-section in the different modes, would allow model-independent constraints on the magnitudes of the different V_{tq} CKM elements [43]. This measurement can thus help test several extensions of the SM, like vector-like quarks or sequential fourth generation models, in which the 3×3 CKM submatrix does not appear unitary. Furthermore, a precise measurement of the top quark pair ($t\bar{t}$) production cross-section ($\sigma_{t\bar{t}}$) allows precision tests of quantum chromodynamics (QCD), whose predictions for $\sigma_{t\bar{t}}$ are now at the level of 10% [80]. In addition, $t\bar{t}$ production is an important background for physics beyond the SM, and new physics may also give rise to additional $t\bar{t}$ production mechanisms or modifications of the top quark decay channels.

7.1 Data and Simulated Samples

MC simulation samples are used to develop and validate the analysis procedures, to calculate the acceptance for $t\bar{t}$ events, and to evaluate the contributions from some background processes and some sources of systematic uncertainty. After event generation, all samples have been processed with the GEANT4 simulation of the ATLAS detector [81], reconstructed and passed through the same analysis chain as the data.

For the generation of $t\bar{t}$ signal the NLO generator MC@NLO v3.41 [82] is used with an assumed top-quark mass of 172.5GeV and with the NLO parton density function (PDF) set CTEQ66 [83]. MC@NLO is interfaced with HERWIG for fragmentation. This sample was generated with a value $R_b = 1$, *i.e.* with the two t-quarks decaying to Wb. In order to measure R_b, two additional samples have been generated modifying the original one by (i) changing the decay chain of one of the t-quarks to be Wq with q either a d- or a s-quark or (ii) changing the decay chain of the two t-quarks to be Wq. This is accomplished by weighting the events such that they are b tagged at the correct rate for the desired decay mode ($WbWq$ or $WqWq$). While this procedure allows to correctly account for the jet flavor as far as b-tagging rate is concerned, it does not take into account any small difference in selection efficiency between the different types of events ($WbWb$, $WbWq$ or $WqWq$). In order to estimate a suitable correction, a dedicated MC sample was generated using PROTOS [84], including top quark decays to Wb, Wd and Ws with branching ratios of 50%, 25% and 25%, respectively. More information about the procedure is explained in Sec. 7.7.

For W/Z boson production in association with multiple jets, ALPGEN v2.13 [85] is used, which implements the exact LO matrix elements for final states with up to 6 partons*. Using the LO PDF set CTEQ6L1 [83], the following backgrounds are generated: W+jets events with up to 5 partons, Z+jets events with up to 5 partons and with the dilepton invariant mass $m_{\ell\ell} > 40$GeV. For the W+jets processes, separate samples are generated that include $b\bar{b}$ and $c\bar{c}$ quark pair production at the matrix element level. In addition, a separate sample containing W+c+jets events is produced. The overlap between the W+light jets and $W + b\bar{b}$ samples is approximately 4%. An overlap removal procedure is applied to avoid double counting. For the small background of single-top

*The 'MLM' matching scheme of the ALPGEN generator is used to remove overlaps between the n and $n+1$ parton samples with parameters `RCLUS`=0.7 and `ETCLUS`=20GeV.

production MC@NLO is used, invoking the 'diagram removal scheme' [86] to remove overlaps between the single-top and the $t\bar{t}$ final states. Diboson WW+jets, WZ+jets and ZZ+jets events were generated with HERWIG. Unless otherwise noted, all events are hadronised with HERWIG using JIMMY for the underlying event model. Details on generator and underlying event tunes used for these samples are given in [87].

The LHC instantaneous luminosity varied by several orders of magnitude during this data-taking period, reaching a peak of about 1.3×10^{33} cm^{-2}s^{-1}. At this luminosity an average of about 8 extra pp interactions are superimposed on each collision event. Pile-up corresponding on average to 6 extra events is added to the MC simulation. A small pile-up uncertainty is considered to cover the remaining mismatch in the observed number of reconstructed primary vertices between data and MC.

7.2 Object Selection

The reconstruction of $t\bar{t}$ events makes use of electrons, muons, jets, and of missing transverse energy, which is an indicator of undetected neutrinos. The events selected for analysis were triggered by a single-lepton trigger. The electron trigger requires a level-1 electromagnetic cluster with transverse energy $E_{\mathrm{T}} > 14$ GeV. A more refined electromagnetic cluster selection is required in the level-2 trigger, and a match between the selected calorimeter electromagnetic cluster and an ID track is required in the event filter. The full trigger chain is `L1_EM14`, `L2_e20_medium` and `EF_e20_medium`. The muon trigger starts by requiring a $p_{\mathrm{T}} > 10$ GeV track in the muon trigger chambers at level-1, matched to a muon of $p_{\mathrm{T}} > 18$ GeV reconstructed in the precision chambers and combined with an ID track. The full trigger chain is `L1_MU10`, `L2_mu18` and `EF_mu18`. The following criteria are used to define the selected objects in the events:

- **Electrons** are defined as electromagnetic clusters consistent with the energy deposition of an electron in the calorimeters and with an associated well-measured track. Candidates are selected in the `ElectronAODCollection` collection, obtained with the calorimeter-seeded reconstruction algorithm `(author == 1 || 3)`, passing the `ElectronTight` requirements. Electrons are required to satisfy $E_{\mathrm{T}} > 25$ GeV ($E_T = E_{\mathrm{cluster}}/\cosh(\eta_{\mathrm{track}})$) and $|\eta_{\mathrm{cluster}}| < 2.47$, where η_{cluster} is the pseudorapidity of the calorimeter cluster associated with the candidate. Candidates in the barrel to endcap calorimeter transition region at $1.37 < |\eta_{\mathrm{cluster}}| < 1.52$

were excluded. Also, in order to suppress the background from photon conversions, the track is required to have an associated hit in the innermost pixel layer. Finally, the electron candidates are required to be "isolated": the transverse energy deposited in the calorimeter towers in a cone* of size $\Delta R = 0.2$ around the electron position is corrected to take into account the leakage of the electron energy. The remaining E_{T} is required to be less than 4 GeV.

- **Muon** candidates are reconstructed from track segments in the different layers of the muon chambers. These segments are combined starting from the outermost layer, with a procedure that takes material effects into account, and matched with tracks found in the inner detector. Candidates are selected in the `MuidMuonCollection` collection, fulfilling the `Tight` and `Combined` requirements `(author==MuonParameters::MuidCo)`. The final candidates are refitted using the complete track information from both detector systems, and required to satisfy $p_{\mathrm{T}} > 20$ GeV and $|\eta| < 2.5$. Additional hit requirements are:

  1. Number of hits in the B layer > 0 if the track does not cross a dead region.
  2. Number of pixel hits plus number of crossed dead pixel sensors > 1.
  3. Number of SCT hits plus number of crossed dead SCT sensors ≤ 6.
  4. Number of pixel holes plus number of SCT holes < 2.
  5. Sum of TRT hits and TRT outliers > 5 and TRT outliers/(TRT hits + TRT outliers) < 0.9 for $|\eta| < 0.9$.
  6. TRT outliers/(TRT hits + TRT outliers) < 0.9 if TRT hits > 5 for $|\eta| \leq 0.9$.

  Finally, muon candidates are required to be isolated by requiring the calorimeter energy in a cone of $\Delta R = 0.3$ to be less than 4 GeV, and the analogous sum of track transverse momenta in a cone of $\Delta R = 0.3$ to be less than 4 GeV. Additionally, muons are required to have a distance ΔR greater than 0.4 from any jet with $p_{\mathrm{T}} > 20$ GeV, further suppressing muons from heavy flavour decays inside jets.

*$\Delta R = \sqrt{(\Delta\eta)^2 + (\Delta\phi)^2}$

- **Jets** are reconstructed with the anti-k_t algorithm [69] ($\Delta R = 0.4$) from topological clusters [88] of energy deposits in the calorimeters, calibrated at the electromagnetic scale appropriate for the energy deposited by electrons or photons. These jets are then calibrated to the hadronic energy scale using a correction factor which depends upon the p_{T} and η obtained from simulation. If the closest object to a selected electron is a jet with a separation $\Delta R < 0.2$ the jet is removed to avoid double-counting of electrons as jets. The jet energy scale (JES) uncertainty is found to vary from 2 to 7% as a function of jet p_T and η. The jet energy resolution (JER) and jet finding efficiency measured in data are applied to all MC samples.

  Jets are considered b-tagged if the JetFitterCOMBNN b-tagging algorithm returns a "weight" value above the threshold of -1.25, which corresponds to about 80% tagging efficiency and 25 light-jet rejection factor for simulated $\mathrm{t\bar{t}}$ events.

- The **missing transverse energy** (`MET_RefFinal_em_tight`) is constructed from the vector sum of calorimeter energy deposits, resolved into the transverse plane. Cells not associated to muons, electrons with $p_{\mathrm{T}} > 10$ GeV, jets and soft jets are included at the EM scale. The electrons, muons and jets used in the missing transverse energy ($E_{\mathrm{T}}^{\mathrm{miss}}$) calculation are used consistently with the definitions and uncertainties stated above.

7.3 Monte Carlo Correction Factors

Since discrepancies between data and MC may appear, scale factor (SF) and efficiencies have been measured to achieve a better agreement among them. An extensive explanation can be found in Ref. [89]. The measurements use samples of $Z \to ll$ and $W \to l\nu$ decays, extracted from the same datasets used for the top-quark analyses. The ratio of the efficiencies obtained in data and MC samples is used to measure the SF to correct the $t\bar{t}$ MC acceptance. These SF account for mis-modellings of the detector and differences of reconstruction and identification performance in MC with respect to those in data. The efficiency of the electron and muon reconstruction, triggers, electron identification and isolation requirements are measured within the egamma and muon combined performance groups [90][91]. The muon channel deserves a special mention, since the HLT has an inefficiency due to a configuration bug.

The measurements of the electron and muon energy scale and resolution have been performed in a kinematic range comparable to that in top events. The energy scale is determined by constraining the peak position of the di-lepton invariant mass distribution in $Z \to ll$ events and parametrizing it as a function of the lepton η. This is done using data for the electron sample and MC simulated events for the muon sample. Although the energy resolution is well known in ATLAS, an additional constant term is needed in MC to correctly reproduce the line shape of the Z peak measured in data.

The analogous SF for b-jets are provided by the b-tagging working group, defined as the ratio of heavy-flavor efficiencies in data ($\epsilon^{Data}_{Flavor}(p_{\mathrm{T}}, \eta)$) over MC ($\epsilon^{MC}_{Flavor}(p_{\mathrm{T}}, \eta)$) for different jet flavors as a function of jet p_{T} and η. For each jet in the analysis, a weight is computed to correct the jet tagging rate in MC to that in data. If the jet is tagged the jet weight is defined as the SF:

$$w_{jet} = SF_{Flavor}(p_{\mathrm{T}}, \eta) = \frac{\epsilon^{Data}_{Flavor}(p_{\mathrm{T}}, \eta)}{\epsilon^{MC}_{Flavor}(p_{\mathrm{T}}, \eta)} \tag{7.2}$$

whereas if the jet is not tagged the weight is:

$$w_{jet} = \frac{1 - \epsilon^{Data}_{Flavor}(p_{\mathrm{T}}, \eta)}{1 - \epsilon^{MC}_{Flavor}(p_{\mathrm{T}}, \eta)} = \frac{1 - SF_{Flavor}(p_{\mathrm{T}}, \eta)\epsilon^{MC}_{Flavor}(p_{\mathrm{T}}, \eta)}{1 - \epsilon^{MC}_{Flavor}(p_{\mathrm{T}}, \eta)} \tag{7.3}$$

The latter form in Eq. 7.3 is preferred since dependencies of $\epsilon^{MC}_{Flavor}(p_{\mathrm{T}}, \eta)$ on event topology are expected to be small, and $SF_{Flavor}(p_{\mathrm{T}}, \eta)$ can be measured in di-jet control samples [92].

7.4 Event Selection

Events that pass the trigger selection are required to contain one and only one reconstructed lepton with $E_{\mathrm{T}} > 25$ ($p_{\mathrm{T}} > 20$ GeV) in the electron (muon) channel, matching the corresponding high-level trigger object in the electron case. Events tagged as electron-muon overlap are removed from the sample. Selected events are required to have at least one offline-reconstructed primary vertex with at least five tracks, and events are discarded if any jet with $p_{\mathrm{T}} > 20$ GeV is identified as out-of-time activity or calorimeter noise. The $E^{\mathrm{miss}}_{\mathrm{T}}$ is required to be larger than 35 (20) GeV in the electron (muon) channel and the transverse leptonic W mass is required to be larger than 25 GeV (60 GeV - $E^{\mathrm{miss}}_{\mathrm{T}}$) in the electron (muon) channel. The latter requirement is referred to as the triangular cut. The requirements are stronger in the electron channel to suppress the larger multi-jet background. Finally, events are required to have three or more jets with $p_{\mathrm{T}} > 25$ GeV and $|\eta| < 2.5$. Subsamples of the above samples are defined with the additional requirements that none, one or at least two of the jets with $p_{\mathrm{T}} > 25$ GeV are tagged as b-jet. The selected events are then classified by the number of jets and b-tagged jets per event fulfilling these requirements. The division into different number of jets will help reducing uncertainties related to the jet energy scale, whereas the separation into different b-tagged jets is necessary to measure R_b. Tabs. 7.1 and 7.2 show the number of selected events in the different jet multiplicity bins used in the analysis. For an inclusive selection see Appendix A. The signal and background estimates are obtained from MC simulation samples except the QCD multi-jet background estimate, which is obtained from data as described in the next section. The $\mathrm{t\bar{t}}$ signal includes the lepton plus jets and the dilepton final states.

Table 7.1: Selected events in the electron channel split up according to jet and b-tag multiplicity. Scale factors obtained from the asymmetry analysis have been applied to the W+jets samples. The quoted uncertainties are statistical.

0 b-tag	3 jets	4 jets	$\geq$ 5 jets
$t\bar{t}$	278.7 ± 3.1	168.3± 2.4	92.9 ±1.8
QCD multi-jet	1515.9 ± 30.5	429.6 ± 15.6	136.8 ±8.9
W+jets	11791.6 ± 120.2	2962 ± 57	1148 ± 28
Z+jets	1294.2 ± 23.5	391.6 ± 11.4	154.8 ±7.9
Single top	87.5 ± 3.4	27.6 ± 1.0	7.8 ±0.9
Diboson	188.1 ± 6.0	42.6 ± 2.4	7.8 ±0.9
Predicted	15156.0 ± 126.5	3843.0 ±47.7	1087.8 ±25.4
Observed	15322	3628	1214
1 b-tag	3 jets	4 jets	$\geq$ 5 jets
$t\bar{t}$	1237.0 ± 6.5	939.9 ± 5.7	594.5 ±4.6
QCD multi-jet	695.3 ± 27.7	263.1 ± 17.5	107.8 ±11.9
W+jets	3320.9 ± 56.3	1071.6 ± 17.5	361.2 ±14.7
Z+jets	227.6 ± 10.1	115.1 ± 3.64	60.3 ±5.1
Sing. top	323.5 ± 6.5	106.2 ± 2.5	38.0 ±2.0
Diboson	64.3 ± 3.5	17.9 ± 1.0	4.0 ±0.8
Predicted	5868.5 ±64.3	2513.8 ±25.8	1165.6 ±20.3
Observed	5632	2349	1212
$\geq$ 2 b-tag	3 jets	4 jets	$\geq$ 5 jets
$t\bar{t}$	1349.2 ± 6.8	1644.6 ± 7.6	1410.3 ±7.1
QCD multi-jet	61.9 ± 13.1	32.7 ± 12.6	0 ±10.6
W+jets	453.1 ± 19.5	227.0 ± 8.6	122.8 ±9.1
Z+jets	14.7 ± 2.6	14.4 ± 0.7	13.3 ±2.4
Sing. top	163.6 ± 4.7	91.5 ± 2.5	47.9 ±2.3
Diboson	10.9 ± 1.2	4.3 ± 0.4	1.2 ±0.5
Predicted	2053.3 ±25.1	2014.5 ±17.2	1580.0 ±16.0
Observed	2012	1969	1716

Table 7.2: Selected events in the muon channel split up according to jet and b-tag multiplicity. Scale factors obtained from the asymmetry analysis have been applied to the W+jets samples. The quoted uncertainties are statistical.

0 b-tag	3 jets	4 jets	$\geq$ 5 jets
$t\bar{t}$	431.7 ± 3.5	266.6 ± 2.8	150.6 ±2.1
QCD multi-jet	2730.7 ± 42.8	630.5± 19.6	182.1 ±10.2
W+jets	25244.0 ± 189.6	5315.2 ± 79.6	1507.7 ±35.1
Z+jets	2051.9 ± 26.4	562.1 ± 13.5	172.8 ±7.2
Single top	145.6 ± 3.9	44.0 ± 1.9	12.5 ±1.0
Diboson	353.5 ± 7.4	80.1 ± 3.5	17.7 ±1.6
Predicted	30957.4 ±196.4	6898.4 ±83.2	2043.4 ±37.4
Observed	31060	6822	1908
1 b-tag	3 jets	4 jets	$\geq$ 5 jets
$t\bar{t}$	1936.9 ± 7.3	1556.0 ± 6.5	989.1 ±5.3
QCD multi-jet	1331.3 ± 26.0	411.5 ± 14.1	156.8 ±8.6
W+jets	6872.4 ± 82.6	1931.5 ± 38.4	728.9 ±21.2
Z+jets	457.6 ± 12.9	174.9 ± 7.8	69.9 ±4.7
Sing. top	535.1 ± 7.4	166.9 ± 3.9	56.3 ±2.2
Diboson	123.0 ± 4.4	32.3 ± 2.3	8.8 ±1.2
Predicted	11256.4 ±88.3	4273.1 ±42.4	2009.8 ±24.1
Observed	11051	4332	2123
$\geq$ 2 b-tag	3 jets	4 jets	$\geq$ 5 jets
$t\bar{t}$	2136.7 ± 7.6	2753.2 ± 8.7	2394.7 ±8.3
QCD multi-jet	221.8 ± 10.8	100.1 ± 7.5	74.9 ±6.4
W+jets	943.5 ± 33.1	429.1 ± 20.3	233.9 ±14.9
Z+jets	38.9 ± 3.7	21.8± 2.77	18.5 ±2.4
Sing. top	295.1± 5.7	149.1 ± 3.8	77.5 ±2.5
Diboson	22.4 ± 1.7	7.0 ± 0.9	2.4 ±0.6
Predicted	3658.4 ±36.3	3460.3 ±23.8	2802.0 ±18.5
Observed	3656	3363	2899

Figure 7.1 shows the jet multiplicity in the electron and muon channels, respectively, for a data sample where all the selection criteria have been applied. Fig. 7.2 shows the tagged jet multiplicity for events fulfilling all the selection criteria and having at least four jets. Appendix B includes the reconstructed leptonic transverse W mass, the missing transverse energy, the lepton p_T and η, the leading and second leading jet p_T,

and the number of primary vertices distributions for each jet and b-tag multiplicity bin. Finally, Figs. 7.3 and 7.4 show the three-jet invariant mass m_{jjj} (defined in Sec. 7.6) distributions in the electron and muon channel, for the 3-, 4-, and $\geq$ 5- jet and 0-, 1- and $\geq$ 2 b-tagged samples. All figures show the selected data as points overlaid on the SM expectation (histograms). As mentioned previously, the expectation for both signal and background is obtained from MC simulation, except the QCD multi-jet background estimate, which is obtained from data. One can observe that data agree nicely with the expectation in all these distributions.

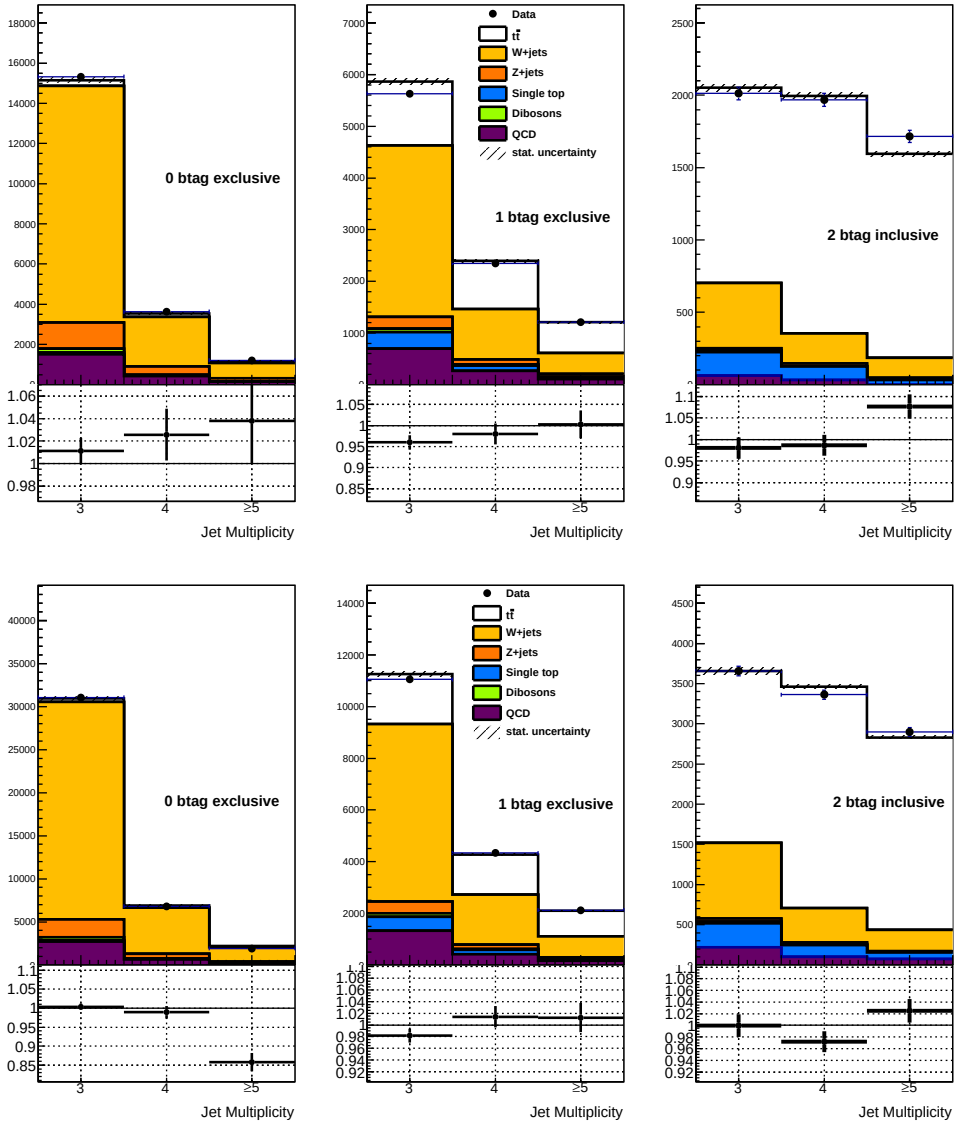

Figure 7.1: Jet multiplicity in the electron (top) and muon (bottom) channels for the events passing all the selection criteria. The data (dots with error bars) are compared to the expectation. Scale factors obtained from the asymmetry analysis have been applied to the W+jets samples.

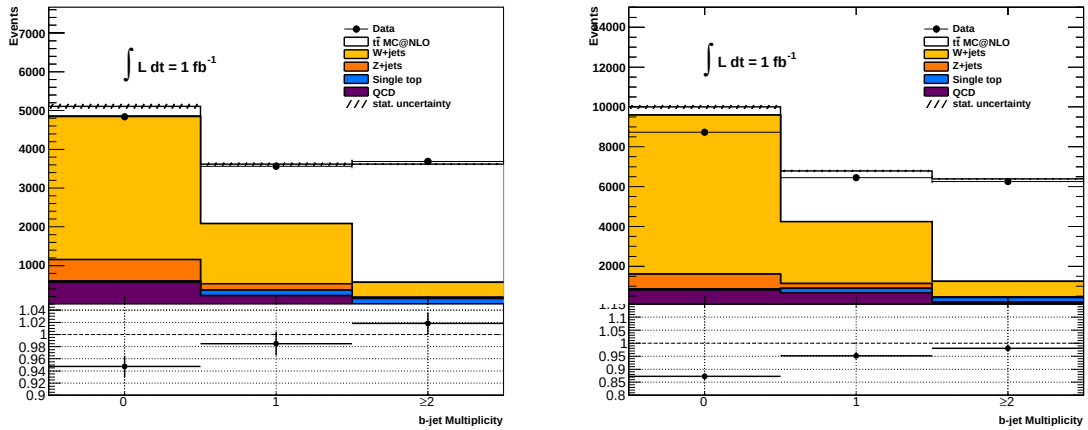

Figure 7.2: Tagged jet multiplicity in the electron (left) and muon (right) channels for the events passing all the selection criteria and having at least four jets. The data (dots with error bars) are compared to the expectation. Scale factors obtained from the asymmetry analysis have been applied to the W+jets samples.

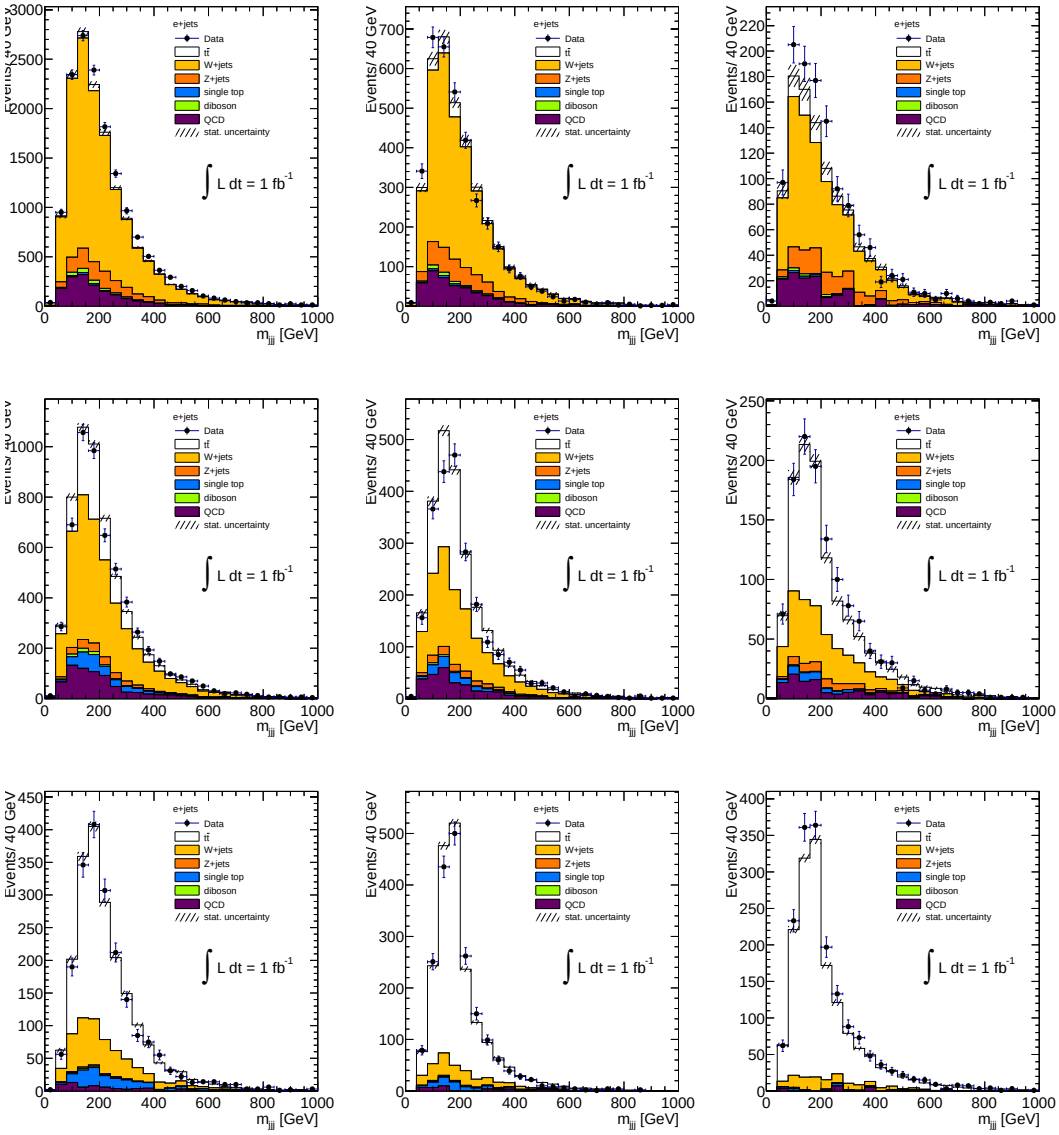

Figure 7.3: Three-jet invariant mass in the 0- (top), 1- (medium) and $\geq$ 2- (bottom) b-jet multiplicity bins in the electron channel. The data (dots with error bars) are compared to the expectation. Scale factors obtained from the asymmetry analysis have been applied to the W+jets samples.

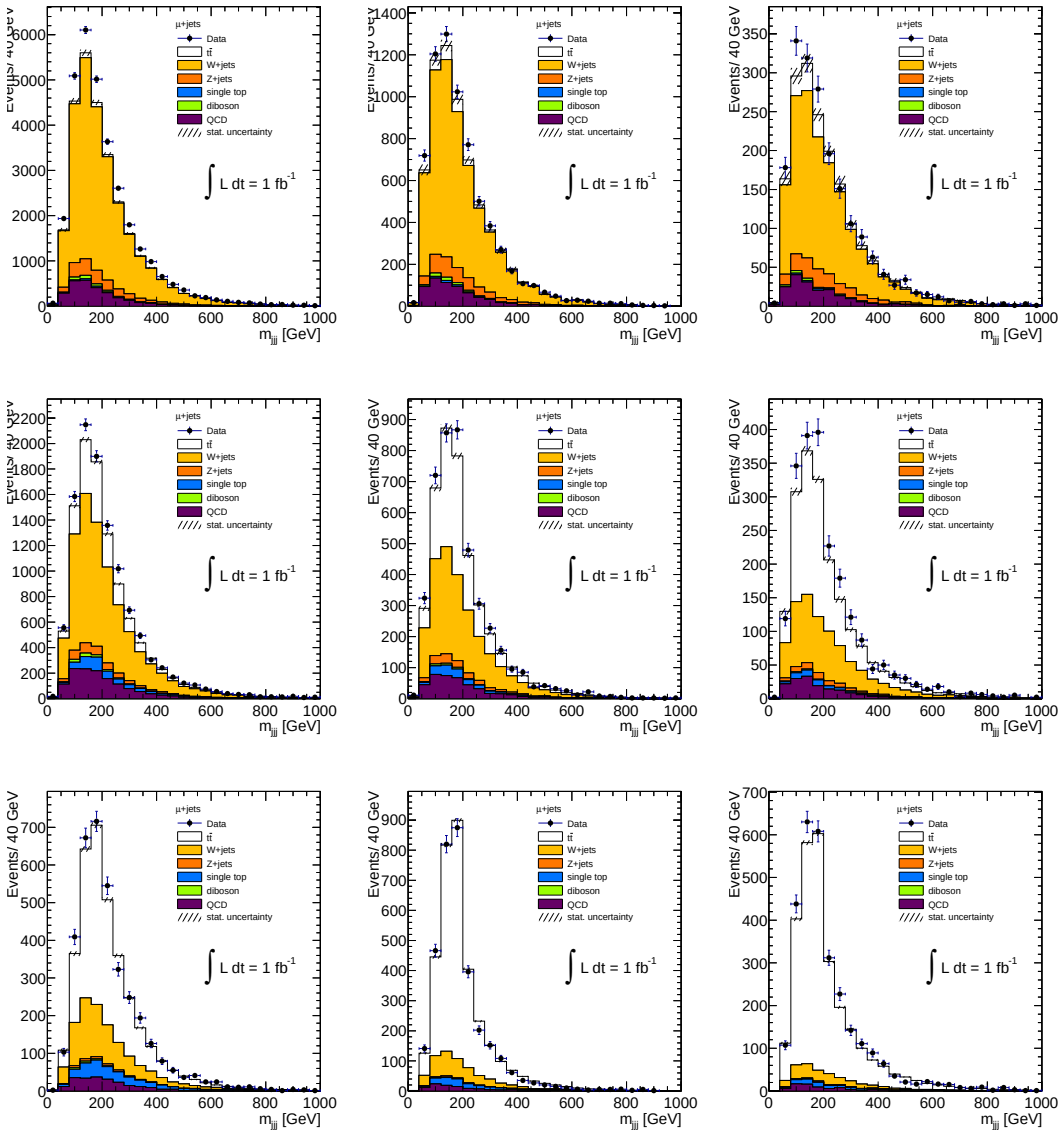

3-jet 4-jet $\geq$ 5-jet

Figure 7.4: Three-jet invariant mass in the 0- (top), 1- (medium) and $\geq$ 2- (bottom) b-jet multiplicity bins in the muon channel. The data (dots with error bars) are compared to the expectation. Scale factors obtained from the asymmetry analysis have been applied to the W+jets samples.

7.5 Background Evaluation

The main backgrounds to $t\bar{t}$ signal events in the single lepton plus jets channel arise from W-boson production in association with jets (in which the W decays leptonically) and from QCD multi-jet production. The latter background can arise from various sources: (i) jets can be mis-reconstructed as electrons if a relatively high fraction of their energy is in the electromagnetic calorimeter (ii) real electrons or muons can be produced in the decays of heavy flavour hadrons inside jets (iii) photons inside jets can undergo conversions to electrons. Relatively smaller backgrounds also arise from Z+jets, diboson and single top production.

The small backgrounds are estimated from MC simulation (see the description of the different MC samples in Sec. 7.1) normalized to the latest theoretical predictions. The W+jets background shape is estimated from MC simulation. Data driven cross-checks were performed and data was found to agree with the MC predictions within the uncertainties [93]. Since the normalization of the W+jets background is difficult to predict in the high jet-multiplicity bins, we use the data/MC scale factors obtained in the W+jets asymmetry analysis [94]. These scale factors are 0.833 in the 3-jet bin, 0.879 in the 4-jet bin and 0.866 in the 5-jet bin. A global scale factor, common to all jet bins, will be obtained from a fit to the three-jet invariant mass of candidate hadronic top decays (see next Section).

The multi-jet background is very difficult to predict from MC simulation so a data driven approach to measure it is used instead, called the matrix method (MM). The leptons used in our event selection have tight isolation requirements, obtained by limiting the amount of energy surrounding the lepton. In addition to these 'tight' leptons, a second sample of 'loose' leptons is defined by removing the isolation criteria for the muons and lessening the `ElectronTight` requirement to be `ElectronMedium` for the electrons. Finally, the isolation requirement is loosened: the leakage-corrected and pileup-corrected `EtCone20` is required to be < 6 GeV instead of < 3.5 GeV. Additionally, `MET_RefFinal_em_medium` is used in the loose selection instead of `MET_RefFinal_em_tight`.

Any lepton sample is composed of 'prompt' (real) leptons (from W or Z decays) and 'non-prompt' (fake) (*e.g.* from heavy-flavour hadrons decays or jets misidentified as electrons). We assume that the tight sample is the final selection used in the analysis. Both selections, loose and tight, include contributions from events with real and

misidentified leptons:

$$\begin{aligned} N^{\text{loose}} &= N^{\text{loose}}_{\text{real}} + N^{\text{loose}}_{\text{fake}}, \\ N^{\text{tight}} &= \epsilon_{\text{real}} N^{\text{loose}}_{\text{real}} + \epsilon_{\text{fake}} N^{\text{loose}}_{\text{fake}}, \end{aligned} \tag{7.4}$$

where $\epsilon_{\text{real}}(\epsilon_{\text{fake}})$ represents the probability for a real (fake) lepton that satisfies the loose criteria, to also satisfy the tight ones. From previous equations, one can write

$$N^{\text{tight}}_{\text{real}} = \frac{\epsilon_{\text{real}}}{\epsilon_{\text{real}} - \epsilon_{\text{fake}}}(N^{\text{tight}} - \epsilon_{\text{fake}} N^{\text{loose}}) \tag{7.5}$$

$$N^{\text{tight}}_{\text{fake}} = \frac{\epsilon_{\text{fake}}}{\epsilon_{\text{real}} - \epsilon_{\text{fake}}}(\epsilon_{\text{real}} N^{\text{loose}} - N^{\text{tight}}). \tag{7.6}$$

This set of equations allows us to estimate the number of events in the tight sample. Defining the 'loose-not-tight' events as $N^{\text{loose-not-tight}} = N^{\text{loose}} - N^{\text{tight}}$ one can rewrite Eq. 7.6 as

$$N^{\text{tight}}_{\text{fake}} = \frac{\epsilon_{\text{real}} \cdot \epsilon_{\text{fake}}}{\epsilon_{\text{real}} - \epsilon_{\text{fake}}} N^{\text{loose-not-tight}} + \frac{\epsilon_{\text{fake}}(\epsilon_{\text{real}} - 1)}{\epsilon_{\text{real}} - \epsilon_{\text{fake}}} N^{\text{tight}}. \tag{7.7}$$

And from here an event-by-event weighting of the complete data sample can be applied. For events that fulfill the loose but fail the tight requirements the weight is:

$$\omega_{\text{loose-not-tight}} = \frac{\epsilon_{\text{real}} \cdot \epsilon_{\text{fake}}}{\epsilon_{\text{real}} - \epsilon_{\text{fake}}}, \tag{7.8}$$

and for those that fulfill the tight requirement the weight is:

$$\omega_{\text{tight}} = \frac{\epsilon_{\text{fake}}(\epsilon_{\text{real}} - 1)}{\epsilon_{\text{real}} - \epsilon_{\text{fake}}}. \tag{7.9}$$

ϵ_{real} is measured from data using samples dominated by leptonically decaying Z-bosons. By defining control samples dominated by QCD multi-jet events, one can measure the efficiency ϵ_{fake} for a non-isolated lepton to pass the tight isolation cuts. Two different control regions are defined: $5\text{GeV} < E_{\text{T}}^{\text{miss}} < 20\text{GeV}$ for electrons and $5\text{GeV} < E_{\text{T}}^{\text{miss}} < 15\text{GeV}$ for muons. Any significant dependence of the efficiencies on the kinematics or on the topology must be parametrized. In the case of the muons,

these dependencies are on the muon η, leading jet p_{T} and minimum $\Delta R(\mu, j)$. The contamination of the QCD control regions by 'prompt' leptons from W, Z and $\mathrm{t\bar{t}}$ events is determined by an iterative method which combines MC simulation and data driven estimates, as shown in Eq. 7.10 and more extensively in Ref. [95].

$$\begin{aligned} N_{corr}^{\text{tight}} &= N^{\text{tight}} - N_{W+jets,MC}^{\text{tight}} - N_{Z+jets,MC}^{\text{tight}} - N_{\mathrm{t\bar{t}},MC}^{\text{tight}} \\ N_{corr}^{\text{loose}} &= N^{\text{loose}} - N_{W+jets,MC}^{\text{loose}} - N_{Z+jets,MC}^{\text{loose}} - N_{\mathrm{t\bar{t}},MC}^{\text{loose}} \end{aligned} \tag{7.10}$$

The final results are the QCD background predictions as a function of the lepton η, ϕ, p_{T} and the different jet multiplicity bins. The systematic uncertainties related to the MM procedure include statistical error on the determination of ϵ_{real} and ϵ_{fake}, the different control regions used to determine ϵ_{fake}, and the different parametrizations. A conservative 50% uncertainty correlated among all jet bins, is assigned to this estimate in the untagged bins. An additional uncorrelated 50% is uncertainty added to the b-tagged bins [95].

7.6 Likelihood Fit

To extract $\sigma_{t\bar{t}}$ and R_b we perform a binned likelihood fit (Eq. 7.12) to the three-jet invariant mass m_{jjj} distribution of candidate hadronic top decays, defined as the combination of three jets having the highest vector sum p_T, in the selected data sample ($\mathcal{D}_{data}$) to a weighted sum of templates corresponding to the three $\mathrm{t\bar{t}}$ samples, ($\mathcal{D}_{t\bar{t}}^{bb}$, $\mathcal{D}_{t\bar{t}}^{bq}$ and $\mathcal{D}_{t\bar{t}}^{qq}$, where q represent d- or s-type quarks, see Sec. 7.7), W+jets ($\mathcal{D}_W$), QCD ($\mathcal{D}_{QCD}$), and the rest of physics backgrounds, single top, Z+jets, and diboson ($\mathcal{D}_{other}$):

$$\begin{aligned} \mathcal{D}_{data} = k_{t\bar{t}} \times \left(R_b^2\, \mathcal{D}_{t\bar{t}}^{bb} + 2R_b(1-R_b)\, \mathcal{D}_{t\bar{t}}^{bq} + (1-R_b)^2\, \mathcal{D}_{t\bar{t}}^{qq} \right) + \\ k_{W+jets} \times \mathcal{D}_W + k_{QCD} \times \mathcal{D}_{QCD} + k_{other} \times \mathcal{D}_{other}. \end{aligned} \tag{7.11}$$

The factor $k_{\mathrm{t\bar{t}}}$ multiplies the corresponding nominal cross-section of the $\mathrm{t\bar{t}}$ signal and a scaling factor of one would correspond to the nominal SM prediction 164.6 pb [80]. The other k's factors provide the different amount of backgrounds in the selected data sample. The template shape describing $\mathrm{t\bar{t}}$ events is taken from simulation, as well as the shapes describing W+jets and minor backgrounds like single top, Z+jets and di-boson processes. The template shape for QCD multi-jet background has been derived

from data, as explained in the previous Section, and is then not affected by physics modelling and JES uncertainties.

To avoid statistical fluctuations in the templates where b-tagging is required and to improve the stability of the fit and the determination of the systematic uncertainties, we apply a per-jet tagging probability to the untagged templates to obtain the tagged templates shape. Their overall normalization, though, is obtained from the yields obtained after the full event selection, *i.e.* after applying b-tagging, is applied (see Appendix C).

We perform a simultaneous fit of $k_{t\bar{t}}$, k_{W+jets} and R_b. The factor k_{QCD} is set to one, such as to reproduce the number of multi-jet events predicted by the data-driven method (Sec. 7.5) in each channel. The coefficient k_{other} is set to one, corresponding to the SM expectation. The uncertainties on k_{QCD} and k_{other} factors are propagated to the final result of the fit and the corresponding systematics evaluated.

The high jet-multiplicity bins in the b-tagged samples are the ones where we expect to collect most of the $\mathrm{t\bar{t}}$ signal, as seen in Tabs. 7.1 and 7.2. Nevertheless, the sensitivity of the fit to the $\mathrm{t\bar{t}}$ cross-section depends also on how well the W+jets normalization is fixed by the fit. As the W background level in the $\geq$4-jet sample is relatively low, it is not stringently constrained by the fit of the $\geq$4-jet tagged sample only. Further constraint is obtained by fitting simultaneously the three-jet exclusive sample that contains a larger fraction of W+jets events and still a sizable amount of $\mathrm{t\bar{t}}$ events. The inclusion of the three-jet exclusive sample in the fit adds about 60% signal. Thus, to provide the maximum sensitivity, we perform a combined fit of nine samples for the electron and nine samples for the muon channels: 3-jet, 4-jet and $\geq$5-jet, and zero-tag, 1-tag and $\geq$2-tag. The fit method takes into account the full correlation of systematic uncertainties from both normalization and shape across processes as well as channels.

In this analysis, most of the systematic variations due to external factors are not simply used to test the bias of the fit due to these factors, but enter directly in the minimization process of the likelihood as parameters of the fit [96]. Compared to a standard likelihood function, the "profile" likelihood function adds to the fitting function a set of nuisance parameters $\overrightarrow{\alpha}$, one for each systematic error:

$$-2\ln L(k_{t\bar{t}}, k_{W+jets}, R_b, \overrightarrow{\alpha}) \propto -2 \sum_{i=0}^{i=N_{bins}} n_i \ln(\mu_i) - \mu_i + \sum_{j=0}^{j=N_{syst}} \alpha_j^2 \qquad (7.12)$$

with:

$$\mu_i = \mu_i(k_{t\bar{t}}, k_{W+jets}, R_b \ , \overrightarrow{\alpha}) \tag{7.13}$$

The nuisance parameters control the size of the corresponding systematic uncertainties and their fitted value corresponds to the amount that better fits the data. Each nuisance parameter is assumed to be Gaussian-distributed around the nominal value of zero and with width one. A fitted value of ± 1 corresponds to the $\pm 1\sigma$ variation given in the input for the corresponding systematic uncertainty. The addition of nuisance parameters to the fit allows to effectively check and constrain in situ the systematic uncertainties using the data themselves. The uncertainty on the fitted values of the nuisance parameters defines the 68% confidence level (CL) range in which the variation of the systematic uncertainty is compatible with data. In the case that the given $\pm 1\sigma$ variation is significantly different from what data uncertainties allow, the uncertainty on the associate nuisance parameter is rescaled to the range covering the 68% CL. It should be noted that the nuisance parameters of the systematic uncertainties are all fitted together in the minimization process, taking into account the correlation among them in the variation of the yields and m_{jjj} shape. As a consequence, the contribution of the single systematic uncertainties to the fitted quantities becomes ill-defined. However, the total uncertainty is still well-defined because it is determined directly in the fitting process.

Extensive tests to check the goodness of the method have been performed. Among them the linearity of the measured quantities, $\sigma_{t\bar{t}}$ and R_b as a function of their true input values. Good linearity and no bias are observed for all fitted quantities, as can be seen in Figs. 7.5 and 7.6.

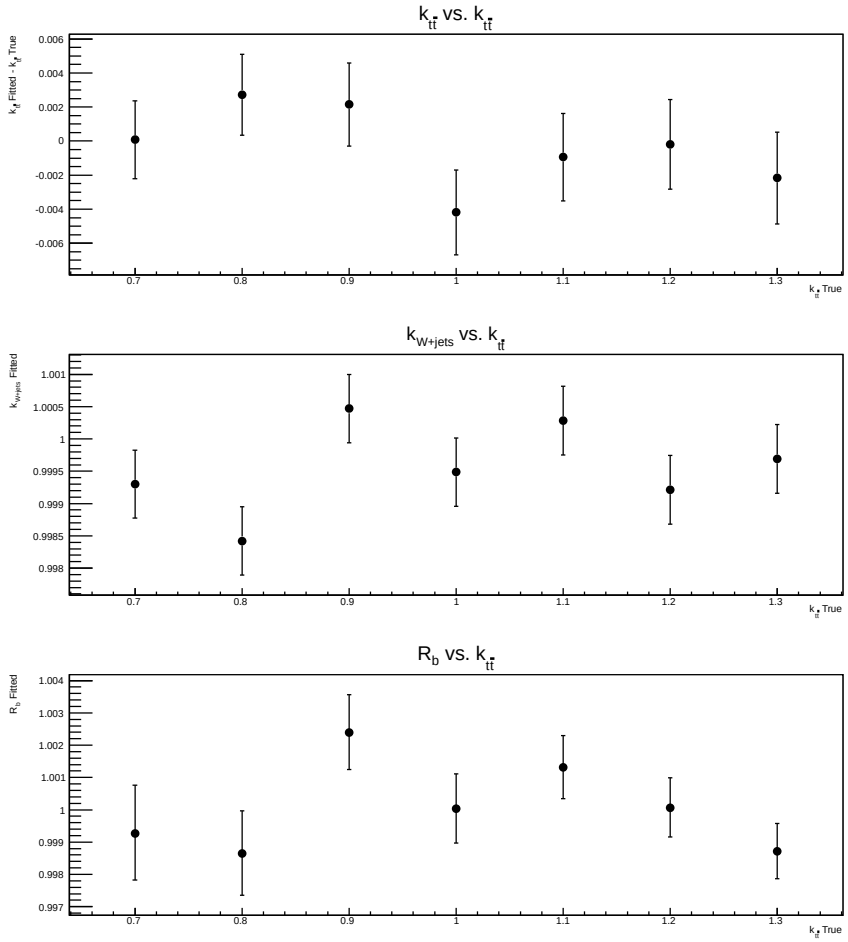

Figure 7.5: Measured $k_{t\bar{t}}$, k_{W+jets} and R_b as a function of the true input $k_{t\bar{t}}$. The top plot shows the difference between measured and true $k_{t\bar{t}}$ to better appreciate the errors.

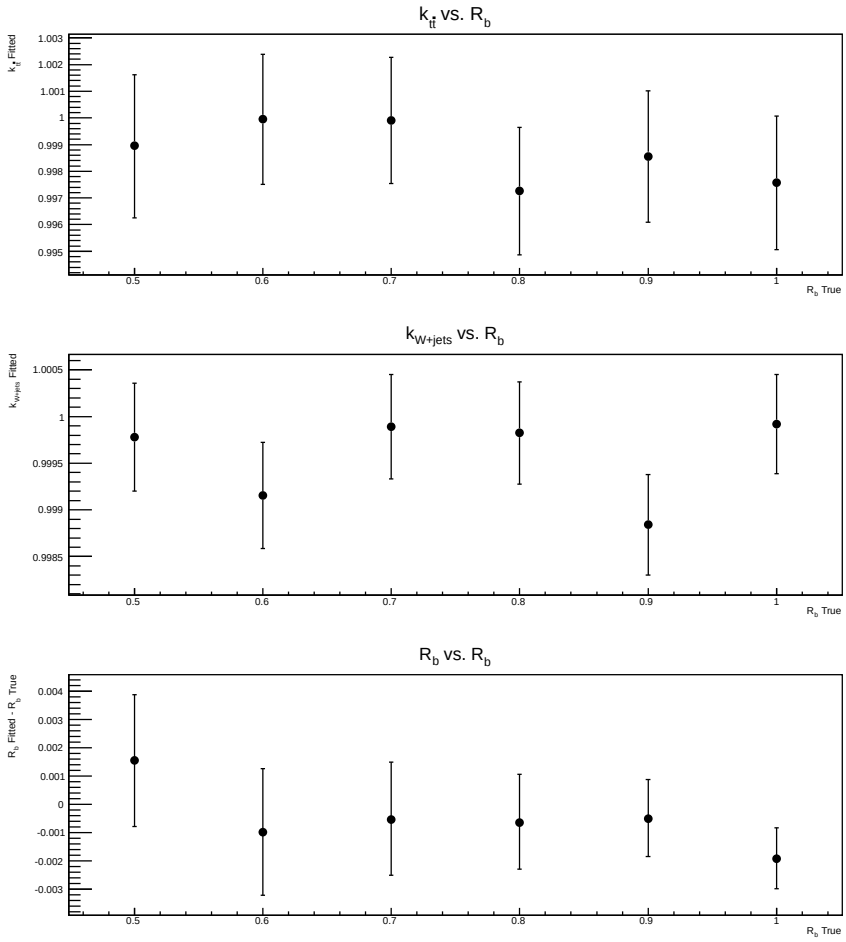

Figure 7.6: Measured $k_{\mathrm{t\bar{t}}}$, k_{W+jets} and R_b as a function of the true input R_b. The bottom plot shows the difference between measured and true R_b to better appreciate the errors.

7.7 How to Measure R_b

To measure R_b we need $t\bar{t}$ simulated samples with the top quark decaying not only to Wb, but also to Wtd and Wts. Since the MC@NLO generator only includes the Wb final state * we make use of the PROTOS generator. PROTOS stands for PRogram for TOp Simulations [84]. It is a LO generator for some new physics processes involving top quarks, but it also includes anomalous Wtq vertices. The ones relevant for this analysis are the ones within the SM, which can be written as Wtd, Wts and Wtb.

The samples we use include lepton plus jets and semileptonic final states. They use the CTEQ6 PDFs and $Q = m_t$ as factorization scale, and are interfaced with PYTHIA for fragmentation purposes. They are generated with 25% of Wtb-Wtb, 50% of Wtb-Wtq and 25% of Wtq-Wtq events, where q is a light down-type quark. In addition to the b-tagging multiplicity, that obviously depends on the final state, either Wtb-Wtb, Wtb-Wtq or Wtq-Wtq, we can expect a small increase on the average $E_{\mathrm{T}}^{\mathrm{miss}}$ of the event since only b-quarks can decay semileptonically [97]. Since the samples are very small (2K events each) they can not be used in the analysis directly. Furthermore, the LO approximation they use is not good enough. Nevertheless, they are very useful to check that the modification done on the MC@NLO MC to include $t \to Wq$ decays works properly. Finally, these samples allow us to evaluate the small differences in selection efficiency between the different event types ($WbWb$, $WbWq$ or $WqWq$), shown in Table 7.3.

Table 7.3: Selection efficiencies for the different PROTOS decays, compared to that of MC@NLO.

	3-jet ex	4-jet ex	5-jet in
PROTOS $WbWb$	0.0203±0.0006	0.0233±0.0007	0.0207±0.0006
PROTOS $WbWq$	0.0204±0.0005	0.0229±0.0005	0.0210±0.0004
PROTOS $WqWq$	0.0209±0.0006	0.0220±0.0007	0.0221±0.0007
MC@NLO $WbWb$	0.02927±0.00004	0.03017±0.00005	0.02508±0.00004

The differences in the reconstructed three-jet invariant mass for Wtb-Wtb, Wtb-Wtq and Wtq-Wtq events can be seen in Fig. 7.7.

* HERWIG crashes when generating the Wtd and Wts couplings.

The procedure to modify the MC@NLO generator so that it contains events with Wtq decays is straightforward, we just transform some b-jets of the event into light-jets depending on the final state. To "create" Wtq-Wtq events, we transform the two leading b-jets into light-jets. To "create" Wtb-Wtq events, we transform one of the two leading b-jets into a light jet randomly, so that if the first one is not transformed we transform the second. To transform a b-jet into a light-jet we apply a weight to it which depends on whether the jet is tagged or not. For tagged jets the weight is $w = SF_{\text{light}} \cdot \epsilon^{\text{MC}}_{\text{light}} \,/\, \epsilon^{\text{MC}}_{b}$, and for untagged jets the weight is $w = (1 - SF_{\text{light}} \cdot \epsilon^{\text{MC}}_{\text{light}}) \,/\, (1 - \epsilon^{\text{MC}}_{b})$, where SF_{light} is the light-jet data/MC scaling factor, which depends on η and p_{T} , and $\epsilon^{\text{MC}}_{\text{light}\,(b)}$ is the tagging efficiency for light (b) jets in MC [92]. (See Eq. 7.2 and 7.3)

To check this procedure, we apply this strategy to the PROTOS Wtb-Wtb sample itself. The "created" tagging efficiencies are compared with the true ones in Tab. 7.4. We see a good agreement between the true and "created" efficiencies in the Wtq-Wtq sample and small differences in the Wtb-Wtq sample.

The tagging efficiencies for the true and "created" PROTOS samples are compared in Fig. 7.8. Finally, Fig. 7.9 shows the tagging efficiencies for "created" MC@NLO samples.

Table 7.4: PROTOS b-tagging efficiencies. The central column shows the efficiencies of the true Wb-Wb, Wb-Wq and Wq-Wq samples, whereas the right column shows the efficiencies of the "created" Wb-Wq and Wq-Wq samples. We quote the efficiencies for the 0-tag exclusive, 1-tag exclusive and 2-tag inclusive samples normalized to the 0-tag inclusive tagging efficiency for every decay type. The table shows a $\mathrm{t\bar{t}}$ dominated sample, 4 jets exclusive in the muon channel.

Bin	True samples	"Created" samples
$Wb - Wb$		
0 tag ex / 0 tag in	$0.059/1.018 = 0.057$	–
1 tag ex / 0 tag in	$0.355/1.018 = 0.349$	–
2 tag in / 0 tag in	$0.603/1.018 = 0.592$	–
$Wb - Wq$		
0 tag ex / 0 tag in	$0.478/2.201 = 0.217$	$0.202/0.901 = 0.224$
1 tag ex / 0 tag in	$1.319/2.201 = 0.599$	$0.508/0.901 = 0.564$
2 tag in / 0 tag in	$0.396/2.201 = 0.180$	$0.191/0.901 = 0.212$
$Wq - Wq$		
0 tag ex / 0 tag in	$0.747/1.062 = 0.704$	$0.639/0.949 = 0.673$
1 tag ex / 0 tag in	$0.284/1.062 = 0.267$	$0.274/0.949 = 0.289$
2 tag in / 0 tag in	$0.030/1.062 = 0.028$	$0.036/0.949 = 0.038$

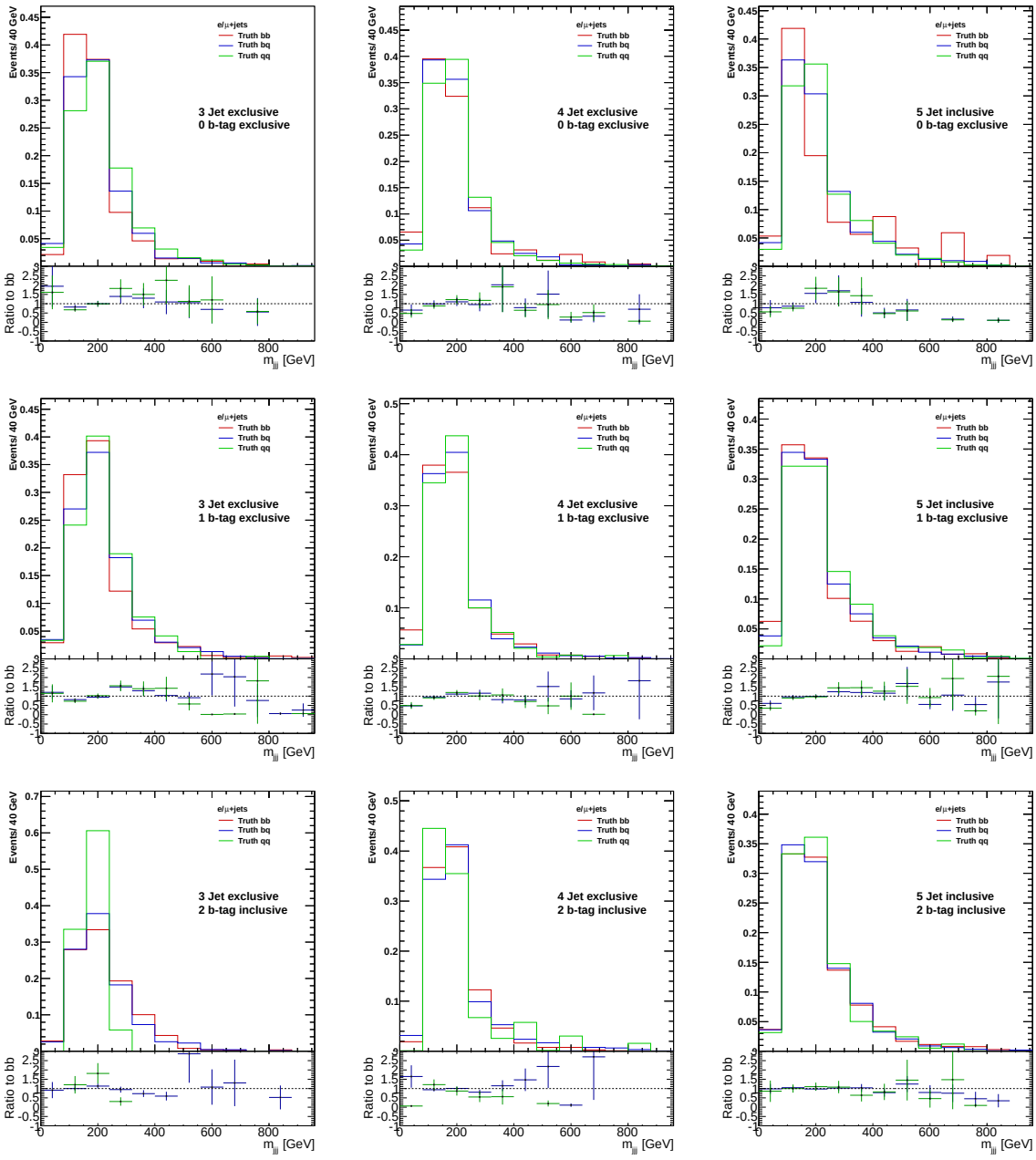

Figure 7.7: Reconstructed three-jet invariant mass for the different types of top decays. The red line corresponds to true bb decays, the blue line to true bq decays and the green line to true qq decays. Electron and muon samples are shown together to increase the statistics in the plots.

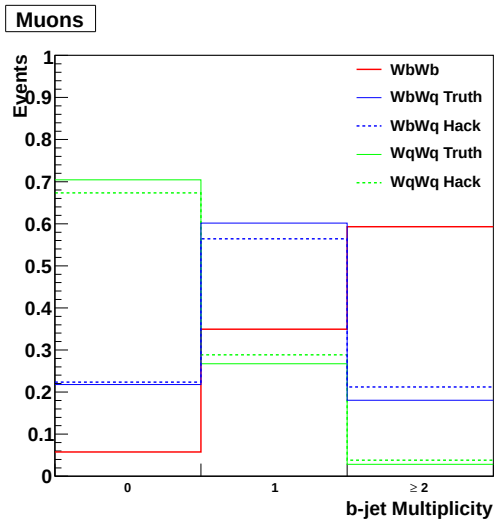

Figure 7.8: PROTOS b-jet multiplicity for true (solid lines) and "created" events (dashed lines). The red (blue, green) lines correspond to Wtb-Wtb (Wtb-Wtq and Wtq-Wtq) samples. The events are required to contain exactly four jets.

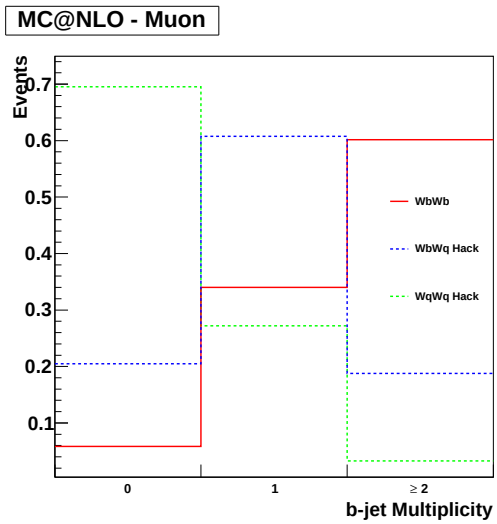

Figure 7.9: MC@NLO b-jet multiplicity for 'created" events. The red (blue, green) line corresponds to the Wtb-Wtb (Wtb-Wtq and Wtq-Wtq) sample. The events are required to contain exactly four jets.

7.8 Systematic Uncertainties

The following sources of systematic uncertainties have been included in the fit via nuisance parameters:

- **Lepton reconstruction, identification and trigger**: The reconstruction and identification of leptons as well as the efficiency of the trigger chain with which they are recorded differ between data and MC. Appropriate SF, derived using "tag-and-probe" techniques on $Z \to l^+l^-(l = e, \mu)$ data and MC are applied to the leptons in the MC simulation to correct for these effects. For each source of uncertainty, the quadratic sum of the statistical and the systematic uncertainty on the SFs is taken as systematic uncertainty. In the same manner, the muon momentum scale and resolution, as well as the electron energy calibration scale and resolution in MC, are smeared to match what is observed in data. The uncertainties associated with the smearing are taken into account to generate modified templates. For the muons, the ID and the MS smearings are varied separately. These uncertainties have been taken into account as normalization factors only accounting for 2.5 % for electrons and +1.0 % - 5.6 % for muons. This uncertainty appears in the following tables and figures under the labels `ElectronFactors` and `MuonFactors`.

- **JES**: The JES and its uncertainty have been derived combining information from test-beam and LHC collision data and from simulation, (see Sec 6.5.4). In the previous measurement with 35 pb^{-1} of data, the JES was conservatively determined with individual "up" and "down" templates. With the present larger sample (1035 pb^{-1}) a more sophisticated approach is desirable to improve the overall precision. To that end, the `JESUncertainty-00-03-04-01` package, which provides the individual sources of JES uncertainty as explained in Ref. [98], has been used. The contributions considered suitable for profiling are: Flavor-content, pile-up, close by jets, bJES and JES envelope.

  - Flavor content. The fragmentation differences between jets initiated by quarks or gluons lead to a flavor dependence in the JES [77].

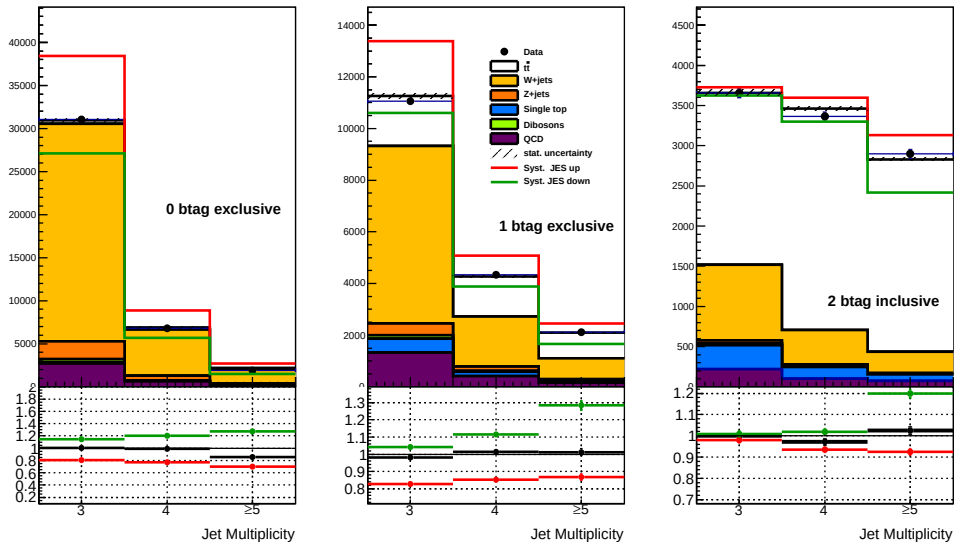

Figure 7.10: JES $\pm$ 1 σ variation in the nine channels used in the analysis for the muon channel.

- Pile-up. The energy of the jet can include energy that does not come from the hard scattering collision, but is instead produced in the multiple proton-proton interaction within the same bunch crossing [98].
- Close-by jets effects. The presence of any jets nearby could cause a difference in the jet response, resulting in an additional JES uncertainty [78].
- bJES. The estimated b-jet specific JES uncertainty depends on the p_{T} of the jets and decreases from 2.5% for jets in the 20-40 GeV range to 0.76% for jets with p_{T} above 600 GeV. The four-momenta of jets in MC matched to true b-quarks are scaled up and down according to their p_{T} to produce the up and down variated templates [99].
- Envelope. Includes the rest of the components (the calorimeter uncertainty from single particles propagation, the cluster noise thresholds from data, the Perugia 2010 tunes, the uncertainty due to the MC samples used (Alpgen + Herwig + Jimmy), the uncertainty due to the calibrarion of the endcap with respect to the central region, and the non-closure of numerical inversion constants) added in quadrature [98]. The variation of this uncertainty can be seen in Fig. 7.10.

The different components of the JES uncertainty appear in the following tables and figures under the labels `JES_FLAVOR`, `JES_PILEUP`, `JES_CLOSEBY`, `bJES` and `JES` respectively.

- **Jet energy resolution (JER)**: The JER observed in data is slightly worse than that in the MC simulation. The nominal samples are smeared according to the quadratic difference between the data uncertainty and the MC resolution as obtained from the `JERUncertaintyProvider` tool, which provides the expected fractional p_{T} resolution for a given jet as a function of its p_{T} and η. This uncertainty is one-sided by definition, as jets in MC cannot be under-smeared. Only an "up variation" template is computed and the corresponding "down variation" is obtained by applying a symmetrical variation to the nominal template. This uncertainty appears in the following tables and figures under the label `JER`.

- **Jet reconstruction efficiency (JRE)**: The JRE accounts for the difference between data and MC in the reconstruction efficiency of calorimeter jets with respect to tracks jets, measured with a tag-and-probe method in QCD dijet events. This difference amounts to approximately 0.4% (depending on the p_{T} of the jet) for low p_{T} jets ($p_{\mathrm{T}} < 35$ GeV) and remains within uncertainties for larger p_{T} jets. Thus, samples where 0.4% of the jets with p_{T} smaller than 35 GeV are randomly discarded are created and used to build modified references. Only an "up variation" template is computed and the corresponding "down variation" is obtained by applying a symmetrical variation to the nominal template. The effect of this uncertainty is negligible and has been removed.

- **Heavy- and light- flavour tagging**: This is one of the most important systematic uncertainties to take into account because of the high correlation between R_b and the b-tagging efficiency in the signal region. Different taggers (SV0, JetProb, JetFitterCombN) and working points (60%, 70% and 80% b-tagging efficiency) have been studied. This analysis uses the JetFitterCombNN tagger at the 80% efficiency working point. A single nuisance parameter is not enough to take into account all the dependencies, so we split the uncertainty into thirteen different nuisance factors, mainly those that change the shapes or the sample composition, as explained in Sec. 6.5.5 and more extensively in

Ref. [79]. The different components of the flavor tagging uncertainty appear in the following tables and figures under the labels `BCtag_bhadrondirection`, `BCtag_LighTemplateModelling`, `BCtag_JetEnergyScale`, `BCtag_BDecay`, `BCtag_Gluon_Splitting_C`, `BCtag_Gluon_Splitting_B`, `BCtag_Muon_Reweighting`, `BCtag_SF_inclusive_jets`, `BCtag_Stats_pT_3`, `BCtag_Stats_pT_4` and `BCtag_Ltag`, respectively.

The `BCtag_BFFragmentation`, `BCtag_FakeMuons`, `BCtag_BDecay_up_down`, `BCtag_Stats_pT_1` and `BCtag_Stats_pT_2` have negligible contributions and are not included in the tables. Fig. 7.11 shows the BCtag $\pm$ 1 σ variation.

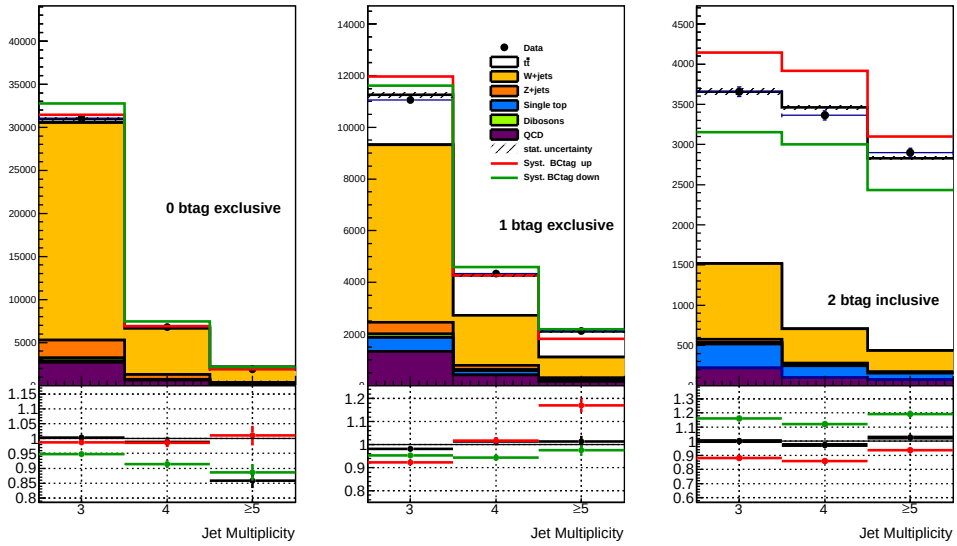

Figure 7.11: Global BC-tagging $\pm$ 1 σ variation in the nine jet bins for the muon channel. Note that this uncertainty is not the one used in the analysis. The breakdown into 13 different component is used instead.

- **Missing transverse energy determination** To account for this effect a 10% flat uncertainty, correlated to both the cell-out and soft jet terms of the $E_{\mathrm{T}}^{\mathrm{miss}}$, is applied and the $E_{\mathrm{T}}^{\mathrm{miss}}$ is recomputed. This is done using the `Top_MET_Tool`. The effect of this uncertainty is negligible and has been removed.

- **Effect of the Liquid Argon hole**: During a period of the 2011 run, there was a hardware problem in the liquid Argon calorimeter - several front end boards

(FEBs) sttoped working - creating a hole in the acceptance region. For the affected data, events are discarded if a jet is close to that region. This procedure is applied to both data and MC in the relevant period (runs 180614 to 185352). The p_{T} threshold for jet removal is set to 20 GeV. For data, this threshold is determined using the jet p_{T} corrected to account for the energy lost in the dead FEBs, whereas for MC, which does not have the hardware failure, the regular jet p_{T} is used. This means that there is a systematic uncertainty associated with the veto. The `MET_Cleaning_Utils` tool is used to perform the events removal. The systematic uncertainty associated to removing the hole is obtained by running the tool with the jet p_{T} threshold varied by ± 4 Gev, *i.e.* at 16 and 24 GeV. The effect of this uncertainty is negligible and has been removed.

- **Backgrounds normalization**: The amount of W+jets in the selected data sample is obtained by the fit, thus it is not subject to systematic uncertainty. On the other hand, both the QCD multi-jet background and the small backgrounds (Z+jets, diboson production and single top) are fixed in the fit to their expectations. We repeat the fit varying these fixed expectations by their uncertainties which amount to 50% for QCD multi-jet background untagged, and 100 % for QCD multi-jet background tagged scenarios, 100% to Z+jets, 10% for single top [100] [101] and 5% for diboson production [93], respectively. The uncertainties are taken as fully correlated between jet bins, but uncorrelated between the e+jets and μ+jets channels. The different components of backgrounds normalization uncertainty appear in the following tables and figures under the labels `Xsect_singleTop`, `Xsect_Zjets`, `Xsect_DB`, `QCDnorm_corr_ele`, `QCDnorm_corr_ele_btag`, `QCDnorm_corr_mu` and `QCDnorm_corr_mu_btag`, respectively.

- **Berends scaling**: As mentioned in Section 7.5 the normalization of the W+jets background is difficult to predict in the high jet multiplicity bins. We use the MC predictions and rescale the contributions in the 3-, 4- and $\geq$5-jet bins by the scale factors obtained in the W+jets asymmetry analysis [94]. Furthermore, we determine the W+jets absolute normalization directly in the fit. On the other hand, the amount of the W+jets production in the different jet multiplicity bins could be obtained from the 2-jet bin by exploiting the fact that the ratio of $W+n$

to $W+n+1$ jets is expected to be constant as a function of n [102]. This ratio has a spread around its central value of 24%, which we use as additional systematic uncertainty once in the 4-jet bin and twice in the 5-jet bin. This uncertainty appears in the following tables and figures under the label `Wjets_Berends`.

- **W+jets heavy flavour content**: There is an overlap between the W+jets generic samples and the specific $W + b\bar{b}$, $W + c\bar{c}$ and $W + c$ MC samples in the sense that some final states appear in both samples. This overlap is removed by means of the `HFOR` tool, which removes the following events: i) Those with heavy flavour generated from the matrix element and those in which the heavy-flavour quark-pairs are not matched to one reconstructed jet in the W+jets generic samples. ii) Those in which the heavy-flavour quark-pairs are not matched to one reconstructed jet in the $W + c$ samples. iii) Those in which $b\bar{b}$ pairs are not matched to one reconstructed jet and those in which $c\bar{c}$ pairs are matched to one reconstructed get in the $W + c\bar{c}$ samples. iv) Those in which $b\bar{b}$ pairs are matched to one reconstructed jet in $W + b\bar{b}$ samples.

  The W+jets heavy flavour content has been measured in data with W events with exactly two jets by studying the properties of secondary vertices inside jets. Based on these results, the MC predictions for a W-boson produced in association with b- or c-quark pairs have been scaled by a factor 1.63 ± 0.76, while the W-boson produced in association with a c-quark has been scaled by a factor 1.11 ± 0.35, keeping the total integral of events (light flavour + heavy flavour) constant. To estimate the effect of the uncertainty on the heavy fraction, modified templates are created by varying the fraction of $W+b\bar{b}$, $W+c\bar{c}$ and $W+c$ events up and down by the above uncertainties. In addition, a 25% uncorrelated uncertainty is added to account for the uncertainty on the extrapolation of the above scale factors - measured in the 2-jet bin - to higher jet multiplicity bins. The uncertainties on the $W+b\bar{b}$ and $W+c\bar{c}$ fractions are treated as fully correlated, and both uncorrelated with respect to that on the $W+c$ fraction. The different components of the heavy flavour content uncertainty appear in the following tables and figures under the labels `Wjets_HFQQ`, `Wjets_HFC`, `Wjets_HFQQ_3ex`, `Wjets_HFQQ_4ex`, `Wjets_HFQQ_5in`, `Wjets_HFC_3ex`, `Wjets_HFC_4ex` and `Wjets_HFC_5in`, respectively.

- **Initial and final state radiation (ISR/FSR)**: To evaluate the uncertainty due to ISR and FSR, five samples are generated using the AcerMC generator [103]: one at nominal value of ISR/FSR and four additional samples generated with more or less ISR or with more or less FSR. The fit is repeated using as $t\bar{t}$ signal these samples and the systematic uncertainty is taken as the maximum difference between the nominal AcerMC fit and the ISR/FSR variated ones. ISR and FSR are treated as independent sources of uncertainty. These uncertainties appear in the following tables and figures under the labels `ttbar_ISR` and `ttbar_FSR`, respectively.

- **Signal generator**: The fit using the default MC@NLO $t\bar{t}$ signal MC is compared to a fit where the $t\bar{t}$ signal has been generated with the Powheg MC [104] and Alpgen [85]. For the comparison both generators are interfaced to Herwig/Jimmy for hadronization. This uncertainty appears in the following tables and figures under the labels `ttbar_NLO_1` and `ttbar_NLO_2`.

- **Fragmentation model**: The uncertainties on the parton shower simulation are assessed by changing the fragmentation model applied to the same $t\bar{t}$ signal MC: Powheg events are hadronized with either Herwig/Jimmy or Pythia and we apply the relative difference between the two to the Mc@nlo sample. This uncertainty appears in the following tables and figures under the label `ttbar_Frag`.

The following sources of systematic uncertainties have been evaluated separately by means of pseudo-experiments (PE):

- **QCD multi-jet modelling**: The QCD multi-jet templates are replaced by alternative data-driven templates, obtained from a data sample requiring reversed lepton identification criteria, keeping the same normalization, to assess the uncertainty due to the QCD-multijet shape modelling.

- **W+jets background modelling**: The shapes of the W+jets templates are taken from the Alpgen MC generator. This generator can be tuned with several parameters, which are varied to estimate the uncertainty due to the W+jets background shape. The variations include a different choice of the Q^2 scale using the option `iqopt=3`, as well as a different setting for the minimum transverse

momentum of the parton jets used by ALPGEN, `ptjmin = 10`. Only an "up variation" template is computed and the corresponding "down variation" is obtained by applying a symmetrical variation to the nominal template. Instead of reconstructing large sets of MC events with the different settings, we reweight the nominal samples with weights derived in a generator-level study.

- **Parton distribution functions (PDF)**: The recommedations of the PDF4LHC working group to evaluate the uncertainties due to the PDFs are followed. The quoted value is the one obtained in the 700 pb^{-1} analysis [105].

- **Monte Carlo statistics**: To assess the effect of the limited MC statistics used to build the templates, 1000 PE have been generated varying the content of each bin by Gaussian fluctuations of the bin error. The RMS of the distributions of the fitted $k_{t\bar{t}}$ and R_b are taken as systematic uncertainties.

- **Uncertainty on the procedure to generate Wq events**:

  The procedure to generate Wb-Wq and Wq-Wq events from MC@NLO, explained in Sec. 7.7, has an associated uncertainty. This uncertainty has been evaluated from 100 PSE using the original PROTOS samples as a pseudo-data and the modified PROTOS samples as a reference. This check has been done for different values of R_b close to unity. The procedure uncertainty is estimated to be 2% between $R_b = 0.7$ and $R_b = 1$. This error will be added in quadrature to the final uncertainty.

Tab. 7.5 presents the a priori expected results on the profile likelihood. The expected uncertainties have been estimated running 40 pseudo-experiments, together with the complete set of nuisance parameters and uncertainties. The expected results of the ensemble testing show no bias in the measured $\sigma_{t\bar{t}}$, k_{W+jets}, R_b and the nuisance parameters. As we will see in next Section, the a priori expected uncertainties are well compatible with the measured ones. Finally, Fig. 7.12 shows the expected correlation matrix.

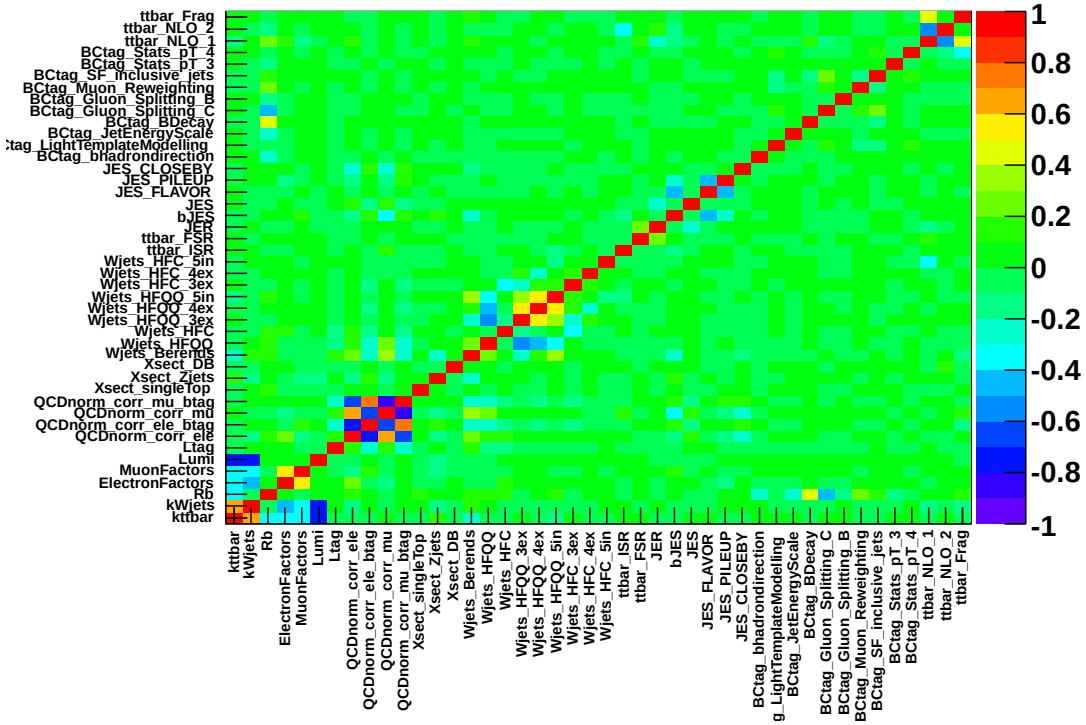

Figure 7.12: Correlation matrix for the electron and muon combined fit (40 Pseudo-experiments) with R_b allowed to vary.

Table 7.5: Expected results of the fit with 1035 pb^{-1}. The α factors correspond to the values of the nuisance parameters that better fit the data and the $\Delta\alpha$'s to the ranges covering the 68 % confidence level. The expected results show no bias.

k_{ttbar}	1.004	0.054/-0.048
k_{Wjets}	0.997	0.054/-0.050
R_b	1.009	0.031/-0.035
Systematic	α	$\Delta\alpha$
ElectronFactors	-0.064	0.850/-0.855
MuonFactors	0.065	0.481/-0.452
Lumi	-0.039	0.868/-0.853
QCDnorm_corr_ele	0.036	0.397/-0.418
QCDnorm_corr_ele_btag	-0.007	0.290/-0.254
QCDnorm_corr_mu	-0.017	0.601/-0.647
QCDnorm_corr_mu_btag	0.013	0.392/-0.269
Xsect_singleTop	0.065	0.939/-0.947
Xsect_Zjets	0.040	0.258/-0.262
Xsect_DB	-0.000	1.002/-0.977
Wjets_Berends	0.010	0.088/-0.089
Wjets_HFQQ	0.001	0.368/-0.395
Wjets_HFC	-0.006	0.759/-0.782
Wjets_HFQQ_3ex	-0.033	0.626/-0.647
Wjets_HFQQ_4ex	-0.042	0.593/-0.613
Wjets_HFQQ_5in	0.077	0.665/-0.684
Wjets_HFC_3ex	0.008	0.793/-0.817
Wjets_HFC_4ex	0.023	0.904/-0.913
Wjets_HFC_5in	-0.037	0.938/-0.947
ttbar_ISR	-0.015	0.079/-0.074
ttbar_FSR	-0.021	0.110/-0.123
bJES	-0.092	0.494/-0.462
JES	0.016	0.143/-0.157
JES_FLAVOR	-0.046	0.314/-0.332
JES_PILEUP	0.018	0.226/-0.200
JES_CLOSEBY	-0.070	0.221/-0.230
JER	-0.035	0.258/-0.245

Systematic	α	$\Delta\alpha$
BCtag_bhadrondirection	-0.034	0.891/-0.852
BCtag_LightTemplateModelling	-0.073	0.855/-0.788
BCtag_JetEnergyScale	0.008	0.903/-0.991
BCtag_BDecay	0.072	0.774/-0.869
BCtag_Gluon_Splitting_C	-0.084	0.800/-0.738
BCtag_Gluon_Splitting_B	-0.027	0.864/-0.866
BCtag_Muon_Reweighting	0.057	0.834/-0.812
BCtag_SF_inclusive_jets	0.105	0.780/-0.751
BCtag_Stats_pT_3	0.038	0.888/-0.901
BCtag_Stats_pT_4	0.017	0.826/-0.862
Ltag	0.092	0.718/-0.810
ttbar_NLO_1	-0.034	0.176/-0.179
ttbar_NLO_2	0.023	0.118/-0.122
ttbar_Frag	-0.042	0.160/-0.182

7.9 Results

Considering all the sources of systematic uncertainties mentioned in the previous Section, the data are fitted for the fraction of $t\bar{t}$ and W+jets events, R_b, and the magnitude of the nuisance parameters.

The result of the fit is shown in Tab. 7.6 for the fit that allows R_b to vary. Figures 7.13 and 7.14 show the three-jet invariant mass distributions after the fit for the selected data superimposed on the SM prediction. The $t\bar{t}$ and W+jets contributions have been scaled, and the shapes of the MC samples have been morphed, in accordance with the results of the fit. In Appendix F dispersion of the expected errors of the nuisance parameters and the fitted value in data are shown. The fits for the electron and muon data samples separately are shown in Appendix D for the fit where R_b is allowed to vary. The fit result for the case when R_b is fixed to one is shown in Appendix E.

Fig. 7.15 shows the correlation matrices for the fit where R_b is allowed to vary. Finally, Fig. 7.16 shows the fitted values of the nuisance parameters for the R_b allowed to vary fit together with the values corresponding to the separate fits to the electron and muon data samples.

Table 7.6: Fit to electron and muon combined data with R_b free.

k_{ttbar}	1.024	0.059/-0.054
k_{Wjets}	1.052	0.065/-0.062
R_b	1.002	0.034/-0.042
Systematic	α	$\Delta\alpha$
ElectronFactors	-0.201	0.912/-0.924
MuonFactors	0.615	0.549/-0.552
Lumi	0.114	0.985/-0.992
QCDnorm_corr_ele	-0.210	0.468/-0.452
QCDnorm_corr_ele_btag	-1.224	0.276/-0.306
QCDnorm_corr_mu	0.276	0.711/-0.697
QCDnorm_corr_mu_btag	-0.775	0.216/-0.207
Xsect_singleTop	0.388	0.966/-0.977
Xsect_Zjets	0.754	0.285/-0.283
Xsect_DB	-0.108	1.004/-0.995
Wjets_Berends	-0.185	0.092/-0.095
Wjets_HFQQ	0.715	0.407/-0.402
Wjets_HFC	0.162	0.786/-0.790
Wjets_HFQQ_3ex	0.408	0.657/-0.670
Wjets_HFQQ_4ex	0.324	0.624/-0.621
Wjets_HFQQ_5in	-0.297	0.677/-0.672
Wjets_HFC_3ex	-0.412	0.849/-0.819
Wjets_HFC_4ex	0.357	0.891/-0.907
Wjets_HFC_5in	0.181	0.944/-0.960
ttbar_ISR	-0.102	0.079/-0.103
ttbar_FSR	-0.104	0.111/-0.108
bJES	0.481	0.378/-0.416
JES	-0.587	0.121/-0.090
JES_FLAVOR	0.908	0.187/-0.214
JES_PILEUP	0.400	0.173/-0.341
JES_CLOSEBY	0.096	0.323/-0.269
JER	-0.370	0.039/-0.037

Systematic	α	$\Delta\alpha$
BCtag_bhadrondirection	-0.142	0.798/-0.822
BCtag_LightTemplateModelling	0.200	0.789/-0.762
BCtag_JetEnergyScale	-0.040	0.804/-0.817
BCtag_BDecay	0.039	0.767/-1.041
BCtag_Gluon_Splitting_C	-0.406	0.746/-0.710
BCtag_Gluon_Splitting_B	-0.105	0.835/-0.820
BCtag_Muon_Reweighting	0.229	0.770/-0.798
BCtag_SF_inclusive_jets	0.558	0.759/-0.791
BCtag_Stats_pT_3	-0.027	0.810/-0.838
BCtag_Stats_pT_4	-0.216	0.828/-0.789
Ltag	0.409	0.706/-0.796
ttbar_NLO_1	0.399	0.263/-0.249
ttbar_NLO_2	0.265	0.182/-0.185
ttbar_Frag	-0.109	0.158/-0.164

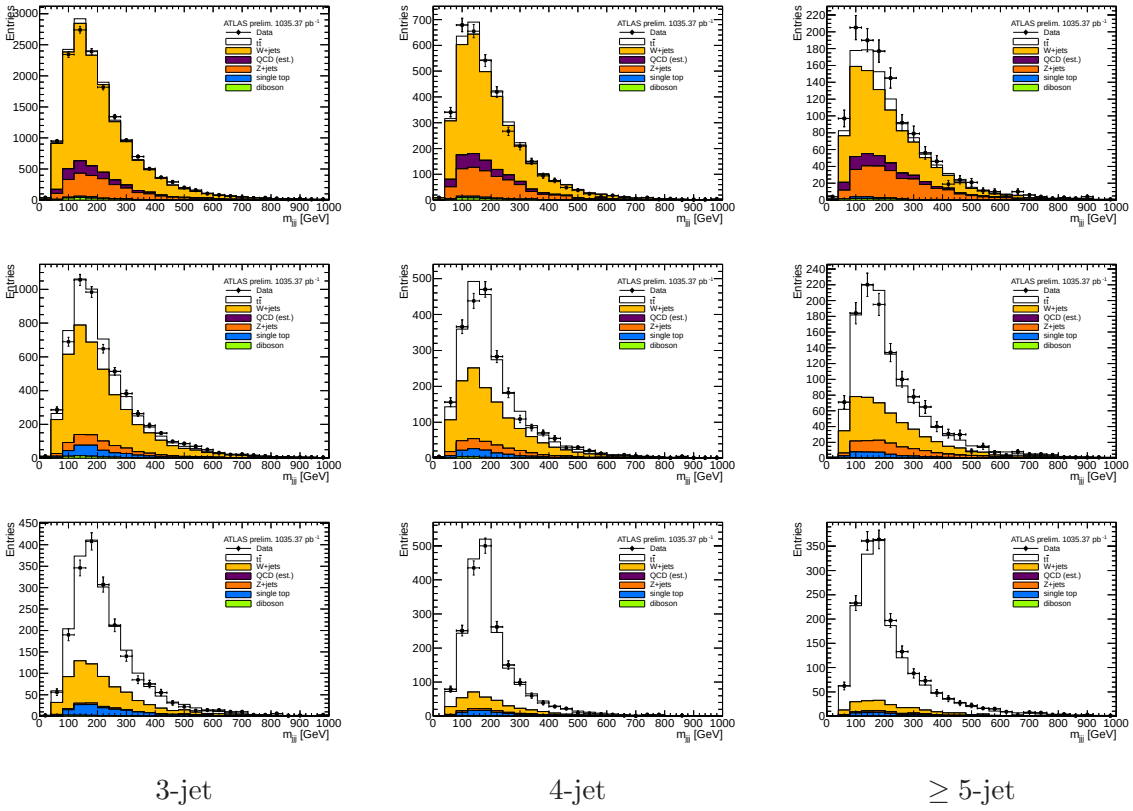

Figure 7.13: Results of the fit to combined data with R_b allowed to vary: Three-jet invariant mass in the 0- (top), 1- (medium) and $\geq$ 2- (bottom) b-jet multiplicity bins in the electron channel. The data (dots with error bars) are compared to the expectation. The shapes of the MC samples are morphed according to the results of the fit.

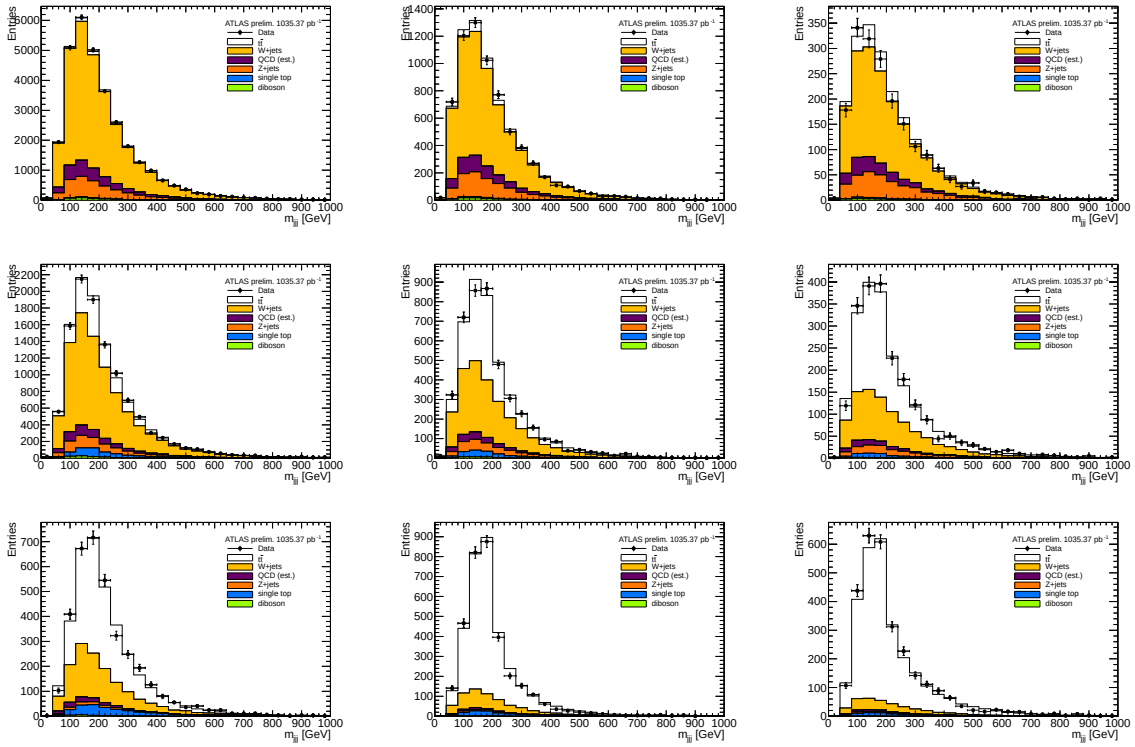

3-jet 4-jet $\geq$ 5-jet

Figure 7.14: Results of the fit to combined data with R_b allowed to vary: Three-jet invariant mass in the 0- (top), 1- (medium) and $\geq$ 2- (bottom) b-jet multiplicity bins in the muon channel. The data (dots with error bars) are compared to the expectation. The shapes of the MC samples are morphed according to the results of the fit.

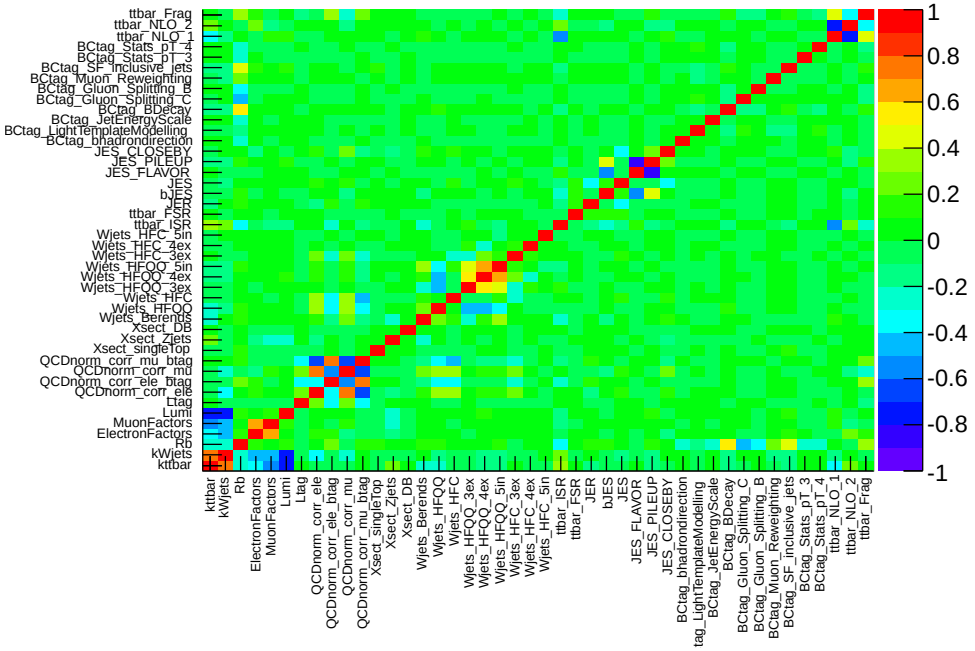

Figure 7.15: Correlation matrix for the electron and muon combined data fit with R_b allowed to vary.

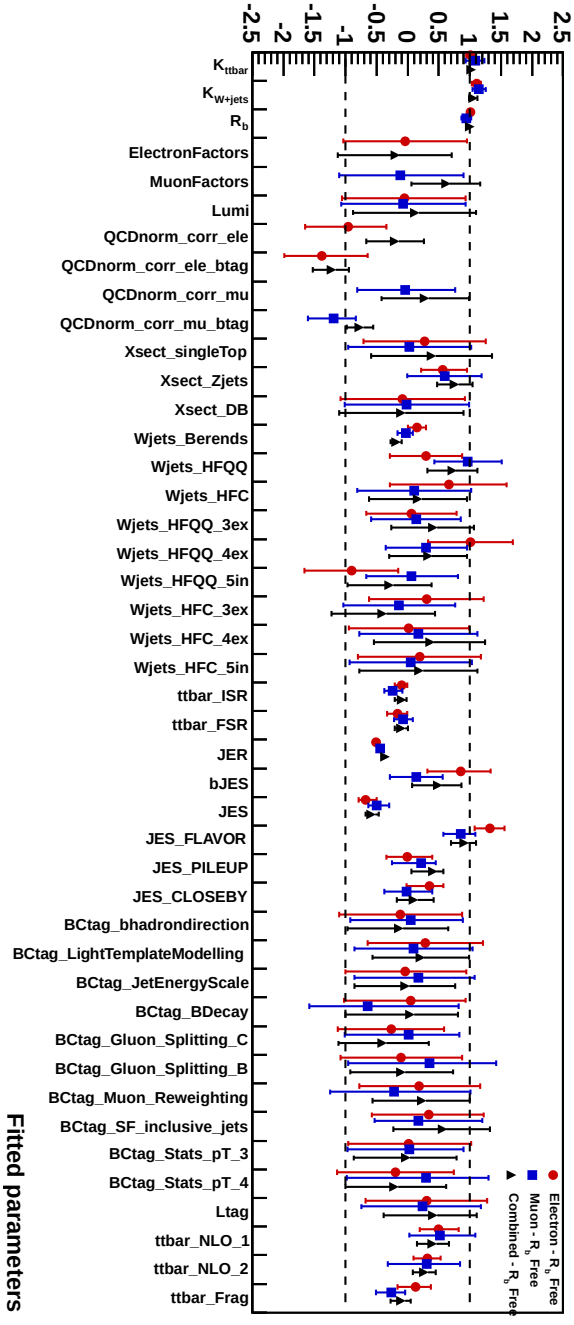

Figure 7.16: Nuisance distribution for fits to data with R_b allowed to vary. Electron, muon and combined data are shown.

Table 7.7 summarizes the results of the fits shown in this section and Appendices E and D.

Table 7.7: The measured $k_{t\bar{t}}$, k_{Wjets} and R_b are shown for the fit to the electron and muon samples separately and for the combined fit. The top row shows the result corresponding to R_b set to one and the three bottom ones to the results for R_b allowed to vary.

Data sample	$k_{t\bar{t}}$	k_{Wjets}	R_b
e or μ + jets	1.024+0.059−0.053	1.052+0.065−0.061	1
e + jets	1.008+0.067−0.063	1.104+0.076−0.074	1.011+0.033−0.037
μ + jets	1.083+0.151−0.135	1.148+0.109−0.104	0.943+0.082−0.041
e or μ + jets	**1.024+0.059−0.054**	**1.052+0.065−0.062**	**1.002+0.034−0.042**

Finally, Tab. 7.8 shows the values of the systematic uncertainties that have been computed outside the fit. To that purpose, 100 pseudo-experiments have been run with the same settings of the profile fit but changing one of the models at a time.

Table 7.8: Systematic uncertainties computed outside the fit for the R_b free scenario.

Data sample	$k_{t\bar{t}}$ (%)	R_b (%)
QCD multijet modelling	-0.2	+0.7
W+jets iopt3	-0.7	+3.2
W+jets ptjmin1	+0.8	+2.0
PDF	+1.0	+1.0
MC Statistics	+0.7	+0.6
Procedure Wq events	+2.0	+2.0
Total	2.6	4.5

Including the out of profile systematics of Tab. 7.8, the final result for the cross-section measurement in the R_b free scenario is:

$$k_{t\bar{t}} = 1.024 \pm 1.3\%(\text{Stat.})^{+5.9}_{-5.4}\%(\text{Syst.}) \pm 2.6\%(\text{Out.}) \tag{7.14}$$

$$R_b = 1.00 \pm 1.0\%(\text{Stat.})^{+3.4}_{-4.2}\%(\text{Syst.}) \pm 4.5\%(\text{Out.}) \tag{7.15}$$

As mentioned in Sec. 7.6, the profile likelihood provides the total uncertainty on the fitted quantities, but the contribution of each single uncertainty is not well defined as the fit takes into account the correlation among the nuisance parameters in the minimization process. To have an estimation of the relative importance of each systematic, the fit is repeated fixing one nuisance parameter to its fitted value at a time and getting the corresponding systematic uncertainty as the quadratic difference between the new total error and the nominal one. The result of this exercise is shown in Tab. 7.9.

Table 7.9: Observed results of the fit with 1035 pb^{-1}: The α factors correspond to the values of nuisance parameters that better fit the data and the $\Delta\alpha$s to the ranges covering the 68% confidence level. The expected results show no bias.

Nuisance parameters	$\Delta k^{+}_{t\bar{t}}$	$\Delta k^{-}_{t\bar{t}}$	ΔR^{+}_{b}	ΔR^{-}_{b}
Object selection				
Lepton Factors(%)	+2.6	-2.3	+0.1	-0.1
Jet Related systematics (%)	+1.9	-1.2	+0.1	-1.4
Heavy-flavour tagging (%)	+0.1	-1.0	+3.0	-4.0
Light-flavour tagging (%)	+1.0	-0.1	+0.1	-0.9
Background rate				
QCD multijet (%)	+1.3	-0.4	+0.5	-1.2
Z+jets cross-section (%)	+1.2	-0.9	+0.1	-1.2
Single top cross-section (%)	+3.1	-0.2	+0.1	-1.1
Dibosons cross-section (%)	+0.9	-0.1	+0.1	0.8
Background modelling				
$W + jets$ (%)	+2.5	-2.2	+0.1	1.4
$t\bar{t}$ signal modelling				
Initial and Final state radiation (%)	+1.1	-1.5	+0.1	-0.4
Fragmentation model (%)	+1.5	-1.0	+0.1	-1.4
Signal generator (%)	+2.0	-1.4	+0.1	-0.8
Luminosity				
Luminosity (%)	+4.1	-3.6	+0.1	-0.9
Total of profiled systematics (%)	+5.9	-5.6	+3.4	-4.2
Out of profile				
W+jets iopt3 (%)	+0.7	-0.7	+3.2	-3.2
W+jets ptjmin1 (%)	+0.8	-0.8	+2.0	-2.0
PDF (%)	+1.0	-1.0	+1.0	-1.0
MC Statistics (%)	+0.7	-0.7	+0.6	-0.6
Procedure Wq events (%)	+2.0	-2.0	+2.0	-2.0
Statistical Uncertainty (%)	+1.3	-1.3	+1.0	-1.0
Total Uncertainty (%)	+6.4	-6.2	+5.6	-6.1

7. SIMULTANEOUS MEASUREMENT OF THE TOP QUARK PAIR PRODUCTION CROSS-SECTION AND R_B

8

Conclusions

With a data sample of 1035 pb^{-1} taken with ATLAS during the first half of the 2011 run, and performing a profile likelihood fit to the three-jet invariant mass distribution, we have measured the $t\bar{t}$ cross-section and the fraction of top- to bottom-quark decays to be:

$\sigma_{t\bar{t}} = 169.0^{+2.1}_{-2.1}(\text{stat.})^{+10.7}_{-10.2}(\text{syst.})$ pb

and

$R_b = 1.00^{+0.01}_{-0.01}(\text{stat.})^{+0.06}_{-0.06}(\text{syst.})$,

respectively.

The measurement is dominated by systematic uncertainties. Several cross-checks of this measurement are performed: the results of the likelihood applied to the individual electron and muon channels are in good agreement with each other and with the combined result. A measurement of $\sigma_{t\bar{t}}$ only was also obtained by fixing $R_b = 1$ in the fit, and the fitted result is also in good agreement with the nominal result. Finally, the fitted values are in good agreement with the theoretical predictions.

Appendix A

Inclusive selection

Table A.1: Selected events split up according to jet multiplicity in the electron channel. Scale factors obtained from the asymmetry analysis have been applied to the W+jets samples. The quoted uncertainties are statistical.

	= 1 jet	= 2 jets	= 3 jets	= 4jets	$\geq$ 5 jets
$t\bar{t}$	338.45 ± 3.41	1473.70 ± 7.13	2864.59 ± 9.92	2751.25 ± 9.75	2098.27 ±8.66
QCD	14583.27 ± 110.16	7344.57 ± 67.26	2445.02 ± 37.67	738.32 ± 21.12	237.17 ±13.37
W+jets	245522.55 ± 860.04	64307.45 ± 319.43	15577.50 ± 134.56	3648.54 ± 58.40	1171.33 ±28.38
Z+jets	5639.36 ± 49.14	3723.53 ± 39.99	1540.08 ± 25.74	520.58 ± 14.89	228.41 ±9.69
Single top	843.58 ± 13.27	1057.51 ± 13.58	574.69 ± 8.75	224.63 ± 5.00	93.94 ±3.19
Dibosons	893.80 ± 13.56	795.25 ± 12.72	263.74 ± 7.11	65.76 ± 3.54	14.25 ±1.48
Total prediction	267821.00 ±868.67	78702.01 ±329.48	23265.63 ±142.87	7949.08 ±64.89	3843.36 ±34.14
Data	265572	76498	22966	7946	4142

Table A.2: Selected events split up according to jet multiplicity in the muon channel. Scale factors obtained from the asymmetry analysis have been applied to the W+jets samples. The quoted uncertainties are statistical.

	= 1 jet	= 2 jets	= 3 jets	= 4jets	$\geq$ 5 jets
$t\bar{t}$	484.82 ± 3.64	2182.15 ± 7.71	4507.15 ± 11.07	4575.71 ± 11.16	3534.25 ±9.99
QCD	38056.50 ± 189.89	16310.95 ± 109.34	4593.82 ± 54.49	1235.84 ± 27.28	451.22 ±16.13
W+jets	584786.10 ± 1726.98	144881.02 ± 542.22	33081.07 ± 209.54	7684.10 ± 91.01	2473.14 ±43.58
Z+jets	26940.23 ± 97.94	8835.92 ± 55.70	2550.45 ± 29.63	758.86 ± 15.86	261.26 ±8.92
Single top	1554.47 ± 16.19	1824.34 ± 16.11	975.27 ± 10.16	360.15 ± 5.72	146.58 ±3.45
Dibosons	1726.00 ± 16.96	1613.66 ± 16.23	498.80 ± 8.78	119.26 ± 4.24	28.94 ±2.07
Total prediction	653548.19 ±1740.31	175648.03 ±556.46	46206.56 ±219.22	14733.91 ±97.22	6895.38 ±48.53
Data	662922	173866	45767	14517	6930

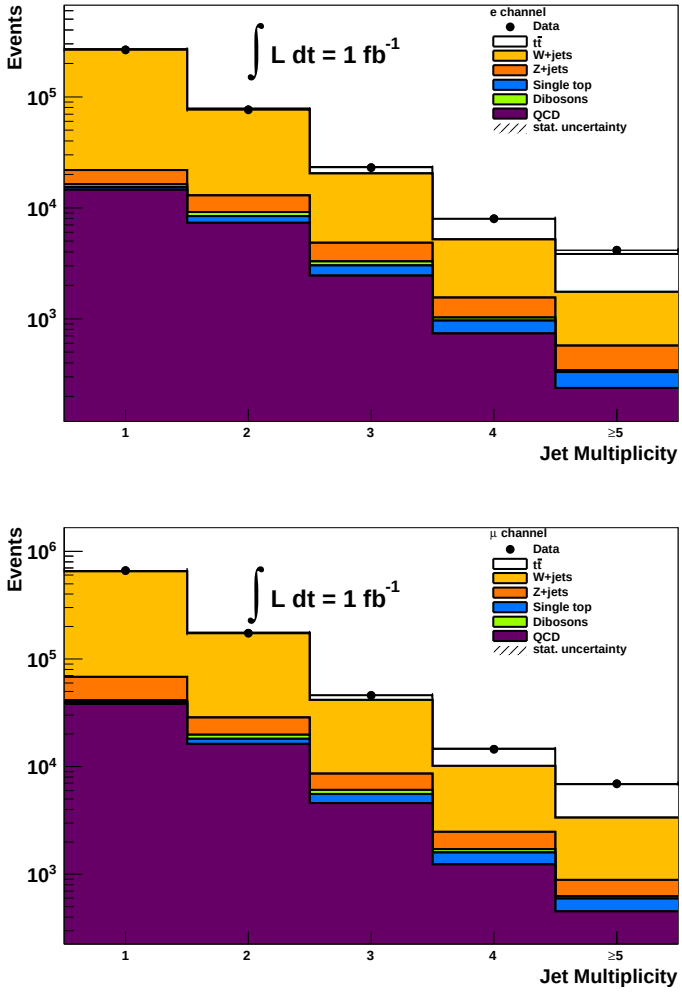

Figure A.1: Jet multiplicity in the electron (top) and muon (bottom) channels for the events passing all the selection criteria except the requirement on the minimum number of jets. The data (dots with error bars) are compared to the expectation.

Appendix B

Control Plots

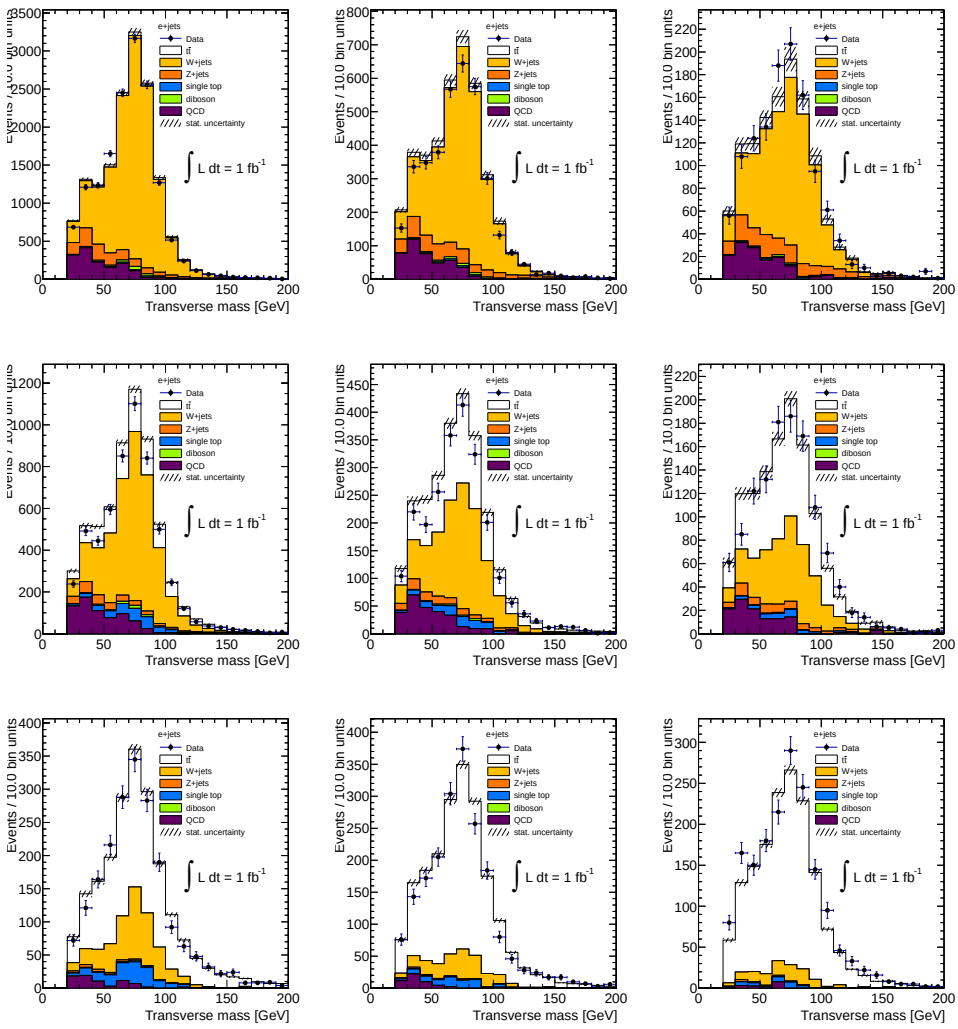

Figure B.1: Leptonic W transverse mass in the 0- (top), 1- (medium) and $\geq$ 2- (bottom) b-jet multiplicity bins for the electron data sample. The data (dots with error bars) are compared to the expectation. Scale factors obtained from the asymmetry analysis have been applied to the W+jets samples.

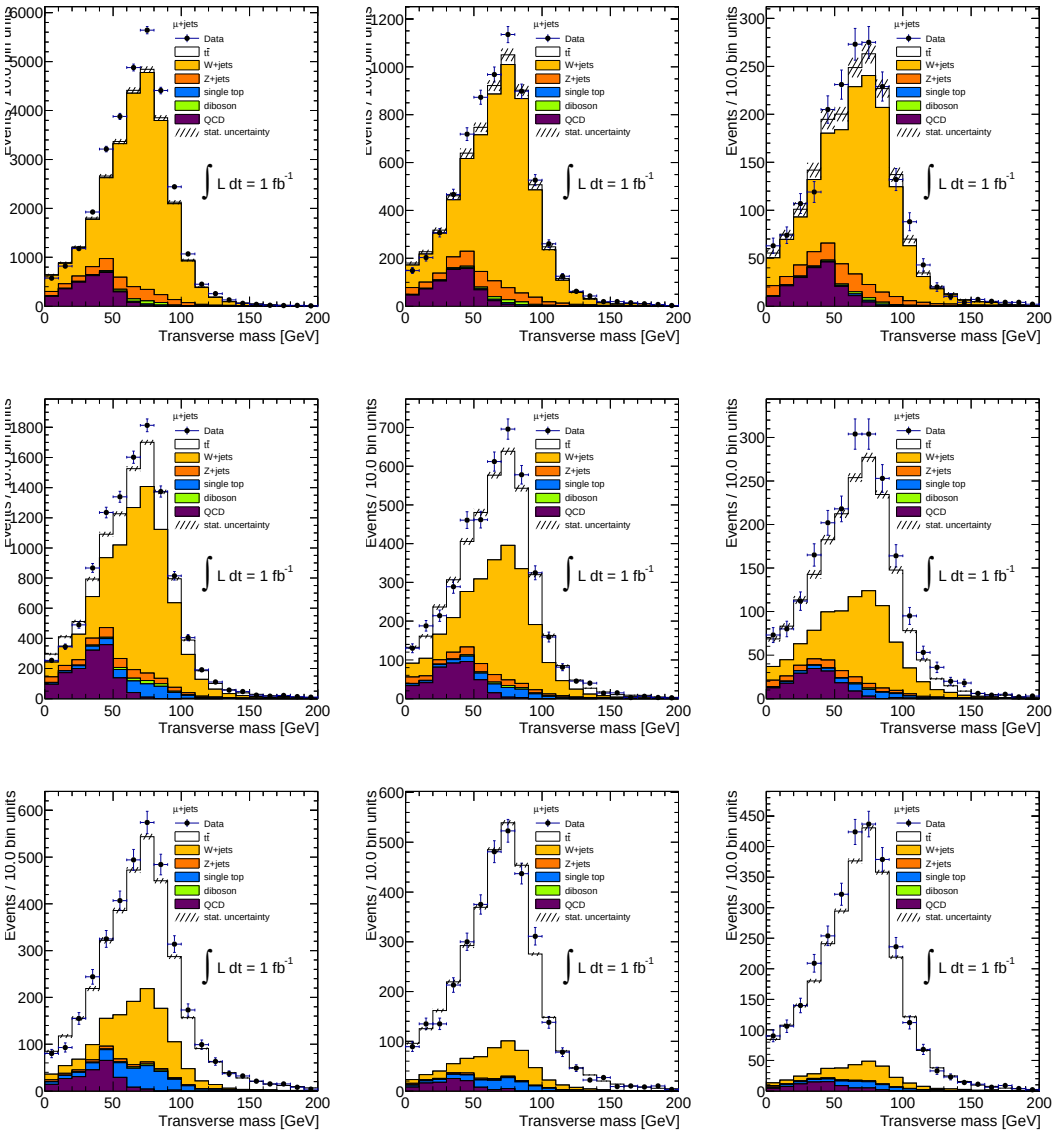

3-jet 4-jet $\geq$ 5-jet

Figure B.2: Leptonic W transverse mass in the 0- (top), 1- (medium) and $\geq$ 2- (bottom) b-jet multiplicity bins for the muon data sample. The data (dots with error bars) are compared to the expectation. Scale factors obtained from the asymmetry analysis have been applied to the W+jets samples.

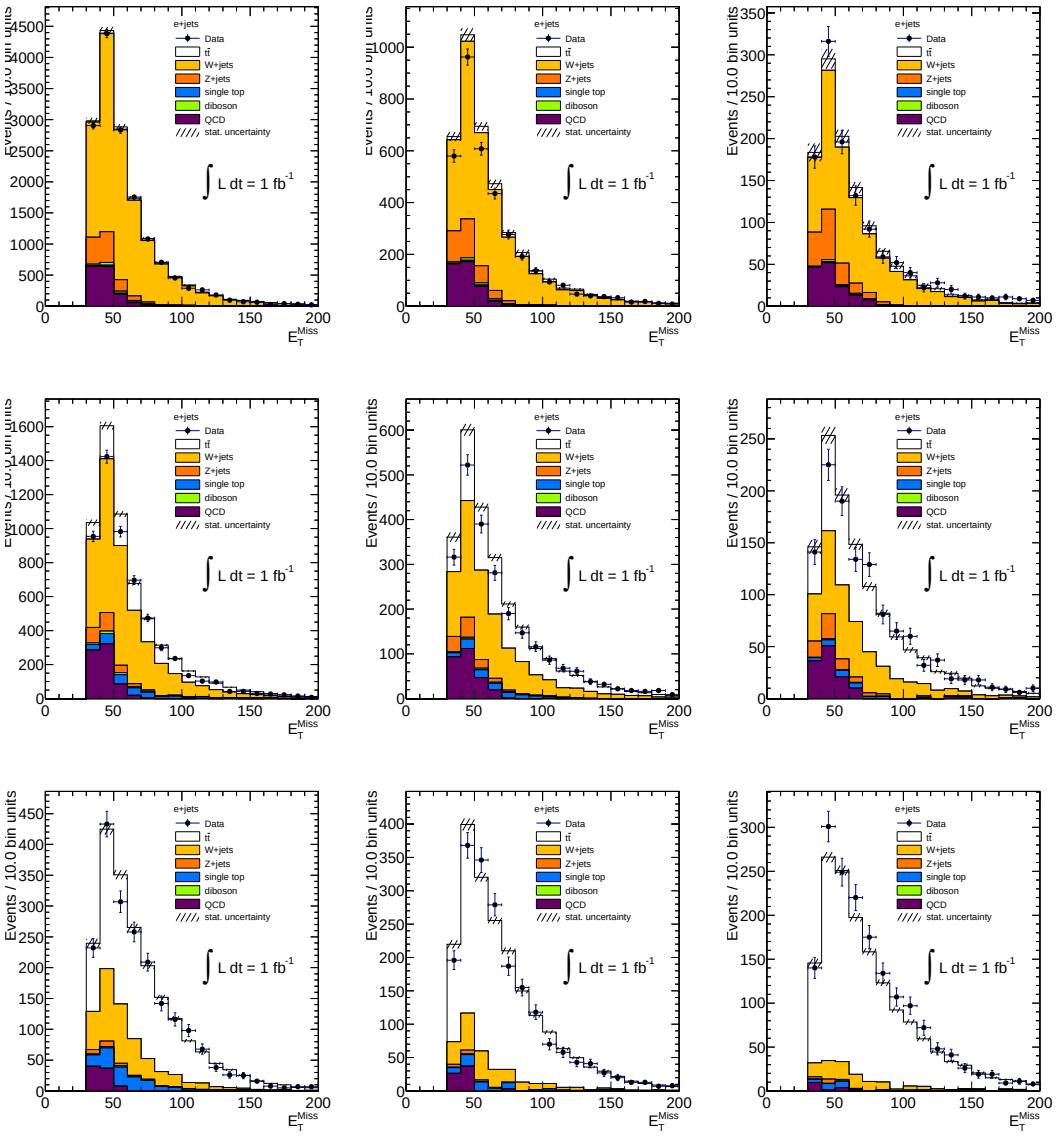

3-jet 4-jet $\geq$ 5-jet

Figure B.3: Missing transverse energy in the 0- (top), 1- (medium) and $\geq$ 2- (bottom) b-jet multiplicity bins for the electron data sample. The data (dots with error bars) are compared to the expectation. Scale factors obtained from the asymmetry analysis have been applied to the W+jets samples.

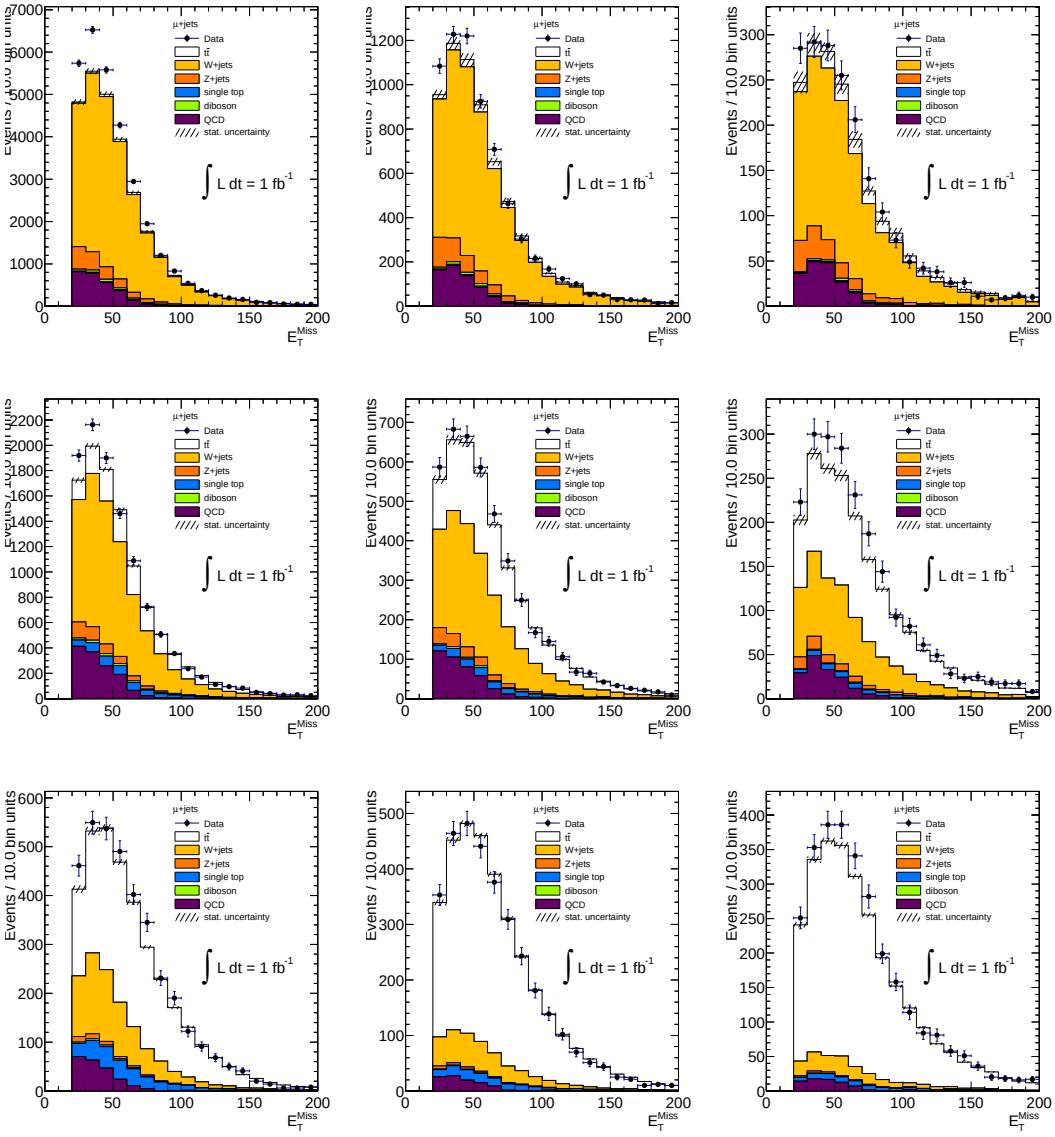

Figure B.4: Missing transverse energy in the 0- (top), 1- (medium) and $\geq$ 2- (bottom) b-jet multiplicity bins for the muon data sample. The data (dots with error bars) are compared to the expectation. Scale factors obtained from the asymmetry analysis have been applied to the W+jets samples.

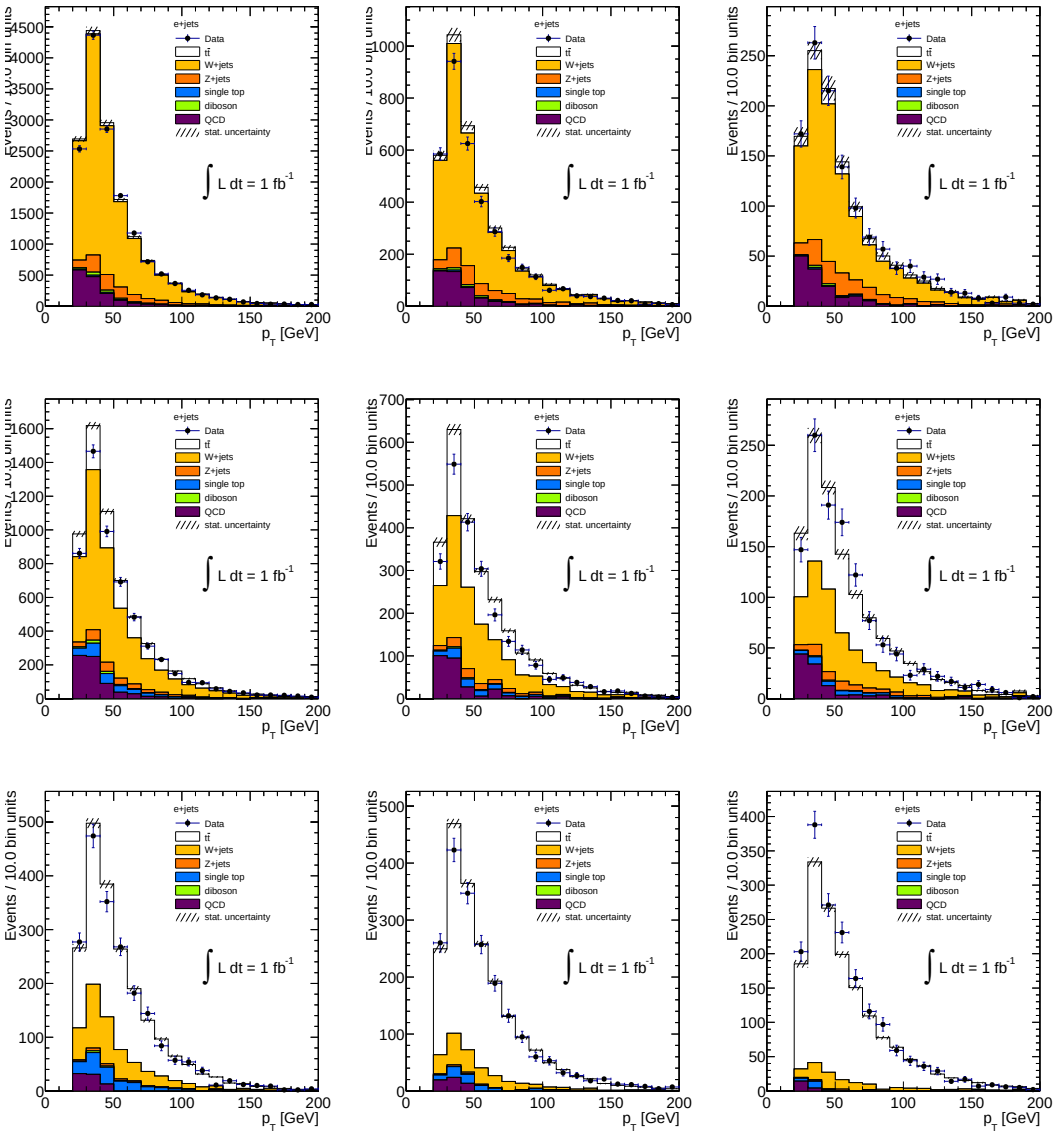

Figure B.5: Electron transverse momentum in the 0- (top), 1- (medium) and $\geq$ 2- (bottom) b-jet multiplicity bins. The data (dots with error bars) are compared to the expectation. Scale factors obtained from the asymmetry analysis have been applied to the W+jets samples.

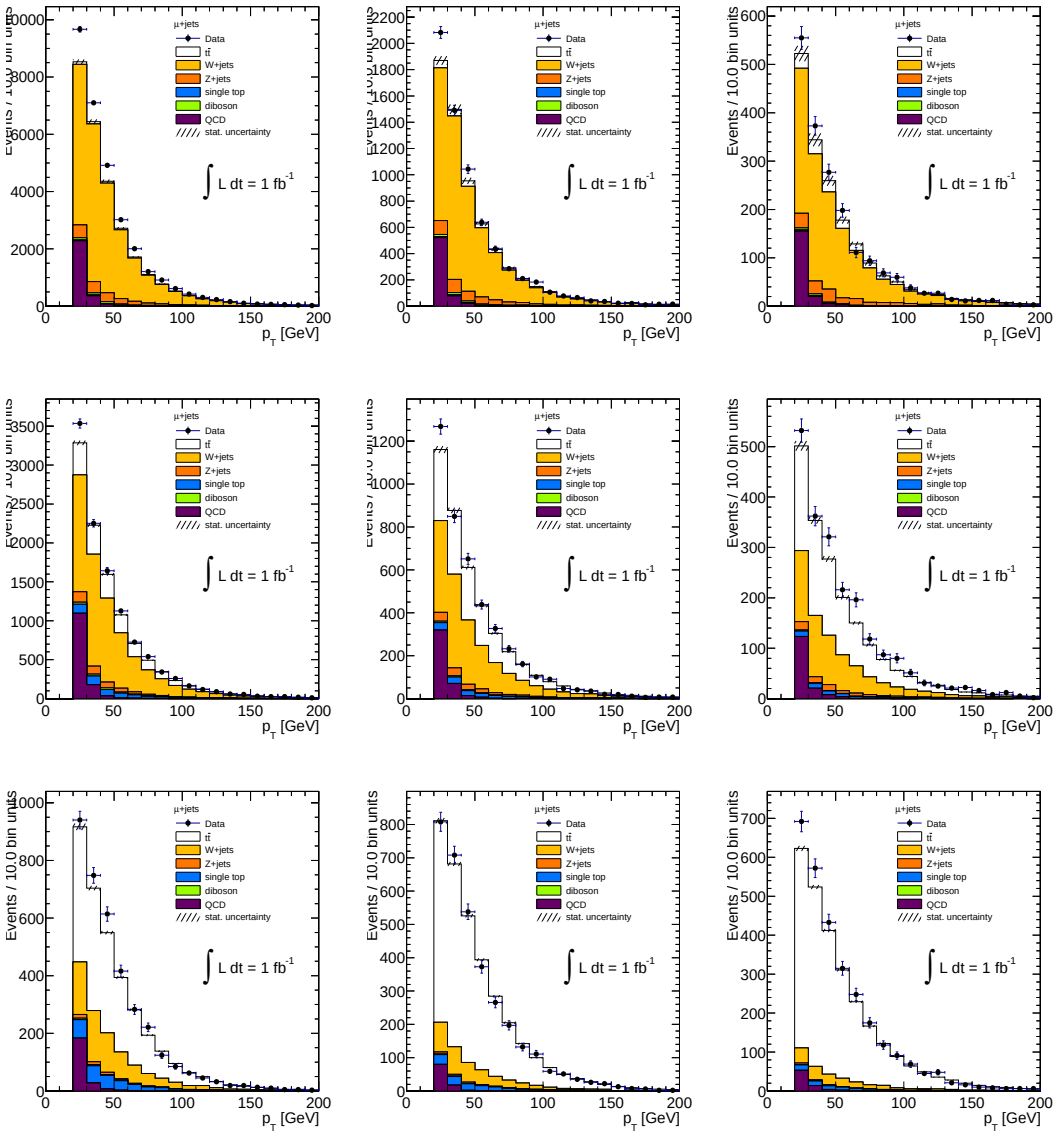

3-jet 4-jet $\geq$ 5-jet

Figure B.6: Muon transverse momentum in the 0- (top), 1- (medium) and $\geq$ 2- (bottom) b-jet multiplicity bins. The data (dots with error bars) are compared to the expectation. Scale factors obtained from the asymmetry analysis have been applied to the W+jets samples.

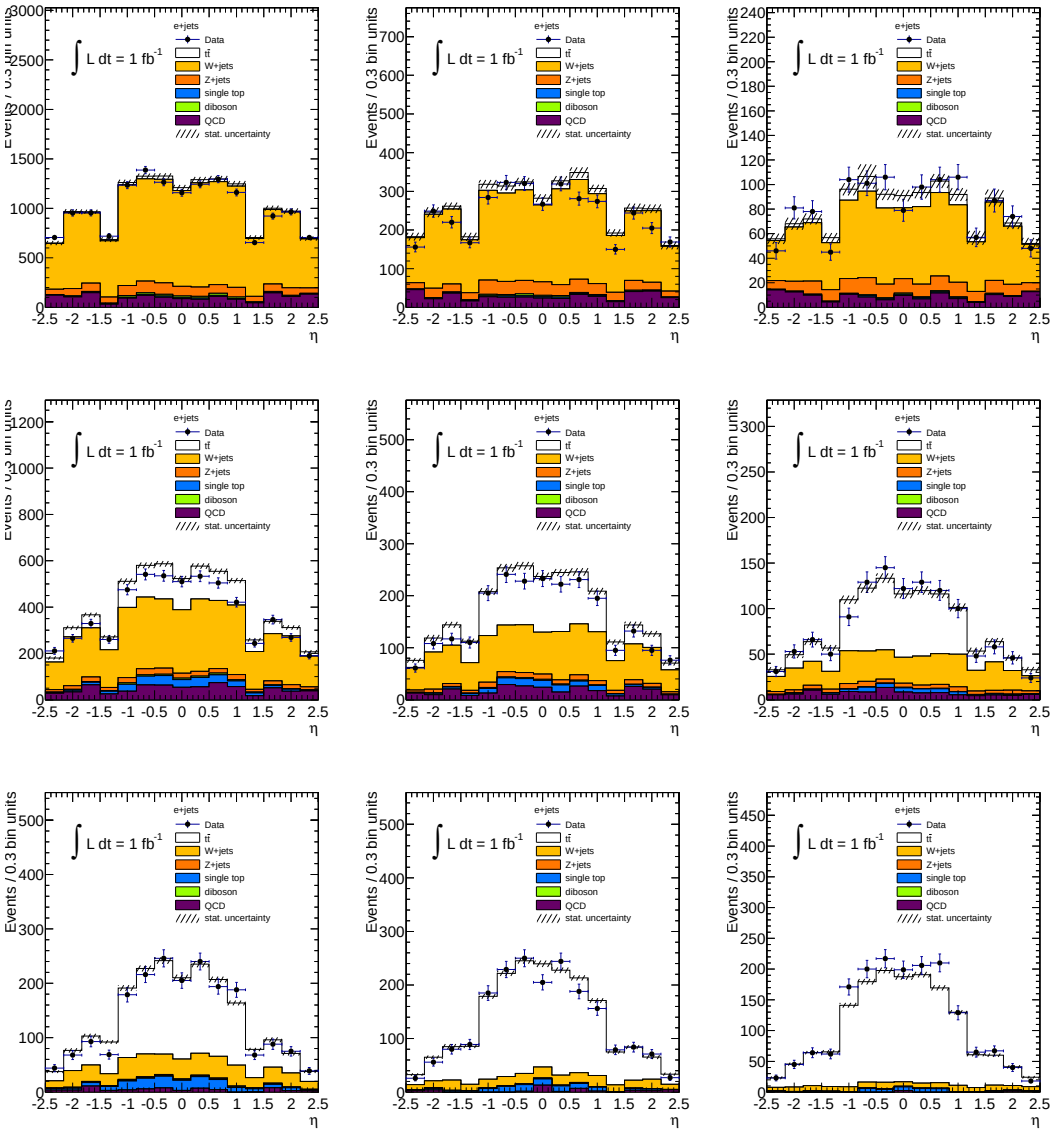

Figure B.7: Electron pseudorapidity in the 0- (top), 1- (medium) and $\geq$ 2- (bottom) b-jet multiplicity bins. The data (dots with error bars) are compared to the expectation. Scale factors obtained from the asymmetry analysis have been applied to the W+jets samples.

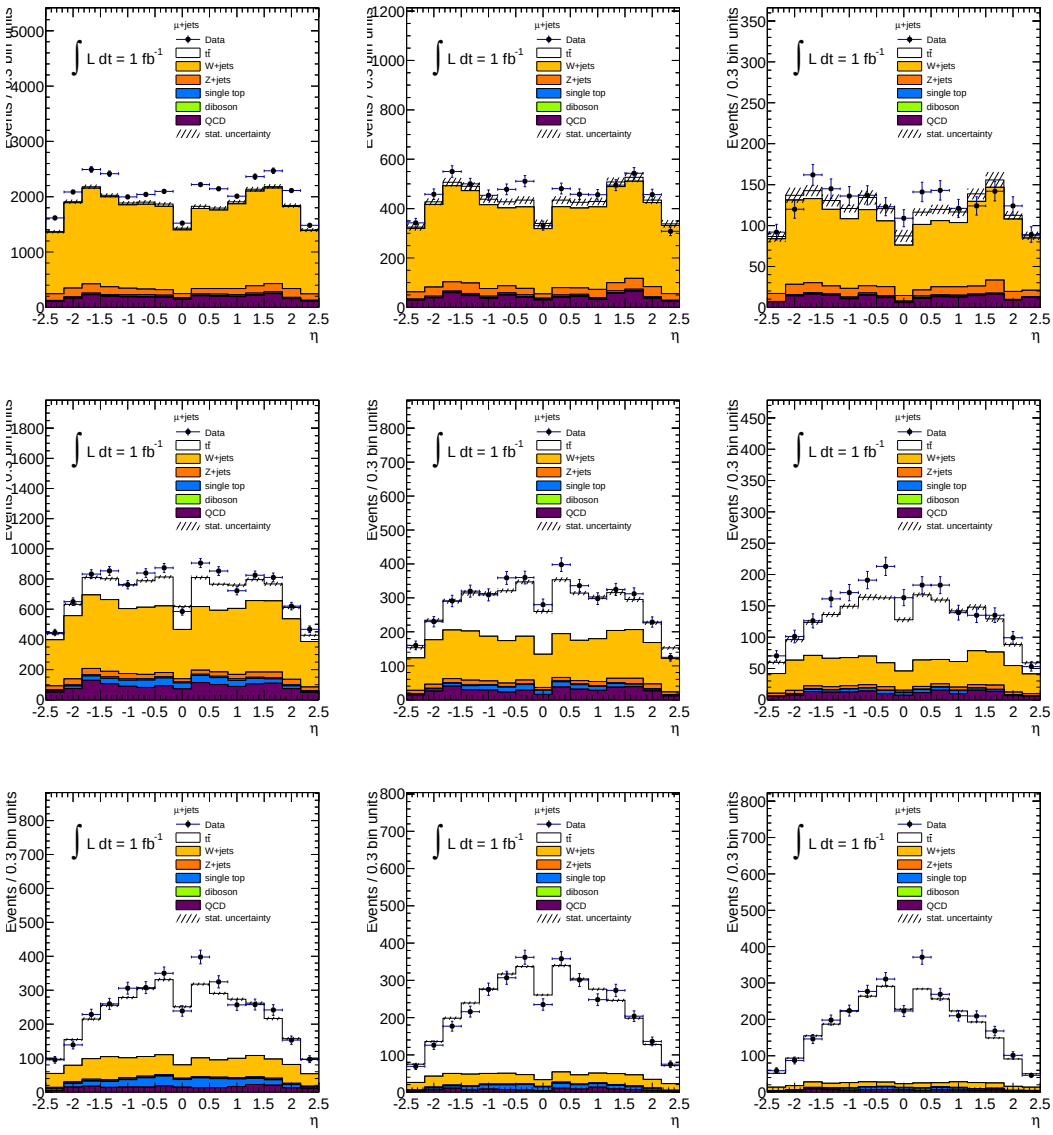

Figure B.8: Muon pseudorapidity in the 0- (top), 1- (medium) and $\geq$ 2- (bottom) b-jet multiplicity bins. The data (dots with error bars) are compared to the expectation. Scale factors obtained from the asymmetry analysis have been applied to the W+jets samples.

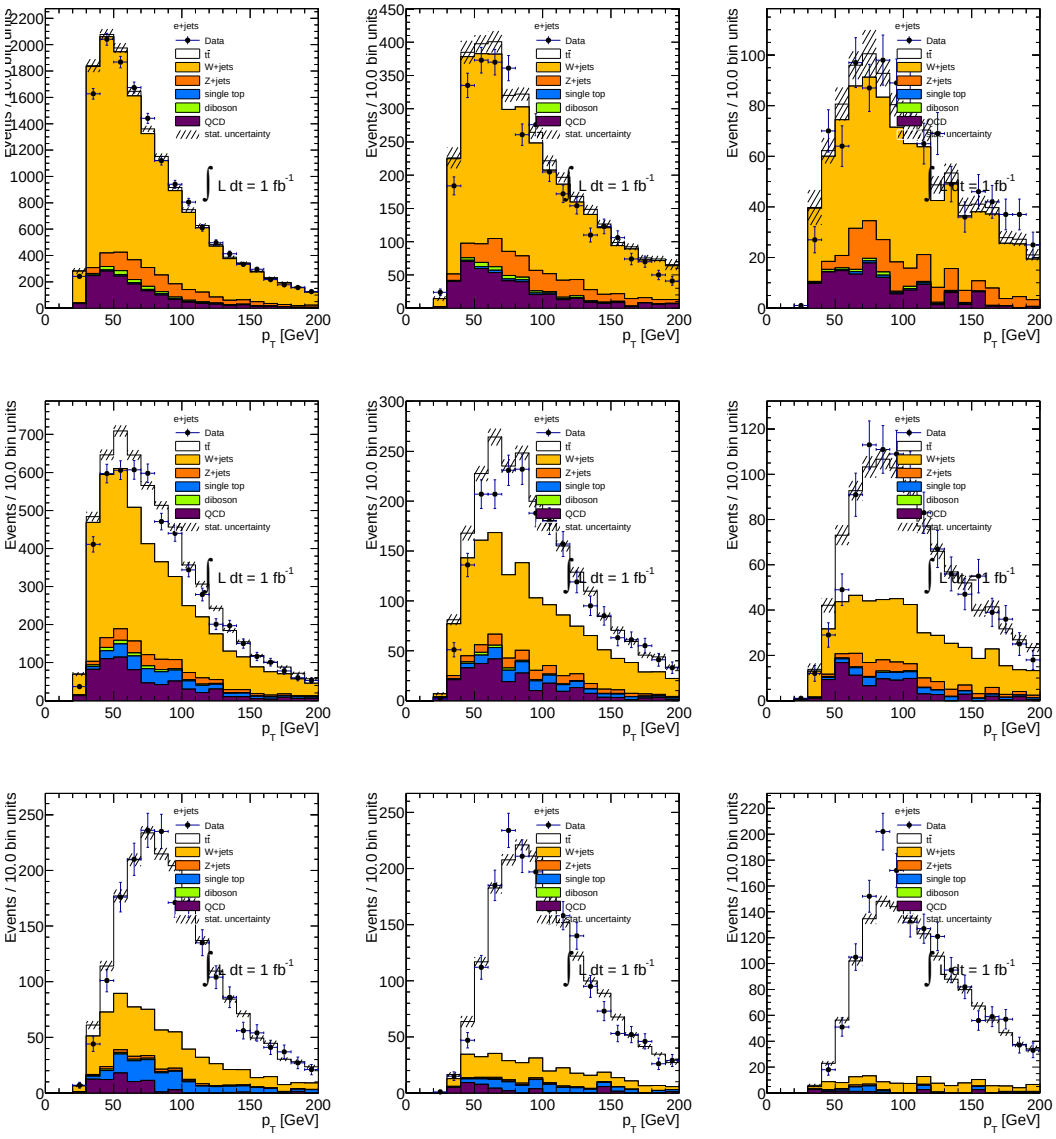

Figure B.9: Leading jet transverse momentum in the 0- (top), 1- (medium) and $\geq$ 2- (bottom) b-jet multiplicity bins for the electron data sample. The data (dots with error bars) are compared to the expectation. Scale factors obtained from the asymmetry analysis have been applied to the W+jets samples.

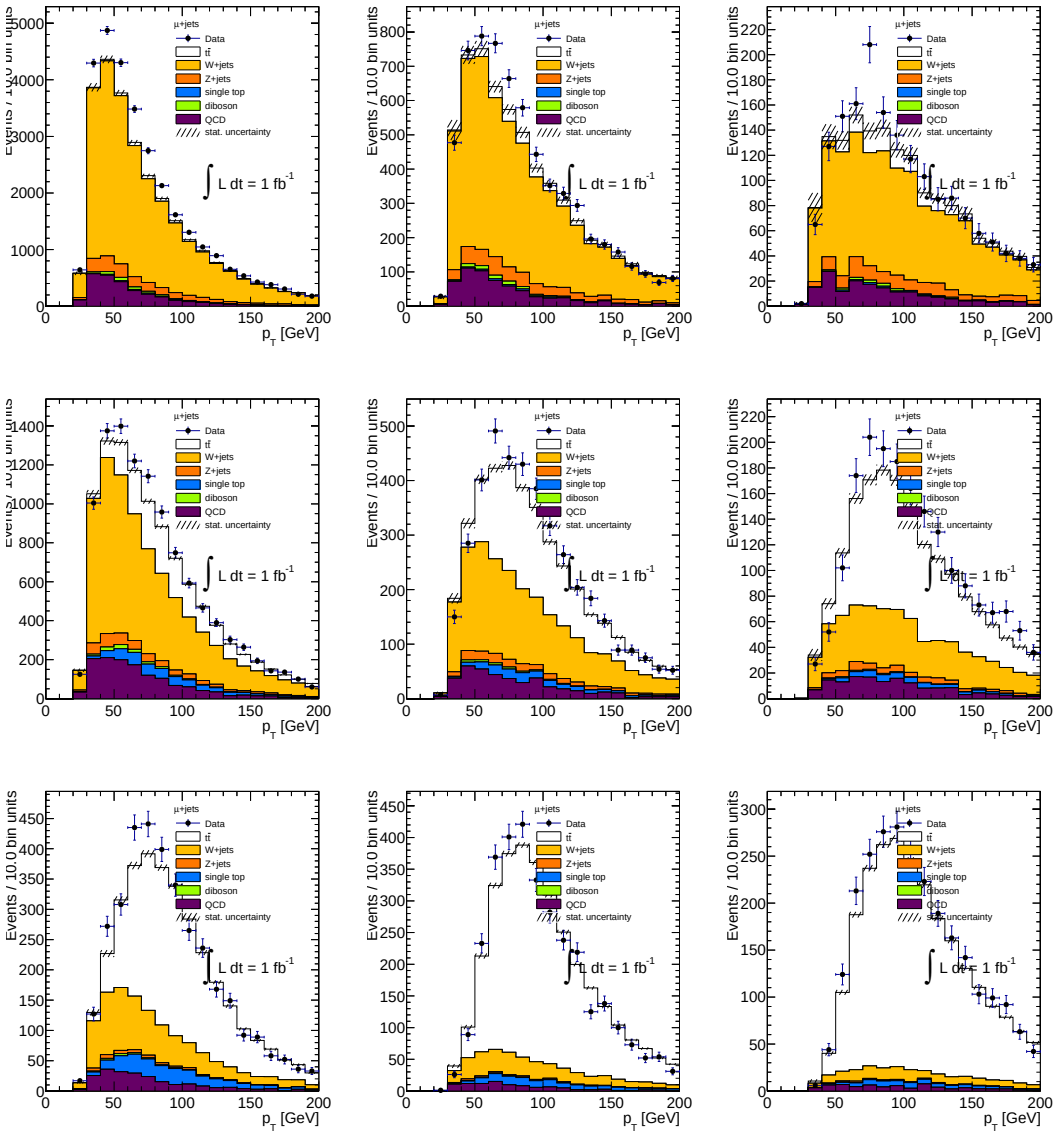

Figure B.10: Leading jet transverse momentum in the 0- (top), 1- (medium) and $\geq$ 2- (bottom) b-jet multiplicity bins for the muon data sample. The data (dots with error bars) are compared to the expectation. Scale factors obtained from the asymmetry analysis have been applied to the W+jets samples.

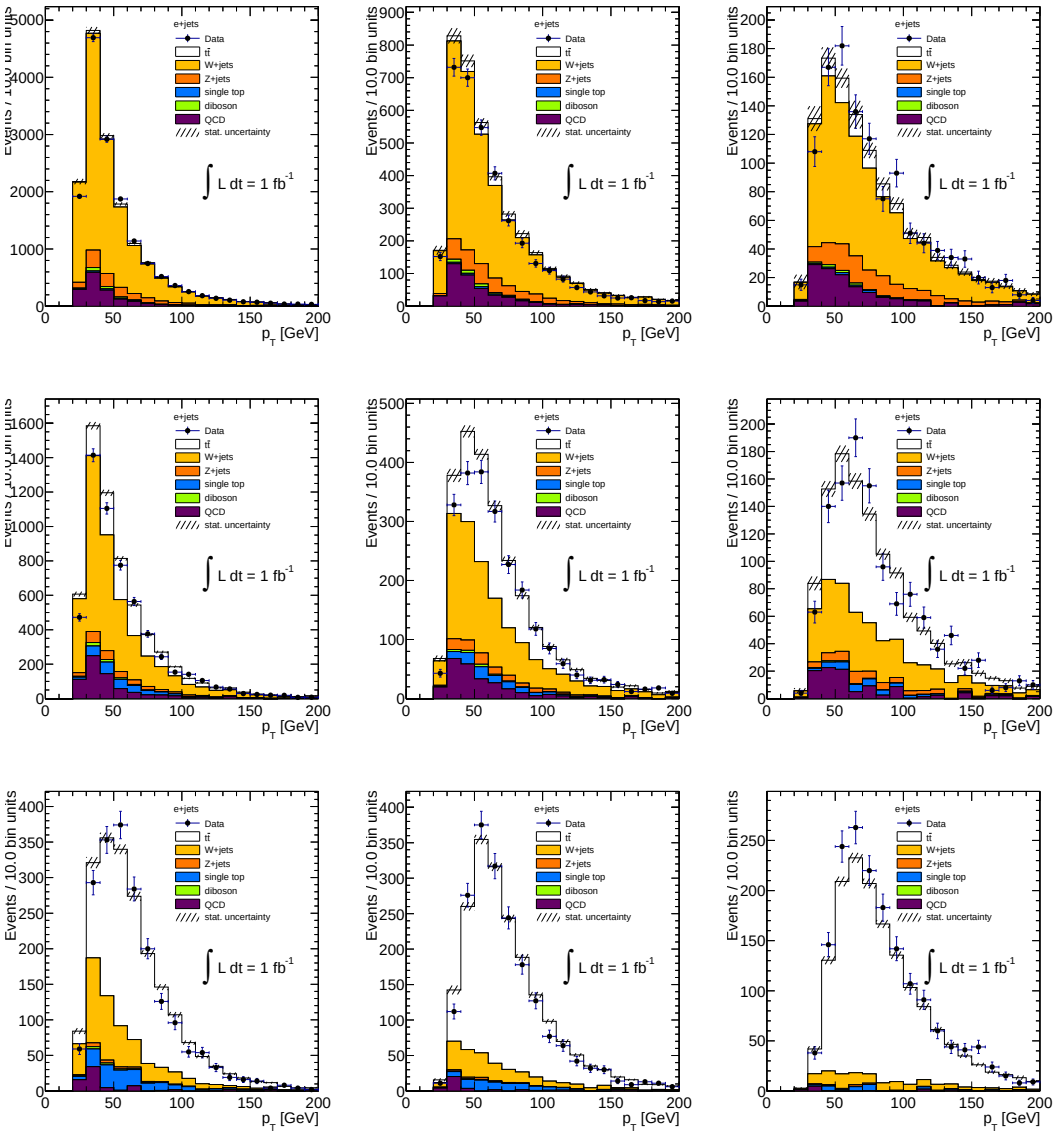

Figure B.11: Second leading jet transverse momentum in the 0- (top), 1- (medium) and $\geq$ 2- (bottom) b-jet multiplicity bins for the electron data sample. The data (dots with error bars) are compared to the expectation. Scale factors obtained from the asymmetry analysis have been applied to the W+jets samples.

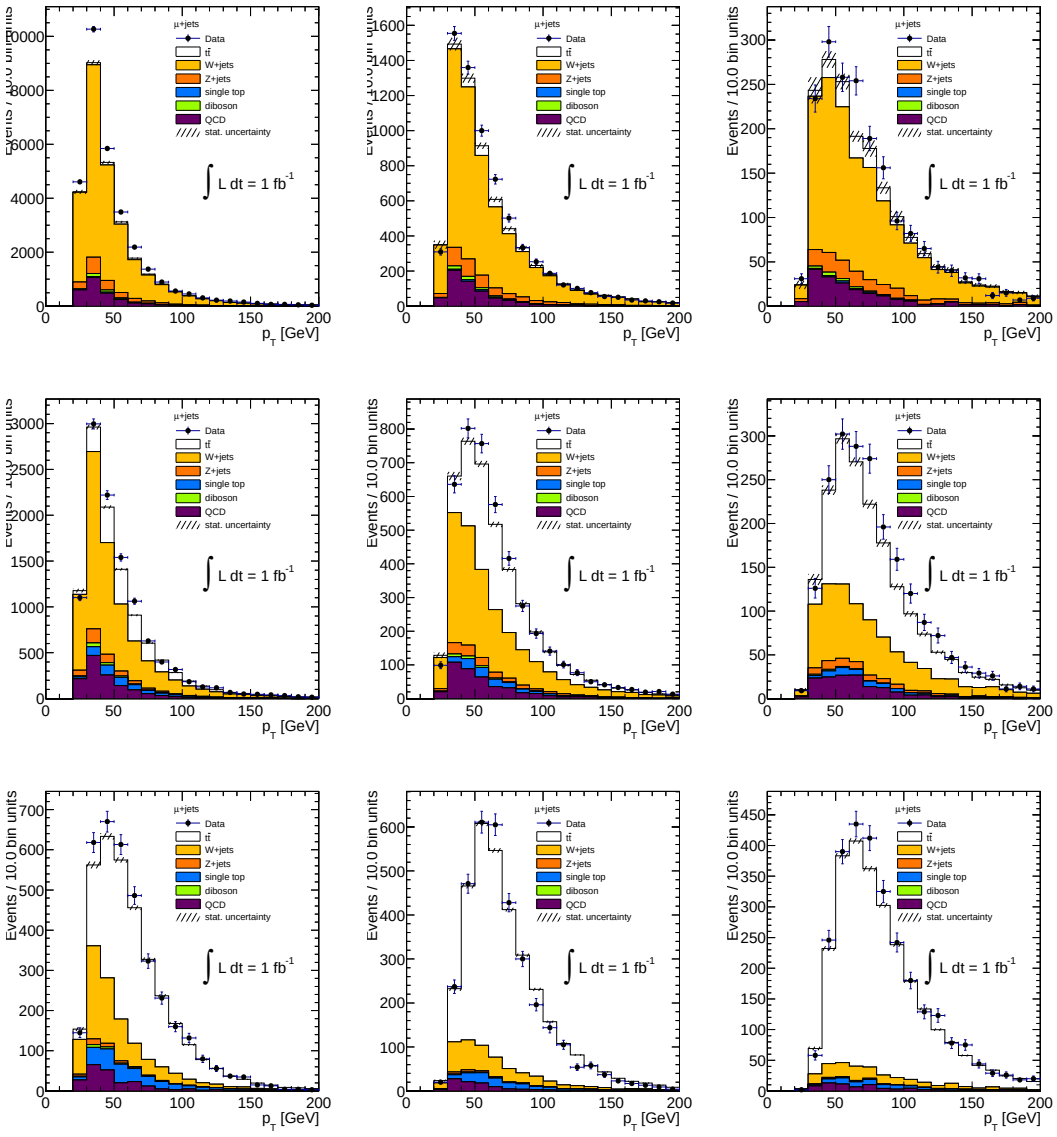

Figure B.12: Second leading jet transverse momentum in the 0- (top), 1- (medium) and $\geq$ 2- (bottom) b-jet multiplicity bins for the muon data sample. The data (dots with error bars) are compared to the expectation. Scale factors obtained from the asymmetry analysis have been applied to the W+jets samples.

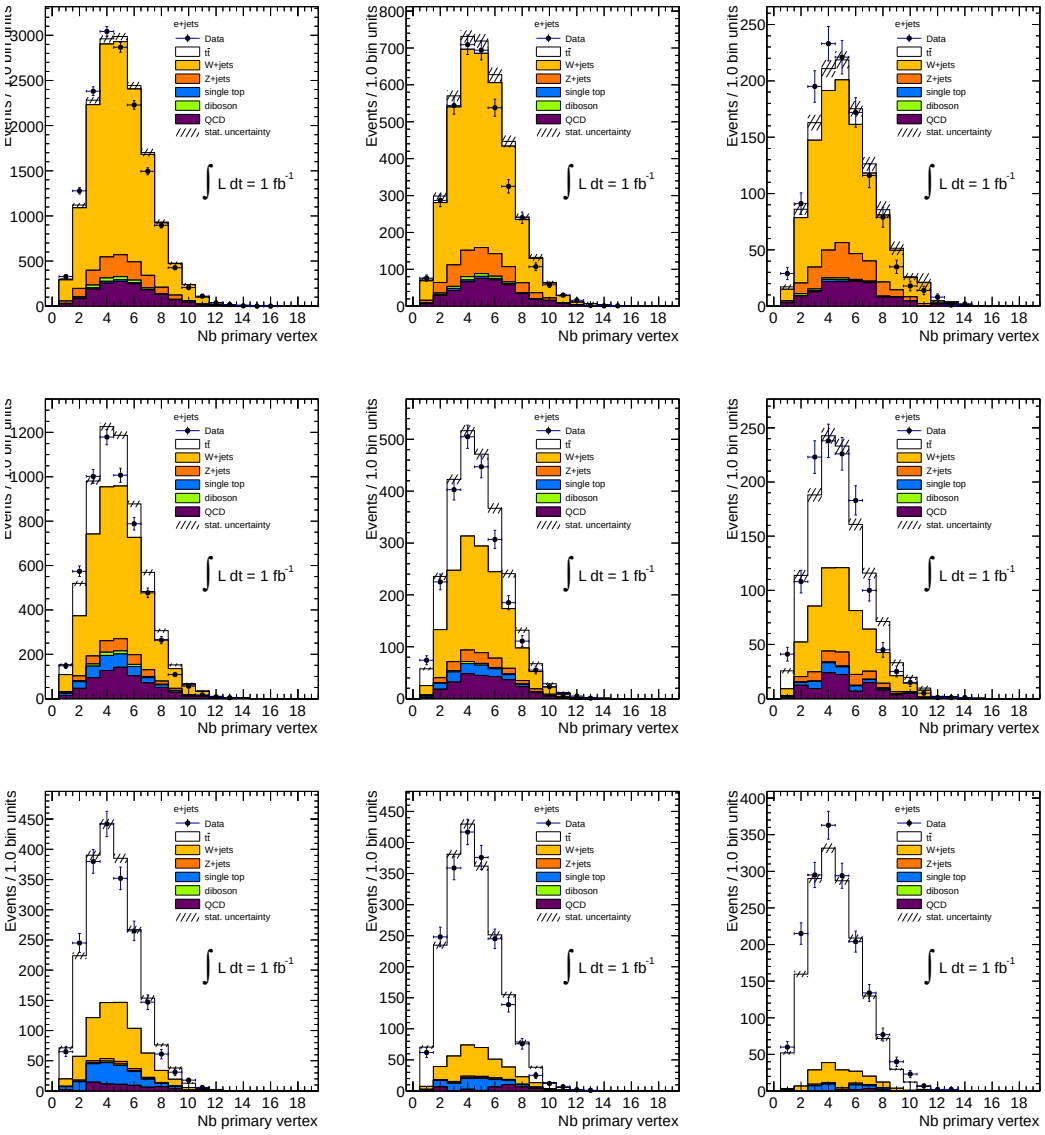

Figure B.13: Number of primary vertices in the 0- (top), 1- (medium) and $\geq$ 2- (bottom) b-jet multiplicity bins for the electron data sample. The data (dots with error bars) are compared to the expectation. Scale factors obtained from the asymmetry analysis have been applied to the W+jets samples.

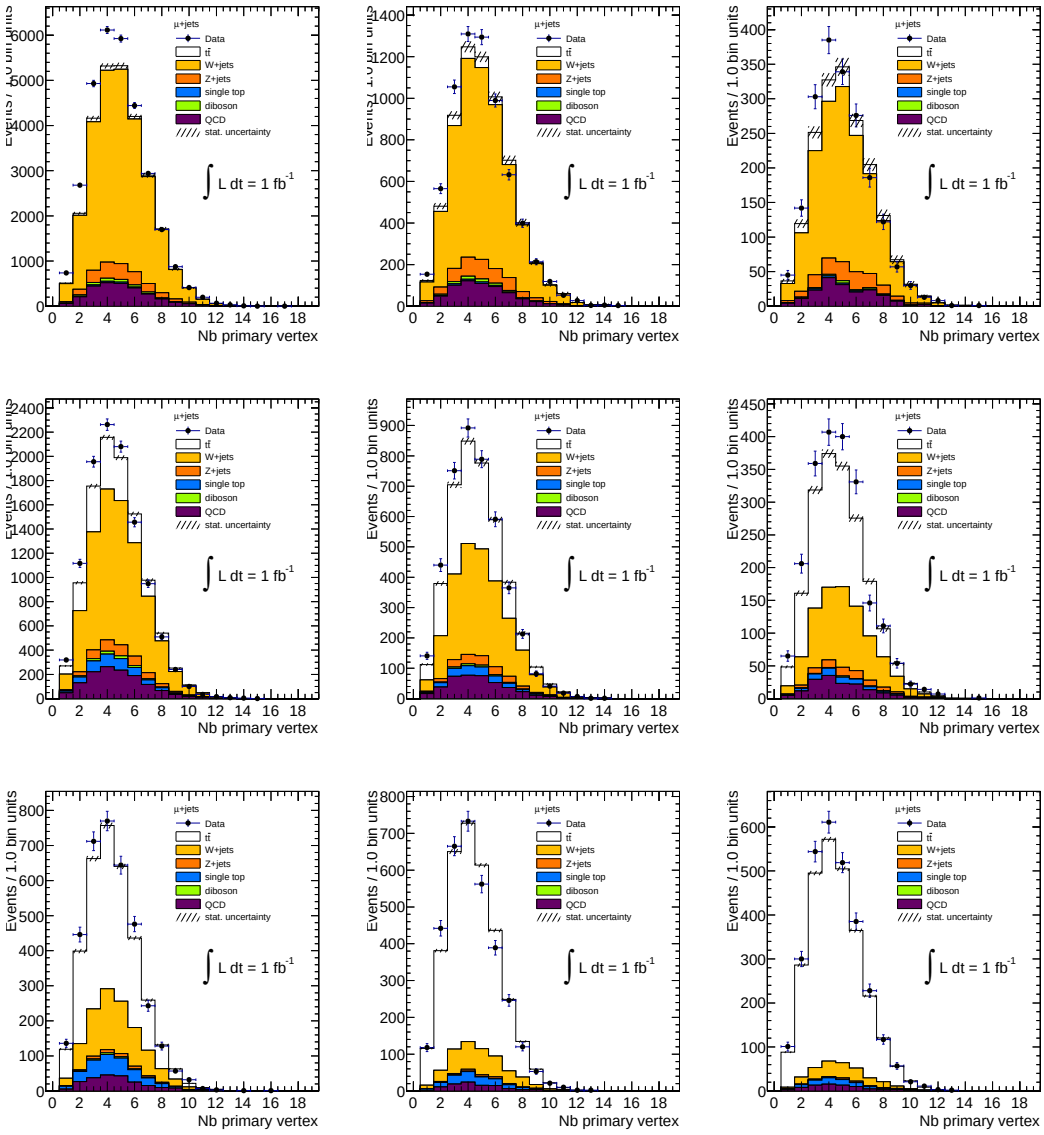

3-jet 4-jet $\geq$ 5-jet

Figure B.14: Number of primary vertices in the 0- (top), 1- (medium) and $\geq$ 2- (bottom) b-jet multiplicity bins for the muon data sample. The data (dots with error bars) are compared to the expectation. Scale factors obtained from the asymmetry analysis have been applied to the W+jets samples.

Appendix C

Tagging Rate Factor Method

The stability of the fit depends on having reasonably smooth templates, built with samples large enough such that the statistical fluctuations of the templates are small. This can be problematic in the case of small backgrounds, where few events survive the event selection, or in general at high jet and/or b-tag multiplicities. Having high statistics templates is also important for the systematically variated templates, because we want to measure real systematic shape variations associated to a given effect instead of pure random fluctuations.

To overcome this problem, we apply a tagging probability to the untagged templates to obtain the tagged ones. The per-event tagging probability to have 0-, 1- or $\geq$2 b-tags is obtained from the per-jet tagging rates, which depend on the flavour, η and p_{T} of the jet. For example, the probability to have a 1-tag event is computed as:

$$P(=1 \text{ tag}) = \sum_i \epsilon_i \prod_{j \neq i} (1 - \epsilon_j)$$

where ϵ_i is the tagging probability of jet i.

The agreement between the original templates, obtained after full event selection, and the ones obtained with this tagging method is good, both in yield, typically better than 5%, and shape. The tagged templates are finally normalized to the yields obtained after full event selection.

Figure C.1 shows the comparison of templates for the Z+jets samples in the 3-jet 0-tag and 5-jet 2-tag bins obtained after full event selection or applying the tagging method.

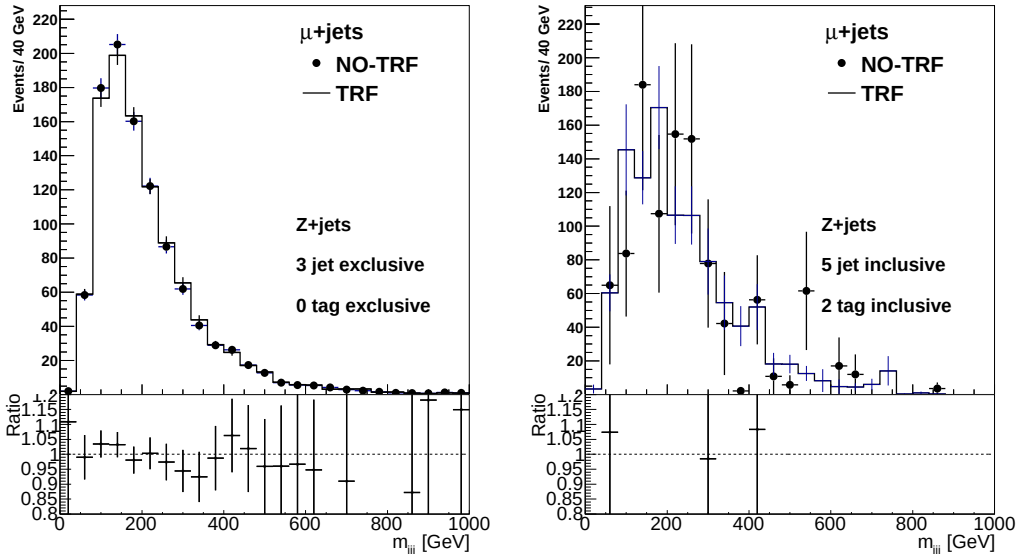

Figure C.1: Three-jet invariant mass in the (left) 3-jet 0-tag and (right) 5-jet 2-tag bins. The solid red lines show the shapes obtained with this weighting method, whereas the original shape is shown in blue points with error bars. The ratio of the nominal over the varied templates is also shown.

Appendix D

Fits for electron and muon channel

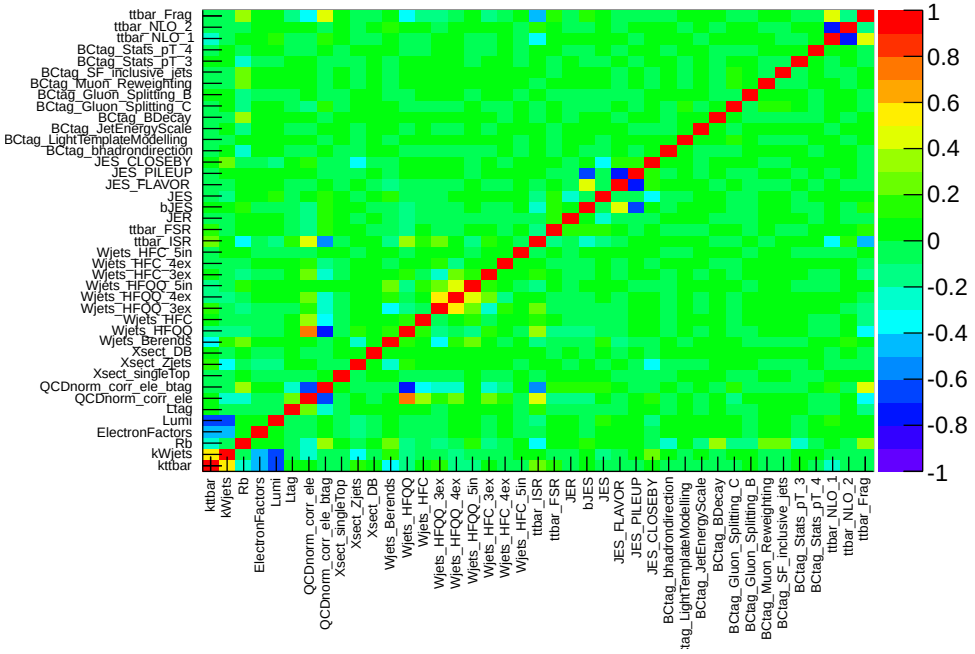

Figure D.1: Correlation matrix for the electron data fit with R_b allowed to vary.

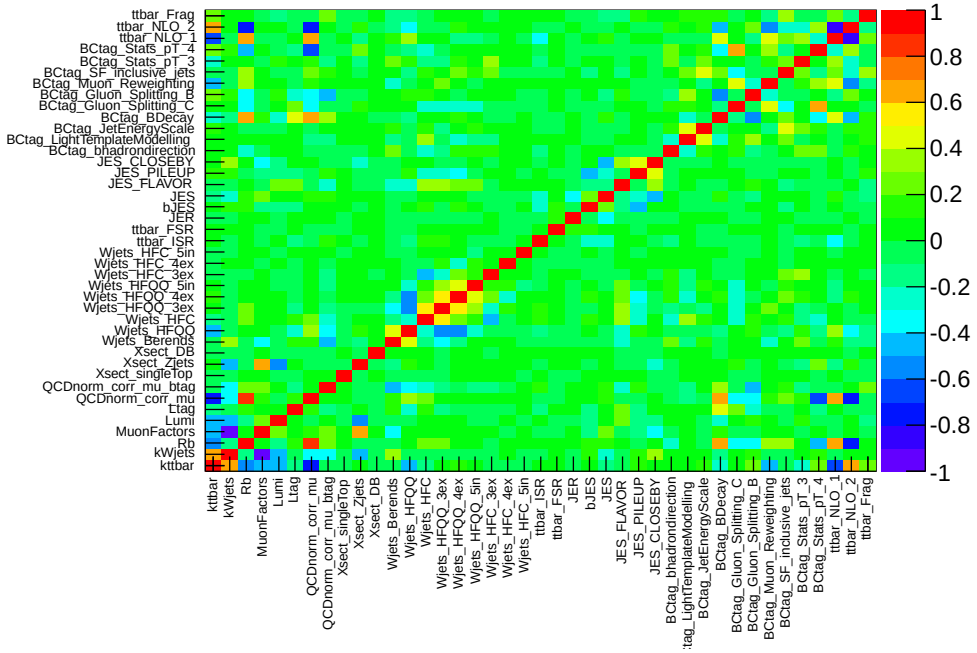

Figure D.2: Correlation matrix for the muon data fit with R_b allowed to vary.

Table D.1: Fit to the electron data with R_b allowed to vary.

k_{ttbar}	1.008	0.067/-0.063
k_{Wjets}	1.104	0.076/-0.074
R_b	1.011	0.033/-0.037
Systematic	α	$\Delta\alpha$
ElectronFactors	-0.042	0.998/-0.998
Lumi	-0.052	0.985/-1.004
QCDnorm_corr_ele	-0.960	0.616/-0.694
QCDnorm_corr_ele_btag	-1.384	0.734/-0.599
Xsect_singleTop	0.271	0.983/-0.988
Xsect_Zjets	0.558	0.393/-0.346
Xsect_DB	-0.082	1.001/-0.999
Wjets_Berends	0.153	0.145/-0.149
Wjets_HFQQ	0.297	0.581/-0.585
Wjets_HFC	0.661	0.928/-0.951
Wjets_HFQQ_3ex	0.057	0.729/-0.728
Wjets_HFQQ_4ex	1.013	0.678/-0.687
Wjets_HFQQ_5in	-0.904	0.750/-0.752
Wjets_HFC_3ex	0.306	0.916/-0.926
Wjets_HFC_4ex	0.019	0.967/-0.961
Wjets_HFC_5in	0.189	0.984/-0.993
ttbar_ISR	-0.095	0.086/-0.120
ttbar_FSR	-0.161	0.155/-0.176
bJES	0.850	0.478/-0.536
JES	-0.675	0.171/-0.119
JES_FLAVOR	1.319	0.236/-0.242
JES_PILEUP	-0.011	0.402/-0.338
JES_CLOSEBY	0.352	0.225/-0.376
JER	-0.516	0.065/-0.059

Systematic	α	$\Delta\alpha$
BCtag_bhadrondirection	-0.116	0.991/-0.991
BCtag_LightTemplateModelling	0.284	0.921/-0.934
BCtag_JetEnergyScale	-0.039	0.979/-0.962
BCtag_BDecay	0.053	0.875/-1.082
BCtag_Gluon_Splitting_C	-0.271	0.851/-0.851
BCtag_Gluon_Splitting_B	-0.113	0.983/-0.963
BCtag_Muon_Reweighting	0.187	0.974/-0.961
BCtag_SF_inclusive_jets	0.342	0.876/-0.923
BCtag_Stats_pT_3	0.015	1.004/-0.977
BCtag_Stats_pT_4	-0.202	0.942/-0.933
Ltag	0.304	0.970/-0.978
ttbar_NLO_1	0.500	0.316/-0.304
ttbar_NLO_2	0.311	0.222/-0.224
ttbar_Frag	0.122	0.254/-0.290

Table D.2: Fit to the muon data with R_b allowed to vary.

k_{ttbar}	1.083	0.151/-0.135
k_{Wjets}	1.148	0.109/-0.104
R_b	0.943	0.082/-0.041
Systematic	α	$\Delta\alpha$
MuonFactors	-0.117	1.010/-0.987
Lumi	-0.076	1.007/-0.993
QCDnorm_corr_mu	-0.045	0.810/-0.764
QCDnorm_corr_mu_btag	-1.191	0.361/-0.410
Xsect_singleTop	0.030	0.993/-0.984
Xsect_Zjets	0.596	0.587/-0.598
Xsect_DB	-0.016	1.000/-0.999
Wjets_Berends	-0.036	0.119/-0.125
Wjets_HFQQ	0.963	0.544/-0.535
Wjets_HFC	0.099	0.923/-0.916
Wjets_HFQQ_3ex	0.136	0.720/-0.726
Wjets_HFQQ_4ex	0.295	0.653/-0.645
Wjets_HFQQ_5in	0.064	0.740/-0.736
Wjets_HFC_3ex	-0.147	0.908/-0.893
Wjets_HFC_4ex	0.173	0.948/-0.955
Wjets_HFC_5in	0.051	0.985/-0.987
ttbar_ISR	-0.239	0.149/-0.138
ttbar_FSR	-0.075	0.151/-0.144
bJES	0.137	0.426/-0.426
JES	-0.495	0.201/-0.139
JES_FLAVOR	0.852	0.233/-0.280
JES_PILEUP	0.212	0.236/-0.469
JES_CLOSEBY	-0.015	0.407/-0.363
JER	-0.447	0.052/-0.049

Systematic	α	$\Delta\alpha$
BCtag_bhadrondirection	0.050	0.841/-0.973
BCtag_LightTemplateModelling	0.097	0.951/-0.958
BCtag_JetEnergyScale	0.169	0.908/-1.027
BCtag_BDecay	-0.641	1.461/-0.944
BCtag_Gluon_Splitting_C	0.010	0.815/-1.019
BCtag_Gluon_Splitting_B	0.348	1.071/-1.302
BCtag_Muon_Reweighting	-0.220	1.232/-1.033
BCtag_SF_inclusive_jets	0.172	1.032/-0.704
BCtag_Stats_pT_3	0.024	0.868/-0.994
BCtag_Stats_pT_4	0.291	1.010/-1.272
Ltag	0.240	0.932/-0.982
ttbar_NLO_1	0.513	0.573/-0.488
ttbar_NLO_2	0.308	0.534/-0.627
ttbar_Frag	-0.266	0.225/-0.242

Appendix E

Fit with R_b set to one

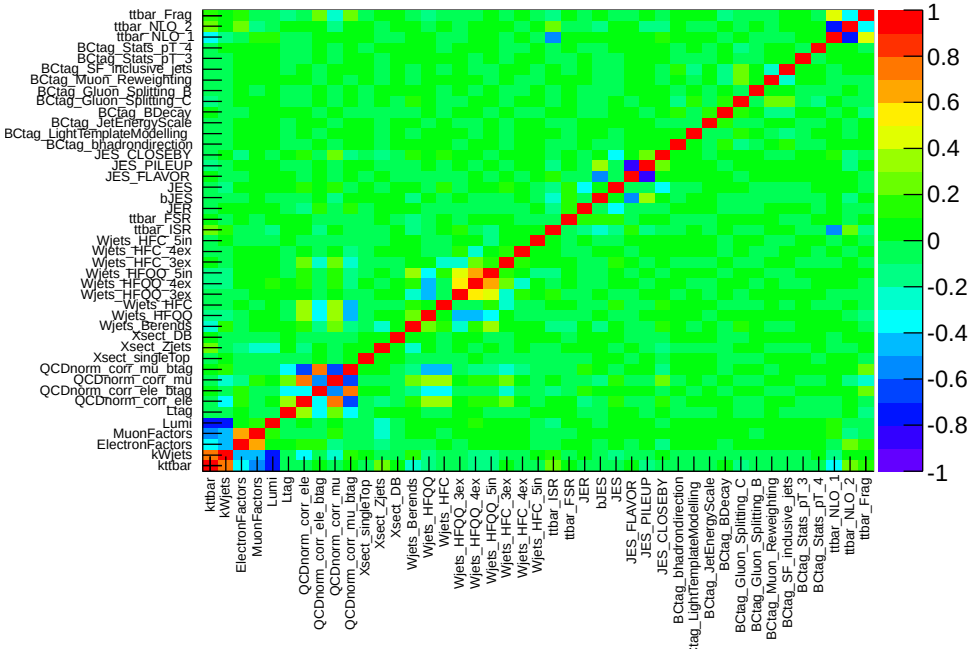

Figure E.1: Correlation matrix for the electron and muon combined data fit with R_b fixed to one.

E. FIT WITH R_B SET TO ONE

Table E.1: Fit to electron and muon combined data with R_b fixed to 1.

k_{ttbar}	1.024	0.059/-0.053
k_{Wjets}	1.052	0.065/-0.061
R_b	1.000	0.000/0.000
Systematic	α	$\Delta\alpha$
ElectronFactors	-0.198	0.910/-0.926
MuonFactors	0.610	0.550/-0.550
Lumi	0.112	0.986/-0.991
QCDnorm_corr_ele	-0.218	0.461/-0.445
QCDnorm_corr_ele_btag	-1.229	0.273/-0.302
QCDnorm_corr_mu	0.277	0.707/-0.699
QCDnorm_corr_mu_btag	-0.776	0.215/-0.208
Xsect_singleTop	0.379	0.950/-0.971
Xsect_Zjets	0.753	0.284/-0.283
Xsect_DB	-0.108	1.003/-0.996
Wjets_Berends	-0.185	0.091/-0.095
Wjets_HFQQ	0.712	0.401/-0.400
Wjets_HFC	0.158	0.776/-0.789
Wjets_HFQQ_3ex	0.406	0.658/-0.668
Wjets_HFQQ_4ex	0.325	0.623/-0.622
Wjets_HFQQ_5in	-0.297	0.675/-0.673
Wjets_HFC_3ex	-0.408	0.847/-0.821
Wjets_HFC_4ex	0.356	0.889/-0.908
Wjets_HFC_5in	0.178	0.941/-0.961
ttbar_ISR	-0.102	0.079/-0.103
ttbar_FSR	-0.104	0.111/-0.108
bJES	0.481	0.376/-0.395
JES	-0.588	0.121/-0.090
JES_FLAVOR	0.908	0.186/-0.214
JES_PILEUP	0.398	0.174/-0.341
JES_CLOSEBY	0.098	0.323/-0.270
JER	-0.370	0.039/-0.037

Systematic	α	$\Delta\alpha$
BCtag_bhadrondirection	-0.130	0.784/-0.800
BCtag_LightTemplateModelling	0.201	0.787/-0.766
BCtag_JetEnergyScale	-0.030	0.789/-0.821
BCtag_BDecay	0.004	0.737/-0.713
BCtag_Gluon_Splitting_C	-0.393	0.708/-0.688
BCtag_Gluon_Splitting_B	-0.095	0.800/-0.826
BCtag_Muon_Reweighting	0.215	0.758/-0.755
BCtag_SF_inclusive_jets	0.537	0.681/-0.728
BCtag_Stats_pT_3	-0.018	0.801/-0.826
BCtag_Stats_pT_4	-0.207	0.786/-0.801
Ltag	0.409	0.706/-0.799
ttbar_NLO_1	0.400	0.262/-0.250
ttbar_NLO_2	0.264	0.182/-0.185
ttbar_Frag	-0.112	0.152/-0.156

E. FIT WITH R_B SET TO ONE

Appendix F

Nuisance Parameters Uncertainty Distributions

F. NUISANCE PARAMETERS UNCERTAINTY DISTRIBUTIONS

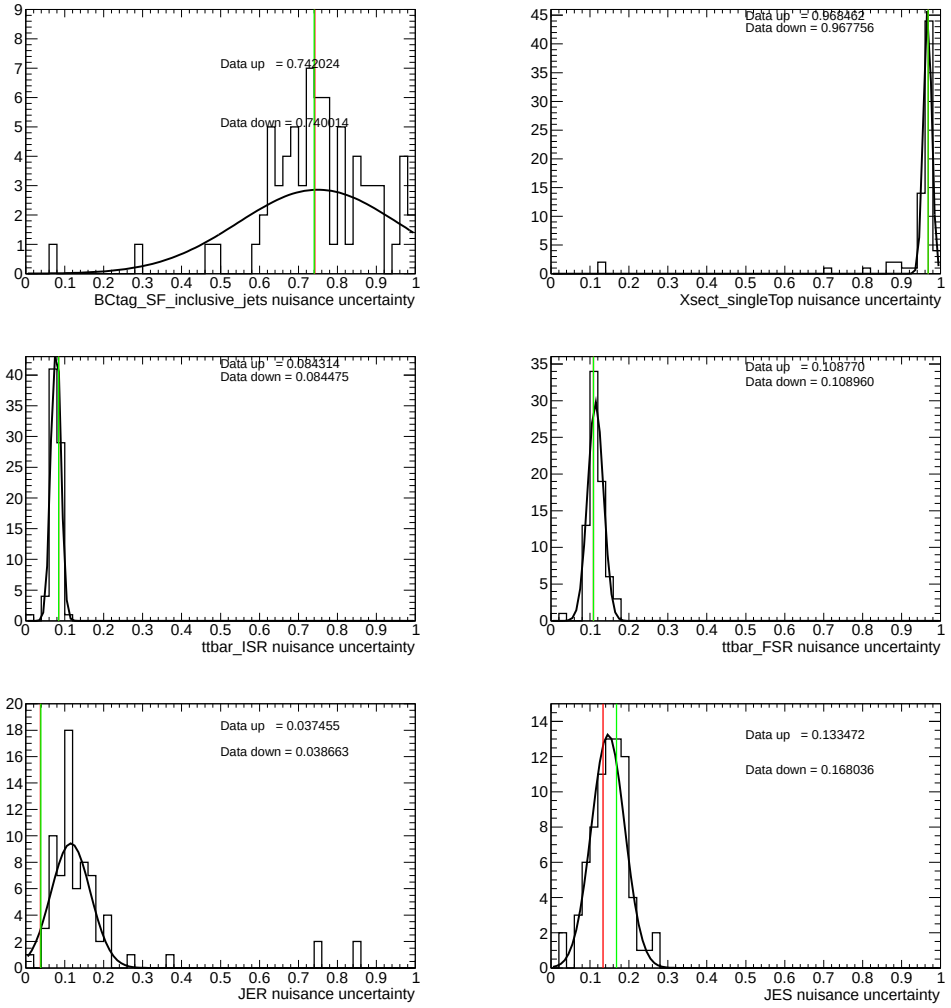

Figure F.1: Distribution of the uncertainties of the fitted nuisance parameters. The histogram corresponds to 40 PSE and includes both the up and down uncertainties. The fitted values on data are shown by the vertical lines for the up (red) and down (green) uncertainties.

Bibliography

[1] J. Beringer *et al.*, "*Review of Particle Physics*", Phys. Rev. D **86** (2012). xv, 5, 8, 9

[2] J. Thomson, "*Cathode rays*", Phil.Mag. **44**, 293 (1897). 1

[3] J. Joyce, *Finnegans Wake* (Penguin Books, 1999). 1

[4] G. Zweig, "*Memories of Murray and the Quark Model*", International Journal of Modern Physics A **25**, 3863 (2010), 1007.0494. 1

[5] S. Glashow, "*Partial Symmetries of Weak Interactions*", Nucl.Phys. **22**, 579 (1961). 1, 5

[6] S. Weinberg, "*A Model of Leptons*", Phys.Rev.Lett. **19**, 1264 (1967). 1, 5

[7] S. N. Bose, "*Planck's Law and the Light Quantum Hypothesis*", Journal of Astrophysics and Astronomy **15**, 3 (1994). 1

[8] CERN, http://press.web.cern.ch/press/pressreleases/releases2012/pr17.12e.html, 2012. 1

[9] N. Cabibbo, "*Unitary Symmetry and Leptonic Decays*", Phys. Rev. Lett. **10**, 531 (1963). 1

[10] F. N. Kurie, J. R. Richardson, and H. C. Paxton, "*The Radiations Emitted from Artificially Produced Radioactive Substances. I. The Upper Limits and Shapes of the β-Ray Spectra from Several Elements*", Physical Review **49**, 368 (1936). 3

[11] P. A. M. Dirac, "*The Quantum Theory of the Emission and Absorption of Radiation*", Royal Society of London Proceedings Series A **114**, 243 (1927). 4

[12] M. Gell-Mann and F. E. Low, "*Quantum Electrodynamics at Small Distances*", Phys. Rev. **95**, 1300 (1954). 4

[13] W. Pauli, Pauli letter collection: letter to lise meitner, Typed copy. 4

[14] V. Barger and R. Phillips, *Collider Physics* (Addison-Wesley Publishing Company, 1997). 4

[15] M. L. Perl *et al.*, "*Evidence for Anomalous Lepton Production in* $e^+ - e^-$ *Annihilation*", Phys. Rev. Lett. **35**, 1489 (1975). 5

[16] K. Kodama *et al.*, "*Observation of tau neutrino interactions*", Physics Letters B **504**, 218 (2001). 5

[17] C. Rubbia, "*Experimental observation of the intermediate vector bosons* W^+, W^-, *and* Z^0", Reviews of Modern Physics **57**, 699 (1985). 6

[18] J. Goldstone, "*Field theories with ' Superconductor ' solutions*", Il Nuovo Cimento (1955-1965) **19**, 154 (1961), 10.1007/BF02812722. 6

[19] F. Englert and R. Brout, "*Broken Symmetry and the Mass of Gauge Vector Mesons*", Phys.Rev.Lett. **13**, 321 (1964). 6

[20] V. E. Barnes *et al.*, "*Observation of a Hyperon with Strangeness Minus Three*", Phys. Rev. Lett. **12**, 204 (1964). 7

[21] M. Gell-Mann, "*A schematic model of baryons and mesons*", Physics Letters **8**, 214 (1964). 7

[22] G. Zweig, "*An* SU_3 *model for strong interaction symmetry and its breaking.*", (1964). 7

[23] E. D. Bloom *et al.*, "*High-Energy Inelastic e-p Scattering at 6 and 10 degrees*", Phys. Rev. Lett. **23**, 930 (1969). 7

[24] M. Breidenbach *et al.*, "*Observed Behavior of Highly Inelastic Electron-Proton Scattering*", Phys. Rev. Lett. **23**, 935 (1969). 7

[25] L. M. Lederman, "*The Upsilon Particle*", Scientific American **239**, 72 (1978). 7

[26] CDF Collaboration, F. Abe *et al.*, "*Observation of Top Quark Production in $\overline{p}p$ Collisions with the Collider Detector at Fermilab*", Phys. Rev. Lett. **74**, 2626 (1995). 7, 13

[27] D0 Collaboration, S. Abachi *et al.*, "*Observation of the Top Quark*", Phys. Rev. Lett. **74**, 2632 (1995). 7, 13

[28] K. G. Wilson, "*Confinement of quarks*", Phys. Rev. D **10**, 2445 (1974). 8

[29] M. Shifman, "*Understanding Confinement in QCD: Elements of a Big Picture*", Int.J.Mod.Phys. **A25**, 4015 (2010), 1007.0531. 8

[30] L. Chau, "*Quark Mixing in Weak Interactions*", Phys. Rept. **95**, 1 (1983). 9

[31] B. Pontecorvo, "*Neutrino Experiments and the Problem of Conservation of Leptonic Charge*", Soviet Journal of Experimental and Theoretical Physics **26**, 984 (1968). 9

[32] S. L. Glashow, J. Iliopoulos, and L. Maiani, "*Weak Interactions with Lepton-Hadron Symmetry*", Phys. Rev. D **2**, 1285 (1970). 9, 19

[33] J. E. Augustin *et al.*, "*Discovery of a Narrow Resonance in e^+e^- Annihilation*", Phys. Rev. Lett. **33**, 1406 (1974). 9

[34] J. J. Aubert *et al.*, "*Experimental Observation of a Heavy Particle J*", Phys. Rev. Lett. **33**, 1404 (1974). 9

[35] Martin-Stirling-Thorne-Watt, Mstw parton distribution functions, http://mstwpdf.hepforge.org/, 2009. 14

[36] S. Moch and P. Uwer, "*Theoretical status and prospects for top-quark pair production at hadron colliders*", Phys.Rev. **D78**, 034003 (2008), 0804.1476. 14

[37] D. Wicke, "*Properties of the Top Quark*", Eur.Phys.J. **C71**, 1627 (2011), 1005.2460. 17

[38] F. Deliot and D. A. Glenzinski, "*Top Quark Physics at the Tevatron*", (2010), 1010.1202. 17

[39] Tevatron Electroweak Working Group, CDF and D0 Collaborations, T. Collaboration, "*Combination of CDF and D0 results on the mass of the top quark using up to 5.8 fb-1 of data*", (2011), 1107.5255. 17

[40] CDF Collaboration, T. Aaltonen *et al.*, "*Direct Top-Quark Width Measurement at CDF*", Phys. Rev. Lett. **105**, 232003 (2010). 18

[41] D0 Collaboration, V. M. Abazov *et al.*, "*Improved determination of the width of the top quark*", Phys. Rev. D **85**, 091104 (2012). 18

[42] M. Okamoto, "*Full determination of the CKM matrix using recent results from lattice QCD*", PoS **LAT2005**, 013 (2006), hep-lat/0510113. 18

[43] J. Alwall *et al.*, "*Is V(tb) = 1?*", Eur.Phys.J. **C49**, 791 (2007), hep-ph/0607115. 19, 77

[44] CDF Collaboration, D. Acosta *et al.*, "*Measurement of R_b at the Collider Detector at Fermilab*", Phys. Rev. Lett. **95**, 102002 (2005). 19

[45] D0 Collaboration, V. Abazov *et al.*, "*Simultaneous measurement of the ratio $B(t \to Wb)$ /$B(t \to Wq)$ and the top quark pair production cross section with the D0 detector at $\sqrt{s}$ = 1.96-TeV*", Phys.Rev.Lett. **100**, 192003 (2008), 0801.1326. 19

[46] CMS Collaboration, First measurement of $r = b(t \to wb)/b(t \to wq)$ in the dilepton channel in pp collisions at $\sqrt(s)$=7 tev - cms pas top-11-029, 2012. 19

[47] ATLAS Collaboration, CERN Report No. ATLAS-CONF-2011-061, 2011 (unpublished). 19

[48] ATLAS Collaboration, G. Aad *et al.*, "*Search for FCNC single top-quark production at sqrt(s) = 7 TeV with the ATLAS detector*", Phys.Lett. **B712**, 351 (2012), 1203.0529. 19

[49] CMS Collaboration, S. Chatrchyan *et al.*, "*Search for Same-Sign Top-Quark Pair Production at sqrt(s) = 7 TeV and Limits on Flavour Changing Neutral Currents in the Top Sector*", JHEP **1108**, 005 (2011), 1106.2142. 19

[50] ATLAS Collaboration, G. Aad *et al.*, "*Measurement of the charge asymmetry in top quark pair production in pp collisions at sqrt(s) = 7 TeV using the ATLAS detector*", (2012), 1203.4211. 20

[51] CMS Collaboration, S. Chatrchyan *et al.*, "*Measurement of the charge asymmetry in top-quark pair production in proton-proton collisions at sqrt(s) = 7 TeV*", Phys.Lett. **B709**, 28 (2012), 1112.5100. 20

[52] C. Berger *et al.*, "*Precise Predictions for W + 4 Jet Production at the Large Hadron Collider*", Phys.Rev.Lett. **106**, 092001 (2011), 1009.2338. 21

[53] N. Kidonakis, "*Next-to-next-to-leading-order collinear and soft gluon corrections for t-channel single top quark production*", Phys.Rev. **D83**, 091503 (2011), 1103.2792. 23

[54] N. Kidonakis, "*Two-loop soft anomalous dimensions for single top quark associated production with a W- or H-*", Phys.Rev. **D82**, 054018 (2010), 1005.4451. 23

[55] N. Kidonakis, "*NNLL resummation for s-channel single top quark production*", Phys.Rev. **D81**, 054028 (2010), 1001.5034. 23

[56] Martelli, "*Dibosons from CMS*", (2012), 1201.4596. 23

[57] A. Buckley *et al.*, "*General-purpose event generators for LHC physics*", Phys.Rept. **504**, 145 (2011), 1101.2599. 25

[58] T. Sjotrand and A. de Roeck, Monte carlo generators for the lhc. mc generators for the lhc, in *Monte Carlo generators for the LHC. MC generators for the LHC*, p. Streaming video ; transparencies ; 4 DVD video, Geneva, 2005, CERN, CERN, CERN, Geneva, 4 - 7 Apr 2005. 25

[59] V. Gribov and L. Lipatov, "*Deep inelastic e p scattering in perturbation theory*", Sov.J.Nucl.Phys. **15**, 438 (1972). 28

[60] G. Altarelli and G. Parisi, "*Asymptotic Freedom in Parton Language*", Nucl.Phys. **B126**, 298 (1977). 28

[61] Y. L. Dokshitzer, "*Calculation of the Structure Functions for Deep Inelastic Scattering and e+ e- Annihilation by Perturbation Theory in Quantum Chromodynamics.*", Sov.Phys.JETP **46**, 641 (1977). 28

[62] L. R. Evans and P. Bryant, "*LHC Machine*", J. Instrum. **3**, S08001. 164 p (2008), This report is an abridged version of the LHC Design Report (CERN-2004-003). 31

[63] CERN, Linac-http://linac2.home.cern.ch/linac2/default.htm, 2009. 32

[64] B. Mikulec *et al.*, "*High Intensity Beams from the CERN PS Booster.*", p. 4 p (2009). 32

[65] CERN, Accelerator, proton synchrotron,http://public.web.cern.ch/public/en/research/ps-en.html. 32

[66] N. A. Tahir *et al.*, "*The CERN Super Proton Synchrotron as a tool to study high energy density physics*", New Journal of Physics **10**, 073028 (2008). 32

[67] T. Cornelissen *et al.*, CERN Report No. ATL-SOFT-PUB-2007-007. ATL-COM-SOFT-2007-002, 2007 (unpublished). 53

[68] A. Collaboration, CERN Report No. ATL-PHYS-PUB-2011-006, 2011 (unpublished). 56

[69] M. Cacciari, G. P. Salam, and G. Soyez, "*The anti- k t jet clustering algorithm*", Journal of High Energy Physics **2008**, 063 (2008). 58, 81

[70] Fastjet Collaboration, Fastjet- http://fastjet.fr, 2012. 58

[71] ATLAS Collaboration, CERN Report No. ATLAS-CONF-2011-028, 2011 (unpublished). 63

[72] P. Z. Skands, "*Tuning Monte Carlo generators: The Perugia tunes*", Phys. Rev. D **82**, 074018 (2010). 64

[73] ATLAS Collaboration, G. Aad *et al.*, "*Study of Jet Shapes in Inclusive Jet Production in pp Collisions at sqrt(s) = 7 TeV using the ATLAS Detector*", Phys.Rev. **D83**, 052003 (2011), 1101.0070. 64

[74] ATLAS Collaboration, CERN Report No. ATLAS-CONF-2011-014, 2011 (unpublished). 64

[75] ATLAS Collaboration, CERN Report No. ATLAS-CONF-2010-055, 2010 (unpublished). 64

[76] A. Collaboration, CERN Report No. ATLAS-CONF-2011-030, 2011 (unpublished). 64

[77] ATLAS Collaboration, CERN Report No. ATLAS-CONF-2011-053, 2011 (unpublished). 64, 103

[78] ATLAS Collaboration, CERN Report No. ATLAS-CONF-2011-062, 2011 (unpublished). 64, 104

[79] CERN, CERN Report No. ATLAS-CONF-2011-089, 2011 (unpublished). 67, 106

[80] U. Langenfeld, S. Moch, and P. Uwer, "*New results for t anti-t production at hadron colliders*", (2009), 0907.2527. 77, 93

[81] G. Aad *et al.*, "*The ATLAS Simulation Infrastructure*", The European Physical Journal C, Volume 70, Issue 3, pp.823-874 **70**, 823 (2010), 1005.4568. 78

[82] S. Frixione, P. Nason, and B. R. Webber, "*Matching NLO QCD and parton showers in heavy flavor production*", JHEP **0308**, 007 (2003), hep-ph/0305252. 78

[83] J. Pumplin *et al.*, "*New generation of parton distributions with uncertainties from global QCD analysis*", JHEP **0207**, 012 (2002), hep-ph/0201195. 78

[84] J. Aguilar-Saavedra, "*A Minimal set of top anomalous couplings*", Nucl.Phys. **B812**, 181 (2009), 0811.3842. 78, 98

[85] M. L. Mangano, M. Moretti, F. Piccinini, R. Pittau, and A. D. Polosa, "*ALPGEN, a generator for hard multiparton processes in hadronic collisions*", JHEP **0307**, 001 (2003), hep-ph/0206293. 78, 109

[86] S. Frixione, E. Laenen, P. Motylinski, B. R. Webber, and C. D. White, "*Single-top hadroproduction in association with a W boson*", JHEP **0807**, 029 (2008), 0805.3067. 79

[87] A. Buckley, H. Hoeth, H. Lacker, H. Schulz, and J. E. von Seggern, "*Systematic event generator tuning for the LHC*", Eur.Phys.J. **C65**, 331 (2010), 0907.2973. 79

[88] ATLAS Collaboration, G. Aad *et al.*, "*Measurement of inclusive jet and dijet cross sections in proton-proton collisions at 7 TeV centre-of-mass energy with the ATLAS detector*", Eur.Phys.J. **C71**, 1512 (2011), 1009.5908. 81

[89] N. Benekos *et al.*, CERN Report No. ATL-COM-PHYS-2011-123, 2011 (unpublished), Supporting document for Winter 2011 top physics measurements. 82

[90] G. Aad, CERN Report No. ATL-COM-PHYS-2010-990, 2010 (unpublished). 82

[91] CERN, CERN Report No. ATLAS-CONF-2011-063, 2011 (unpublished). 82

[92] M. Bosman *et al.*, CERN Report No. ATL-COM-PHYS-2010-331, 2010 (unpublished). 83, 99

[93] ATLAS Collaboration, G. Aad *et al.*, "*Measurement of the top quark-pair production cross section with ATLAS in pp collisions at* $\sqrt{s} = 7$ *TeV*", Eur.Phys.J. **C71**, 1577 (2011), 1012.1792. 91, 107

[94] Goettingen, Asymmetry factors from w+jets analysis, https://twiki.cern.ch/twiki/bin/viewauth/atlasprotected/wplusjetsbackgroundsfortopanalyses#sfs_and_u 2009. 91, 107

[95] K. Becker *et al.*, CERN Report No. ATL-COM-PHYS-2011-768, 2011 (unpublished). 93

[96] N. Reid, Likelihood Inference in the Presence of Nuisance Parameters, in *Statistical Problems in Particle Physics, Astrophysics, and Cosmology*, edited by L. Lyons, R. Mount, and R. Reitmeyer, p. 265, 2003, arXiv:physics/0312079. 94

[97] D. L. Mateos, Neutrino correction to semileptonic b-jets with release 17, 2009. 98

[98] CERN, CERN Report No. ATLAS-CONF-2011-032, 2011 (unpublished). 103, 104

[99] A. Collaboration, https://twiki.cern.ch/twiki/bin/viewauth/atlasprotected/topjetliaisonr16recommendations#b_jets_jes_uncertainty, 2009. 104

[100] N. Kidonakis, "*Next-to-next-to-leading logarithm resummation for s-channel single top quark production*", Phys. Rev. D **81**, 054028 (2010). 107

[101] N. Kidonakis, "*Next-to-next-to-leading-order collinear and soft gluon corrections for t-channel single top quark production*", Phys. Rev. D **83**, 091503 (2011). 107

[102] F. Berends, W. Giele, H. Kuijf, R. Kleiss, and W. Stirling, "*Multijet production in W, Z events at pp colliders*", Physics Letters B **224**, 237 (1989). 108

[103] B. P. Kersevan and E. Richter-Was, "*The Monte Carlo event generator AcerMC version 2.0 with interfaces to PYTHIA 6.2 and HERWIG 6.5*", (2004), hep-ph/0405247. 109

[104] P. Nason and B. Webber, "*Next-to-Leading-Order Event Generators*", (2012), 1202.1251. 109

[105] ATLAS Collaboration, CERN Report No. ATLAS-CONF-2011-121, 2011 (unpublished). 110

Acknowledgements

El primer agraïment és per la meva directora de tesi Lluïsa Mir, que òbviament, és una de les persones que més ha contribuït a la tesi. De fet, tinc la creença que sense ella, ni tan sols l'hagués començat.

Al Andreu Pacheco, li vull agrair que hagi estat una de les persones més importants durant la meva estada al IFAE, sens dubte, ha fet possible que estigueu llegint aquestes paraules.

Gràcies al grup d'ATLAS del IFAE, i en especial al subgrup del Top, per tenir aquest 'bon rotllo' sempre. Començant per la Martine i l'Aurelio, que han estat una font incessant de idees i genialitats, i als no tan sèniors, fincats al CERN: Clement, Luca, Francesco i Antonella. I recentment a Davide, Eve i Javier, treballar amb ells ha sigut tot un plaer.

Un record especial a la gent del PIC, que durant el meu primer any al Tier-2, on vaig trobar grans persones i els quals encara conservo com amics, en especial, a Xavi Espinal. Que hauria passat si no ens haguèssim trobat aquell dia al IFAE?

Al meu amic dins i fora del despatx, en Volker, qui m'ha ensenyat un munt de trucs: de vim, de bash, de c++, etc... i és el principal autor del Fitter, que m'ha ajudat a conseguir els resultats d'aquesta tesi!

Chiara ha estat durant aquesta última època, la persona que més estones he compartit al IFAE. Gràcies per les mil discussions que hem tingut de física i no física, i intentar ensenyar-me una mica d'italià.

A l'Estel, gràcies per tenir sempre un sofà a punt i anar a comprar-me el suc de pinya quan pujava al cern!

Al Lluís, que hem sigut inseparables des de que vam començar la carrera pràcticament, i espero, i no tinc cap dubte que seguirà sent així.

Al juniors del IFAE: Javi: espero que el proper dinar no és faci esperar, i poder repetir-ho durant molts anys. Als periquitos de l'IFAE, l'Oriol i l'Alex, força Espanyol! Marc, a l'únic físic-veterinari que coneix-ho i que segurament, coneixeré. Martí, Emili, Ramon, John, i un llarg etc: gràcies per aquestes converses tant interessants que hem tingut durant els dinars.

Finalment, vull agrair a la meva família tot l'esforç que han fet durant tots els meus anys d'estudis. Les coses no han estat fàcils, però finalment hem vist la llum! I com no, donar un especial agraïment a l'Ángel i la Núria, per deixar-me les claus del paradís, on s'han escrit aquestes paraules... I per últim, però no menys important, a la persona que més m'ha aguantat, qui m'ha ajudat en tot i, per que no confessar-ho, fins i tot a fer alguns plots! En definitiva, la persona que dia darrere dia, m'ha donat l'empenta necessària. Sobren les paraules....Gràcies Petita!